UNIVERSITY OF THE WESTERN CAPE

Probing the primordial Universe using the SKA in combination with other cosmological surveys

by

William Matthewson

A thesis submitted for the
degree of **Master of Science**

in the
Faculty of Natural Science
Department of Physics and Astronomy

UNIVERSITY *of the*
WESTERN CAPE

Supervisor: Prof. Roy Maartens

Co-supervisor: Dr. Mario Ballardini

September 28, 2019

Declaration of Authorship

I, WILLIAM MATTHEWSON, declare that this thesis titled, 'Probing the primordial Universe using the SKA in combination with other cosmological surveys' and the work presented in it are my own. I confirm that:

- This work was done wholly or mainly while in candidature for a research degree at this University.

- Where any part of this thesis has previously been submitted for a degree or any other qualification at this University or any other institution, this has been clearly stated.

- Where I have consulted the published work of others, this is always clearly attributed.

- Where I have quoted from the work of others, the source is always given. With the exception of such quotations, this thesis is entirely my own work.

- I have acknowledged all main sources of help.

- Where the thesis is based on work done by myself jointly with others, I have made clear exactly what was done by others and what I have contributed myself.

- Chapter 5 and the elements from Chapter 4 concerning the peak-background split are based on a paper (accepted by MNRAS) co-authored with my supervisors [115].
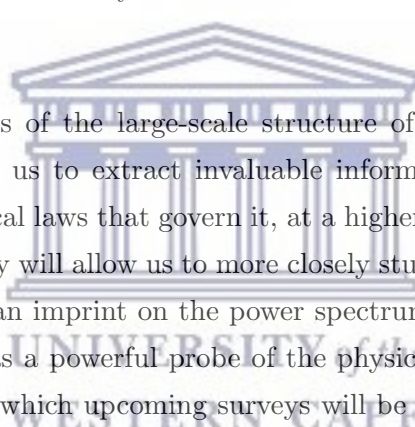
Signed:

Date: 28/09/2019

Abstract

Master of Science

by William Matthewson

Next-generation surveys of the large-scale structure of the Universe will be of great importance in allowing us to extract invaluable information about the nature of the Universe and the physical laws that govern it, at a higher precision than previously possible. In particular, they will allow us to more closely study primordial non-Gaussianity, a feature which leaves an imprint on the power spectrum of galaxies on the ultra-large scales and which acts as a powerful probe of the physics of the early Universe. To investigate the extent to which upcoming surveys will be able to improve our knowledge of primordial non-Gaussianity, we perform a forecast to predict the observational constraints on local-type primordial non-Gaussianity, as well as an extension that includes a scale dependence. We study the constraining power of a multi-tracer approach, where information from different surveys is combined to help suppress cosmic variance and break parameter degeneracies. More specifically, we consider the combination of a 21cm intensity mapping survey with each of two different photometric galaxy surveys, and also examine the effect of including CMB lensing as an additional probe. The forecast constraint from a combination of SKA1, a Euclid-like (LSST-like) survey and a CMB Stage 4 lensing experiment is $\sigma(f_{\mathrm{NL}}) \simeq 0.9$ (1.4) which displays a factor of 2 improvement over the case without CMB lensing, indicating that the surveys considered are indeed complementary. The constraints on the running index of the scale-dependent model are forecast as $\sigma(n_{\mathrm{NL}}) \simeq 0.12$ (0.22) from the same combination of surveys.

Acknowledgements

I would like to express my gratitude to the members of the Physics and Astronomy department of University of the Western Cape for all of their support. In particular, I would like to thank my supervisor Prof Roy Maartens and co-supervisor Dr Mario Ballardini for their guidance and assistance during my MSc. I could not have asked for more knowledgeable or caring direction and I have learnt a great deal from both of them. In addition, the financial assistance of the South African Radio Astronomy Observatory (SARAO) towards this MSc. is hereby acknowledged (www.ska.ac.za). Finally, I would like to thank my parents for their continued encouragement and support of everything I do - at last I have my "Thing".

UNIVERSITY *of the*
WESTERN CAPE

iii

Contents

Abbreviations

Acronym	Meaning
Angular	**P**ower **S**pectrum
CMB	**C**osmic **M**icrowave **B**ackground
CMB-S4	**CMB S**tage **4** experiment
EoS	**E**quation **o**f **S**tate
FLRW	**F**riedmann-**L**emaître-**R**obertson-**W**alker
GR	**G**eneral **R**elativity
HI	Neutral (**I**) **H**ydrogen
IM	**I**ntensity **M**apping
ΛCDM	**L**ambda **C**old **D**ark **M**atter
LSS	**L**arge-**S**cale **S**tructure
LSST	**L**arge **S**ynoptic **S**urvey **T**elescope
PBS	**P**eak **B**ackground **S**plit
2PCF	2-**P**oint **C**orrelation **F**unction
PNG	**P**rimordial **n**on-**G**aussianity
RSD	**R**edshift **S**pace **D**istortions
SKA	**S**quare **K**ilometre **A**rray

Chapter 1

Overview

The current widely-accepted description of the origin and evolution of our Universe is known as the Λ-Cold Dark Matter (ΛCDM) model. It is the purpose of this chapter to explain a series of simpler models, building up incrementally to a full description of the ΛCDM. The goal is a model that describes an expanding Universe comprising various fluid components, each governed by an equation of state. The model begins with a "Big Bang" where the Universe starts expanding from a singularity of infinite density and the evolution of the physical size of the Universe is controlled by the relative energy densities of these fluid components. There is a relativistic component which consists of photons and relativistic particles, a matter component which comprises both visible, baryonic matter and non-interacting (cold) dark matter, which is not directly observable, and finally a cosmological constant component Λ which acts like a fluid with negative pressure.

Shortly after the Big Bang a brief period of extreme expansion known as inflation occurs, bringing primordial quantum fluctuations to a macroscopic scale and providing the seeds for the formation of structure that follows. The model assumes that the Universe is statistically isotropic and homogeneous on large scales, and has flat curvature. There are 6 independent parameters on which the model depends. Together with their values from 2018 Planck observations, these are: the cold dark matter density parameter $\Omega_{c0} = 0.120 \pm 0.001$, the baryon density parameter $\Omega_{b0} = 0.0224 \pm 0.0001$, the scalar spectral index $n_s = 0.965 \pm 0.004$, the curvature fluctuation amplitude $\ln(10^{10} A_s) = 3.044 \pm 0.014$,

<div align="center">1</div>

the Hubble parameter $H_0 = 67.4 \pm 0.5 km s^{-1} Mpc^{-1}$ and the reionization optical depth $\tau = 0.054 \pm 0.007$ [29].

1.1   A brief history

Before we introduce the mathematical model for the Universe, we begin by presenting a summary of the evolution of the Universe according to the ΛCDM model (see Fig. 1.1 for a graphic depiction).

The Universe began expanding from an infinitely dense singularity in what is known as the Big Bang. During the earliest times, the length-scale of the observable Universe was comparable to the Planck scale and would have been dominated by quantum effects. The exact nature of the physical laws governing the Universe during this time is unknown, but it is expected that the fundamental forces were unified through a Grand Unified Theory (GUT) during this high energy regime. The ΛCDM model also includes a period known as inflation which was a brief, extremely rapid expansion and is motivated by various observations. [1, 2]

As the Universe quickly expanded and cooled, the forces began to "freeze out", becoming the distinct gravitational, strong, weak and electromagnetic forces. Elementary particles such as quarks also started to form and, by approximately 3 minutes after the Big Bang, nuclei had formed. During this time, the energy density of radiation was the dominant component and the Universe was filled with a hot plasma of tightly-coupled photons, protons and electrons. Unlike the energy density of matter, which scales like the inverse power of 3 with the size of the universe, the energy density of radiation scales like the inverse power of 4 and thus decreases proportionately quicker as the Universe expands. So, as the Universe ages, the radiation component decreases with respect to the matter component until the matter component is dominant, allowing for the formation of structure. [1, 2]

Approximately 300 000 years after the big bang, the Universe had cooled sufficiently that matter and radiation could decouple: Hydrogen atoms began to form and photons were free to stream through the Universe. This period is known as recombination and is responsible for the photons that form the surface of last scattering that we observe

as the Cosmic Microwave Background, a remnant of this early stage of the Universe's evolution. [1, 2, 9–12]

The atomic matter (mostly Hydrogen) that began to form at this stage would, through the complex process of structure formation, eventually go on to become the galaxies that we observe in the Universe today. However, it was only after a long period called the cosmic Dark Ages that the first stars and galaxies were able to form [13].
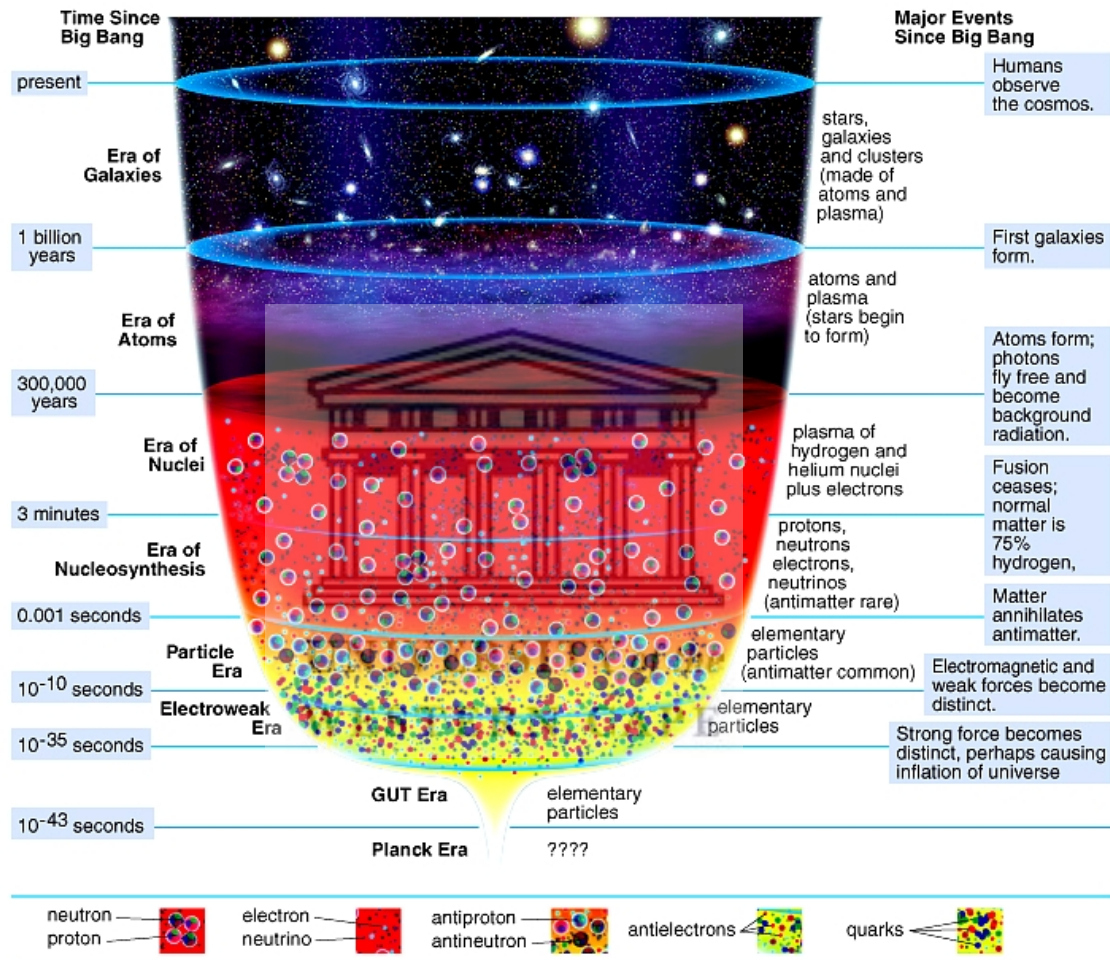

FIGURE 1.1: A summary of the evolution of the Universe (from [14]).
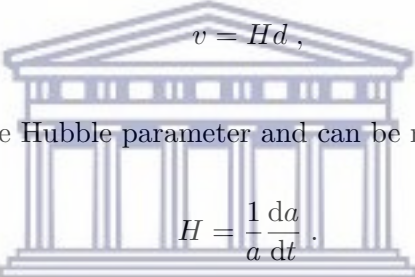
1.2 The Big Bang model

According to observations, we inhabit an expanding Universe. In order to quantify this expansion, we define the scale factor a such that [1]:

$$d(t) = a(t)\chi \, , \tag{1.1}$$

where d is the physical distance measured between two points and must increase with the expansion, whereas χ is the comoving distance, which is the spatial coordinate distance between two points in a reference frame that expands with the Universe. If the points maintain their coordinates, then the comoving distance must remain constant in time. Thus a must grow with time, controlling the growth of d. The time t introduced here is the cosmic time or coordinate time, which is measured from an observer's reference frame. It is also useful to define the proper time τ, which is equivalent to the time measured in the instantaneous rest-frame of an event, so that the proper time interval between two events is an invariant quantity.

Observations show that galaxies are moving away from us according to Hubble's law, where for small d the recessional velocity of each galaxy is dependent on the distance from the observer to the galaxy [2]:

$$v = Hd \,, \tag{1.2}$$

where H is known as the Hubble parameter and can be related to the scale factor by

$$H = \frac{1}{a}\frac{\mathrm{d}a}{\mathrm{d}t} \,. \tag{1.3}$$

If we follow the evolution of the Universe backwards into the past, a must decrease. This suggests that our expanding Universe began from a singularity of infinite density. Other observations, such as the Cosmic Microwave Background (CMB) indicate that the Universe is not expanding in a steady state, but evolving as it expands [2]. The standard model to describe this kind of Universe is known as the "Hot Big Bang" model and has been successful in explaining such observations as Hubble's law, the CMB, the formation of the large-scale structure and the proportional abundance of the light elements. However, in the absence of any matter beyond that which we directly observe around us, such a model is only able to predict a Universe with a decelerating expansion. This raises some problems, due to other observations that have been made. These include, chiefly:
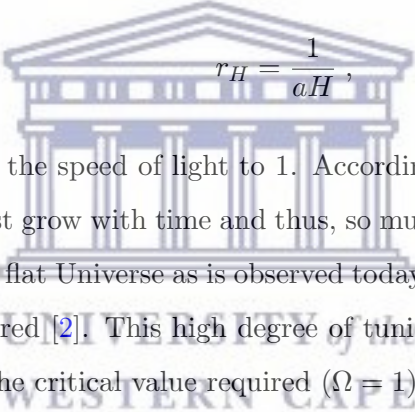
- *The Horizon problem*: The radiation of the CMB that we observe today is statistically homogeneous and isotropic [3]. This is true even when we compare patches on the sky sufficiently far apart, according to the model of the Big Bang we have

described so far, as to be outside of causal contact for all times up to the point in the early Universe when the CMB signal was created. What our observation implies is that somehow these different regions must have been in causal contact for a sufficiently long period before the time of last scattering for the photons to reach equilibrium before being emitted.

- *The Flatness problem*: The Universe that we observe today is spatially flat [4]. That means that it is geometrically Euclidean. The curvature of the Universe can be specified (see (1.31)) by [3]

$$1 - \Omega(t) \propto r_{\mathrm{H}}^2(t) \; , \tag{1.4}$$

where $\Omega(t)$ is the total energy density (including matter, radiation and dark energy) of the Universe at a particular time, and r_H is the comoving Hubble radius, i.e.

$$r_H = \frac{1}{aH} \; , \tag{1.5}$$

where we have set the speed of light to 1. According to the Big Bang model, the Hubble radius must grow with time and thus, so must the curvature. In order that we measure such a flat Universe as is observed today, a very finely-tuned curvature parameter is required [2]. This high degree of tuning is not predicted by the Big Bang model and the critical value required ($\Omega = 1$) is an unstable point [5].

Although it is not immediately obvious, both of these problems share one common feature. In the case of the horizon problem we require that particles be brought back into causal contact with each other as we move backwards in time. From the definition of the comoving Hubble radius, it can be said that particles which are within the radius will be in causal contact with one another. Thus, we would require the Hubble radius to grow as we move *backwards* in time, to incorporate patches on completely opposite sides of the sky. This means that we would require a period in the early Universe when r_H shrinks as time progresses forwards. Similarly, in the case of the flatness problem, a shrinking r_H would result in a decrease in the curvature towards flatness, even if it was not initially tuned [2]. Therefore, a solution to both of these problems lies in incorporating a period with decreasing r_H into the evolution of the Universe at early times. Cosmic inflation is one such approach [6].

1.3 Inflation

Since we require a period where the comoving Hubble radius is decreasing in time, we have the following restriction:

$$\frac{\mathrm{d}r_H}{\mathrm{d}t} < 0 \,, \tag{1.6}$$

which leads to

$$\frac{\mathrm{d}^2 a}{\mathrm{d}t^2} > 0 \,, \tag{1.7}$$

from the definition (1.5) as well as the restrictions that $a > 0$ and that the Universe is constantly expanding $\mathrm{d}a/\mathrm{d}t > 0$.

Thus, we can include in the model for the Big Bang a brief period of accelerated expansion at early times, called inflation. This will solve both the horizon and flatness problems at once. During inflation the Universe expansion accelerates extremely rapidly. Subsequently, measurable physical length scales are much smaller than the resultant scale of the observable Universe, meaning that all patches of the CMB sky have been in prior causal contact and that the measured curvature is reduced to very nearly flat.

The simplest and most commonly adopted model of inflation is known as slow-roll inflation [7]. In this type of model, the scalar (inflaton) field responsible for inflation varies slowly, resulting in a slowly decreasing Hubble rate [1, 2]. Inflation proceeds while the potential energy of the scalar field exceeds its kinetic energy [8].

Not only does the incorporation of an inflationary period help to resolve the horizon and flatness problems, but it also provides a mechanism by which primordial quantum fluctuations can be frozen out into the fluctuations that eventually lead to the anisotropies in the CMB and the formation of structure on large scales [1].

Thus, we can set the initial conditions for these anisotropies from the primordial curvature fluctuations that are enlarged during inflation [16]. With this in mind, it is convenient to define the power spectrum associated with the primordial fluctuations. In most cases, single-field models of inflation are Gaussian random with almost scale-invariant dimensionless power spectra of the form [18, 19]

$$\mathcal{P}_\zeta(k) = A_s \left(\frac{k}{k_*}\right)^{n_s - 1} \,, \tag{1.8}$$

where ζ is the primordial curvature perturbation, $n_s \sim 1$ is the spectral index, A_s is the scalar amplitude, k is the wavenumber and k_* is the pivot scale. The assumption that the perturbations are Gaussian can be relaxed, and indeed we define a parameter later that controls the primordial non-Gaussianity (see Chapter 4).

After inflation had amplified the primordial fluctuations, and once radiation and matter had decoupled, the initial conditions for structure formation were set. The anisotropies visible in the CMB were also present in the form of perturbations in the density field of matter, creating gravitational instabilities essential for the formation of structure.

1.4 Structure formation

Structures in the Universe exist over a very wide range of scales, from stars to galaxy clusters, and are formed from matter. In particular, they are formed from overdensities in the matter density field which are seeded by primordial fluctuations, passed on to the matter via the coupling with photons and amplified by the action of gravity [16, 17]. This leads to a particularly characteristic pattern, known as the cosmic web, that is visible in the large-scale structure (LSS) which Figure 1.2 displays using the distribution of galaxies in the Universe.

The perturbations present in the dark matter density result in gravitational instabilities. In order for structures to form, matter must come together in dense clumps that eventually form stars and galaxies. Gravitational forces assist in this regard, attracting matter together to enhance the overdensities in the matter field. However, the entire process is more complex than the individual action of gravity, since there are various mechanisms that oppose the gravitational collapse of matter overdensities: namely, the expansion of the Universe and the outwards pressure of photons when the radiation energy density is sufficiently high. These factors work against gravity to decrease the strength of the overdensities above the background and thereby prevent or slow the formation of structure. Thus, it is only over time, through a complex interplay between the attraction of gravitational forces and the repulsion of radiation pressure set against the expanding background, that the perturbations lead to the formation of small dark matter halos. Once formed, these are able to gravitationally attract baryonic matter, which clumps together, eventually merging to form galaxies [1, 17]. These too attract
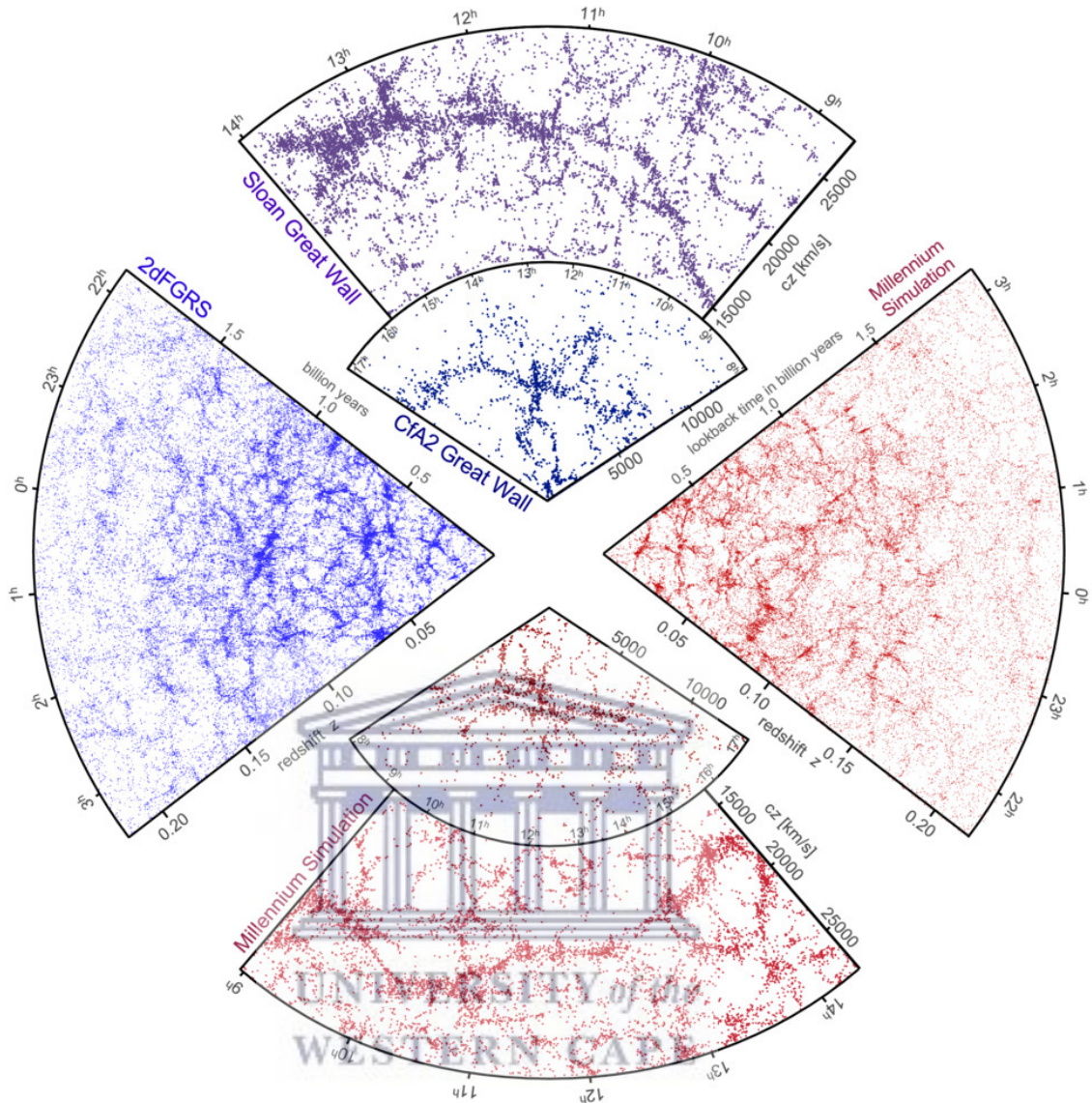
FIGURE 1.2: The cosmic web visible in the galaxy distribution of real data from spectroscopic redshift surveys (blue and purple) and of synthetic data from cosmological simulations (red) (from [15]).

each other to form galaxy clusters, which form part of the cosmic web we see in the large-scale structure.

In order to describe the formation of structure due to gravitational interactions on large scales, we must use the framework of General Relativity. First, we must choose a suitable metric and then apply the Einstein field equations so that we can determine the evolution of the scale factor and matter density field.

1.5 The FLRW universe

The standard metric used in a cosmological description is known as the Friedmann-Lemaître-Robertson-Walker (or FLRW) metric and is given by [22, 23]

$$\mathrm{d}\bar{s}^2 = -\mathrm{d}t^2 + a^2(t)\left(\frac{\mathrm{d}\bar{\chi}^2}{1 - K\bar{\chi}^2} + \bar{\chi}^2\mathrm{d}\theta^2 + \bar{\chi}^2\sin^2\theta\mathrm{d}\phi^2\right) , \qquad (1.9)$$

where t is the cosmic time, a is the scale factor as defined previously and $(\bar{\chi}, \theta, \phi)$ are the comoving radial and angular coordinates for a sphere centred at an arbitrarily chosen observer. The curvature parameter K can take a positive, zero or negative value corresponding to a closed (spherical), flat or open (hyperbolic) universe, respectively.

There are two fundamental constraining assumptions about the nature of the Universe, constituting the Cosmological Principle, which states that on sufficiently large scales ($\gtrsim 100$ Mpc), we have [2]:

- Statistical Isotropy: This means that the characteristics of the Universe don't change as a function of the direction in which the observer is looking. Hence, measured observables must be rotation-invariant on large scales.

- Statistical Homogeneity: This means that the properties of the Universe do not change if measured at different points in space. Hence, every observable must be translation-invariant on large scales.

The FLRW metric has exactly isotropic and homogeneous $t = $ const spatial surfaces and so it is the correct background metric to describe perturbations in radiation and matter. The assumptions of the Cosmological Principle are also well-supported by our observations. Observations of the CMB display evidence of statistical isotropy: The averaged temperature of CMB photons from different patches in the sky is almost the same ($T_{\mathrm{CMB}} = 2.73$ K, with relative fluctuations of the order 10^{-5}) independent of the direction of observation [21]. An FLRW background with linear perturbations leads to a good description of the CMB physics on small angular scales.

1.5.1 The background solution

Initially, we consider a universe conforming to the assumptions we have made and characterised by the average background quantities, which are without perturbations. We then solve the associated Einstein field equations to determine the dynamics and evolution. Note that the background quantities will be denoted in general with an overbar, e.g. $\bar{\chi}$.

1.5.1.1 Einstein's field equations

Since the scale factor controls the physical size of the Universe, once we determine the dependence of a on t, we have a description of how the Universe evolves over time. This solution comes from solving the Einstein field equations, given by

$$\bar{G}_{\mu\nu} + \Lambda \bar{g}_{\mu\nu} = 8\pi G \bar{T}_{\mu\nu} , \qquad (1.10)$$

where $\bar{g}_{\mu\nu}$ is the background metric, Λ is called the cosmological constant and the Einstein tensor $\bar{G}_{\mu\nu}$ is defined as

$$\bar{G}_{\mu\nu} = \bar{R}_{\mu\nu} - \frac{1}{2}\bar{g}_{\mu\nu}\bar{R} , \qquad (1.11)$$

where $\bar{R}_{\mu\nu}$ and $\bar{R}$ are the Ricci tensor and Ricci scalar, respectively. The Ricci tensor is obtained from the Christoffel symbols $\bar{\Gamma}^{\lambda}{}_{\mu\nu}$ as follows: [1]

$$\bar{R}_{\mu\nu} = \partial_{\lambda}\bar{\Gamma}^{\lambda}{}_{\mu\nu} - \partial_{\nu}\bar{\Gamma}^{\lambda}{}_{\lambda\mu} + \bar{\Gamma}^{\lambda}{}_{\lambda\sigma}\bar{\Gamma}^{\sigma}{}_{\mu\nu} - \bar{\Gamma}^{\lambda}{}_{\sigma\nu}\bar{\Gamma}^{\sigma}{}_{\lambda\mu} , \qquad (1.12)$$

where the Christoffel symbols are related to the metric tensor $\bar{g}_{\mu\nu}$ by [1, 21]

$$\bar{\Gamma}^{\lambda}{}_{\mu\nu} = \frac{1}{2}\bar{g}^{\lambda\sigma} \left(\partial_{\mu}\bar{g}_{\nu\sigma} + \partial_{\nu}\bar{g}_{\mu\sigma} - \partial_{\sigma}\bar{g}_{\mu\nu} \right) . \qquad (1.13)$$

The term containing Λ in the Einstein field equations arises as an integration constant and, depending on which side of the equation it is added to, can be thought of as a geometrical effect or as another component of the energy density, known as "dark energy". In the case of the latter, this component can be used to explain particular observations concerning the expansion of the Universe. Measurements of the luminosity distances of

type Ia supernovae (SNIa) show that the Universe is accelerating in its expansion [24]. However, as will be seen, ordinary matter causes the expansion of the Universe to slow with time, since the attractive action of gravity opposes the expansion. Thus, there is a concerted effort underway to try understand and describe this acceleration, including surveys such as the Baryon Acoustic Oscillation Spectroscopic Survey (BOSS) [25] and Dark Energy Survey (DES) [26].

Returning to the field equations, the non-zero Christoffel symbols for the particular metric given in (1.9) are [23]:

$$
\begin{aligned}
&\bar{\Gamma}^0{}_{11} = \frac{a\dot{a}}{1 - K\bar{\chi}^2} \;, && \bar{\Gamma}^0{}_{22} = a\dot{a}\bar{\chi}^2 \;, \\
&\bar{\Gamma}^0{}_{33} = a\dot{a}\bar{\chi}^2 \sin^2\theta \;, && \bar{\Gamma}^1{}_{01} = \bar{\Gamma}^2{}_{02} = \bar{\Gamma}^3{}_{03} = \frac{\dot{a}}{a} \;, \\
&\bar{\Gamma}^1{}_{11} = \frac{K\bar{\chi}}{1 - K\bar{\chi}^2} \;, && \bar{\Gamma}^1{}_{22} = -\bar{\chi}\left(1 - K\bar{\chi}^2\right) \;, \\
&\bar{\Gamma}^1{}_{33} = -\bar{\chi}\left(1 - K\bar{\chi}^2\right)\sin^2\theta \;, && \bar{\Gamma}^2{}_{33} = -\sin\theta\cos\theta \;, \\
&\bar{\Gamma}^2{}_{12} = \bar{\Gamma}^3{}_{13} = \frac{1}{\bar{\chi}} \;, && \bar{\Gamma}^3{}_{23} = \cot\theta \;.
\end{aligned}
\tag{1.14}
$$

The non-zero elements of the Ricci tensor, calculated from (1.12), are [23]:

$$
\begin{aligned}
&\bar{R}_{00} = -3\left(\dot{H} + H^2\right) \;, && \bar{R}_{11} = \frac{a^2}{1 - K\bar{\chi}^2}\left(\dot{H} + 3H^2 + \frac{2K}{a^2}\right) \;, \\
&\bar{R}_{22} = a^2\bar{\chi}^2\left(\dot{H} + 3H^2 + \frac{2K}{a^2}\right) \;, && \bar{R}_{33} = a^2\bar{\chi}^2\sin^2\theta\left(\dot{H} + 3H^2 + \frac{2K}{a^2}\right) \;,
\end{aligned}
\tag{1.15}
$$

where $H = \frac{\dot{a}}{a}$ is the Hubble parameter and $\dot{a} = \frac{\mathrm{d}a}{\mathrm{d}t}$[1]. Hence, the Ricci scalar is given by [23]

$$
\bar{R} = 6\left(\dot{H} + 2H^2 + \frac{K}{a^2}\right) \;.
\tag{1.16}
$$

$\bar{T}_{\mu\nu}$ in (1.9) is the energy momentum tensor of a perfect fluid and is given by [1]

$$
\bar{T}_{\mu\nu} = \left(\bar{\rho}_{tot} + \bar{p}_{tot}\right)\bar{u}_\mu\bar{u}_\nu + \bar{p}_{tot}\bar{g}_{\mu\nu} \;,
\tag{1.17}
$$

where $\bar{\rho}_{tot}$ and $\bar{p}_{tot}$ are respectively the total energy density and pressure of the fluid components contained in the Universe and $\bar{u}_\mu = \frac{\mathrm{d}x^\mu}{\mathrm{d}\tau}$ is the 4-velocity of the fluid. We

---

[1]Once the conformal time is introduced, derivatives denoted with primes will be taken to mean derivatives with respect to the conformal time

may approximate the components as perfect fluids for most periods in the evolution of the Universe, since the anisotropic dissipative terms such as heat flux, viscosity or anisotropic pressure are negligible [2]. The physical interpretations of the components of $T_{\mu\nu}$ are as follows:

- T^{00} is the energy density

- T^{0i} and T^{0i} are both equivalent to the mass flux across the surface of a volume element with normal vector $\boldsymbol{n} = \hat{x}_i$

- T^{ij} is the flux across the surface, with normal $\boldsymbol{n} = \hat{x}_j$, of the ith component of the momentum. If $i \neq j$ this is known as a shear and if $i = j$ this is the pressure.

As discussed, we may treat the cosmological constant term $\Lambda \bar{g}_{\mu\nu}$ of (1.10) as another component of the energy density and thus we absorb it into $\bar{T}_{\mu\nu}$: the energy density and pressure $\bar{\rho}_{tot}$ and $\bar{p}_{tot}$ are redefined as $\bar{\rho}_{tot} + \bar{\rho}_\Lambda \rightarrow \bar{\rho}_{tot}$ and $\bar{p}_{tot} - \bar{p}_\Lambda \rightarrow \bar{p}_{tot}$, where

$$\bar{p}_\Lambda = \frac{\Lambda}{8\pi G} = -\bar{\rho}_\Lambda \tag{1.18}$$

follows from the equation of state for the Λ component. In the following we suppress the subscript *tot* for brevity and, unless otherwise stated, take $\bar{\rho}$ and $\bar{p}$ to mean the total background energy density and pressure. The field equations now read:

$$\bar{G}_{\mu\nu} = 8\pi G \bar{T}_{\mu\nu} . \tag{1.19}$$

For a comoving observer, $\bar{u}_\mu = (-1, \boldsymbol{0})$, which gives:

$$\bar{T}_{00} = \bar{\rho} , \qquad\qquad \bar{T}_{11} = \frac{\bar{p}a^2}{1 - K\bar{\chi}^2} ,$$

$$\bar{T}_{22} = \bar{p}a^2\bar{\chi}^2 , \qquad\qquad \bar{T}_{33} = \bar{p}a^2\bar{\chi}^2\sin^2\theta . \tag{1.20}$$

It is then possible to write the Einstein field equations, using (1.14), (1.15) and (1.20) to obtain the following system of equations for the evolution of the scale factor [23]:

$$H^2 = \frac{8\pi G\bar{\rho}}{3} - \frac{K}{a^2} , \tag{1.21}$$

$$H^2 + \dot{H} = -\frac{4\pi G}{3}(\bar{\rho} + 3\bar{p}) . \tag{1.22}$$

The first equation (1.21) is known as the **Friedmann equation** and (1.22) is known as the **Raychaudhuri equation**, and together these equations form the basis for the description of the evolution of the background. If we assume a barotropic model for each component in the Universe, with an equation of state (EoS) for component X given by [1, 21]:

$$\bar{p}_X = w_X \bar{\rho}_X \, , \tag{1.23}$$

then the EoS parameter w will have the following values for different kinds of components

- $w_m = 0$ for non-relativistic matter,

- $w_r = 1/3$ for thermal radiation or a gas of relativistic particles, and

- $w_\Lambda = -1$ for a cosmological constant.

Therefore, incorporating the EoS parameter in (1.22) for component X, we obtain

$$H^2 + \dot{H} = -\frac{4\pi G}{3} \left(1 + 3w_X\right) \bar{\rho}_X \, . \tag{1.24}$$

We can use the Raychaudhuri equation (1.24) to determine that the requirement for the observed accelerating expansion is $w < -1/3$ which, using the EoS, corresponds to a negative pressure:

$$\bar{p} < -\frac{1}{3}\bar{\rho} \, . \tag{1.25}$$

Thus, in the case of the cosmological constant, $w_\Lambda = -1$ implies a negative pressure, which aids the expansion. We explain this physical effect as a kind of vacuum energy, proportional to spatial volume. This description has not been wholly successful thus far, since the prediction from quantum field theory is many orders of magnitude higher than the vacuum energy density we infer from observations.

We now introduce the conformal time η, defined as

$$\mathrm{d}t = a\mathrm{d}\eta \, , \tag{1.26}$$

so that the spatial scale factor becomes a conformal factor of the spacetime metric. Hereafter all derivatives denoted with a prime, e.g. a', are taken to be derivatives with

respect to the *conformal* time. We can also define the conformal Hubble parameter:

$$\mathcal{H} = \frac{1}{a}\frac{\mathrm{d}a}{\mathrm{d}\eta} = aH \ .$$

(1.27)

The Friedmann equation ((1.21)) and Raychaudhuri equation ((1.22)) then become:

$$\mathcal{H}^2 \quad = \quad \frac{8\pi G\bar{\rho}}{3}a^2 - K \ ,$$

(1.28)

$$\mathcal{H}^2 + \mathcal{H}' \quad = \quad -\frac{4\pi G}{3}\left(\bar{\rho} + 3\bar{p}\right)a^2 \ .$$

(1.29)

For convenience we define the dimensionless density parameter for component X as

$$\Omega_X(a) = \frac{8\pi G\bar{\rho}_X(a)}{3\mathcal{H}^2}a^2 \ ,$$

(1.30)

where $\bar{\rho}_X$ denotes the corresponding energy density, so that the Friedmann equation becomes

$$1 \quad = \quad \sum_X \Omega_X - \Omega_K \ ,$$

(1.31)

where we have defined $\Omega_K = K/\mathcal{H}^2$.
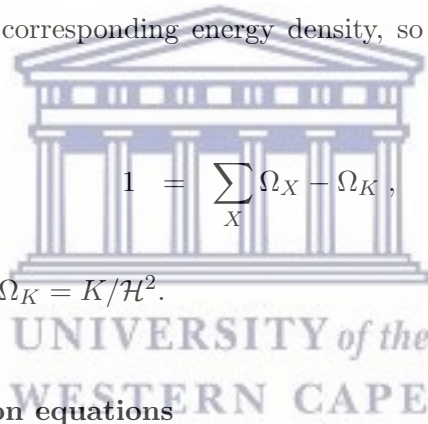
1.5.1.2   Conservation equations

From the Friedmann equation (1.21) and Raychaudhuri equation (1.24) we wish to extract a time evolution for the density ρ of each component and for the scale factor a. These are coupled non-linear differential equations and are not straightforward to solve. However, we can recover conservation equations and use them to solve for the relation between ρ and a before obtaining the time-dependence of a. The conservation of energy and momentum is ensured by the Bianchi identity, which requires that the covariant divergence of the Einstein tensor must vanish:

$$\bar{\nabla}_\nu \bar{G}^\nu_\mu = 0 \ .$$

(1.32)

From the Einstein field equations (1.10), we then obtain the following for the energy-momentum tensor:

$$\bar{\nabla}_\nu \bar{T}^\nu_\mu = 0 \ , \tag{1.33}$$

which we interpret as the conservation condition.

Using the metric to raise one of the indices and the EoS (1.23) for a single component X, (1.17) becomes

$$\bar{u}_\mu \bar{u}^\nu \bar{\nabla}_\nu \left[(1 + w_X)\bar{\rho}_X \right] + (1 + w_X)\,\bar{\rho}_X \left(\bar{u}^\nu \nabla_\nu \bar{u}_\mu + \bar{u}_\mu \nabla_\nu \bar{u}^\nu \right) + \bar{\nabla}_\mu \bar{p}_X = 0 \ . \tag{1.34}$$

If we contract (1.34) with the 4-velocity $\bar{u}^\mu$, this yields

$$\dot{\bar{\rho}}_X + \bar{\Theta}\left(1 + w_X\right)\bar{\rho}_X = 0 \ , \tag{1.35}$$

where we have used $\dot{\bar{\rho}}_X = \bar{u}^\nu \nabla_\nu \bar{\rho}_X$ and defined the volume expansion rate as [2]

$$\bar{\Theta} = \bar{\nabla}_\nu \bar{u}^\nu . \tag{1.36}$$

The comoving velocity and the Christoffel symbols for an isotropic, homogeneous universe give $\bar{\Theta} = 3H$ [23]. This leads to the equation for the conservation of energy:

$$\bar{\rho}'_X + 3\mathcal{H}\left(1 + w_X\right)\bar{\rho}_X = 0, \tag{1.37}$$

which is known as the **Continuity equation** and where we have made the change to conformal time variables.

We can also contract (1.34) with $(\bar{u}_\alpha \bar{u}^\mu + \delta^\mu_\alpha)$. This yields the other conservation equation, known as the **Euler equation**:

$$(1 + w_X)\,\bar{\rho}_X \dot{\bar{u}}_\alpha + (\bar{u}_\alpha \bar{u}^\mu + \delta^\mu_\alpha)\,\bar{\nabla}_\mu \bar{p}_X = 0 \ , \tag{1.38}$$

where $\dot{\bar{u}}_\alpha$ is the 4-acceleration vector, given by $\dot{\bar{u}}_\alpha = \bar{u}^\nu \nabla_\nu \bar{u}_\alpha$. This is a statement of the conservation of momentum and is trivially satisfied in a FLRW background: since the FLRW universe is homogeneous and isotropic, the spatial vectors $\dot{\bar{u}}_\alpha$ and $(\bar{u}_\alpha \bar{u}^\mu + \delta^\mu_\alpha)\bar{\nabla}_\mu \bar{p}_i$ must vanish, making the left-hand side of (1.38) identically 0.

TABLE 1.1: Evolution of energy density and scale factor in a flat FLRW universe for each case where a different component dominates the energy budget.

	w	$\bar{\rho}(a)$	$a(t)$
Radiation	1/3	a^{-4}	$t^{1/2}$
Matter	0	a^{-3}	$t^{2/3}$
Λ	-1	a^0	e^{Ht}

The evolution of the scale factor and the energy density can be determined by simultaneously solving (1.24) and (1.37) in various cases where different components dominate. For a flat Universe with a dominant component X, we obtain:

$$
\begin{aligned}
\bar{\rho}_X(a) &= \bar{\rho}_{X0} a^{-3(1+w_X)} , \\
a(t) &= t^{\frac{2}{3(1+w_X)}} ,
\end{aligned}
\tag{1.39}
$$

where $\bar{\rho}_{X0} = \bar{\rho}_X(a_0)$ and the scale factor is normalized to the present time $a_0 = a(t_0) = 1$. The results for each of the components discussed earlier are displayed in Table 1.1. In reality, there may not always be a single dominant component, but the single-component solutions are useful during periods where one component is dominant. In Figure 1.3, we see that the Universe begins with a radiation-dominated era, followed by matter domination and at late times the Λ component begins to dominate.

1.5.1.3   The full ΛCDM model

The model of the Universe with zero spatial curvature, containing various fluid components, each specified by their own equations of states and with dark energy parametrized by Λ, is called the Lambda Cold Dark Matter (ΛCDM) model.

Thus the Friedmann equation (1.21) can be written in conformal variables as

$$
\mathcal{H}^2 = \frac{8\pi G}{3}\Big(\bar{\rho}_m + \bar{\rho}_r + \bar{\rho}_\Lambda\Big)a^2 ,
\tag{1.40}
$$

where we have set $K = 0$ and $\bar{\rho}_m$, $\bar{\rho}_r$ and $\bar{\rho}_\Lambda$ are the respective energy densities of cold matter (cold dark matter and baryons), radiation (photons and neutrinos) and dark energy.
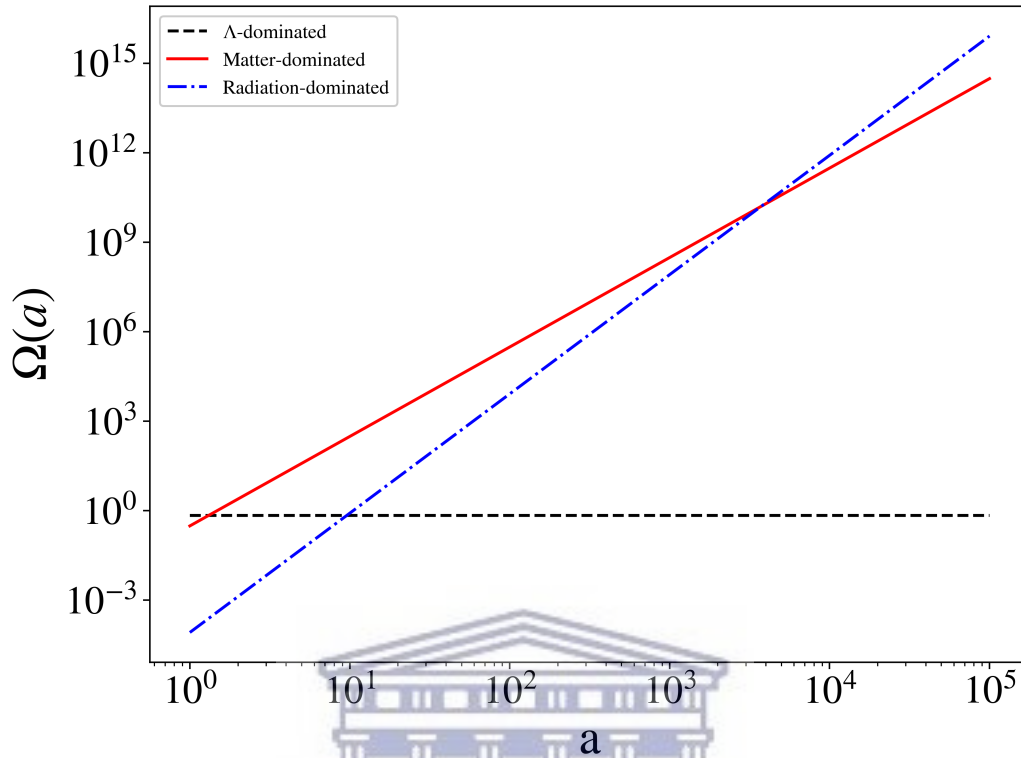
FIGURE 1.3: The evolution of the dimensionless energy (see (1.30)) densities in universes with different dominant components, normalized so that $\Omega_{tot} = 1$ today.

Using the definition of the density parameter (1.30), the Friedmann equation becomes

$$1 = \Omega_m + \Omega_r + \Omega_\Lambda . \tag{1.41}$$

In terms of the current values of the density parameters (Ω_{X0}), the Friedmann equation becomes

$$\mathcal{H}(a) = aH_0\sqrt{\Omega_{m0}a^{-3} + \Omega_{r0}a^{-4} + \Omega_{\Lambda 0}} , \tag{1.42}$$

Once again, Planck 2018 data give: $\Omega_{m0} = 0.308$, $\Omega_{r0} = 9.24 \times 10^{-5}$, $\Omega_{\Lambda 0} = 0.692$ and $H_0 = 100\,h\,\mathrm{km\,s^{-1}\,Mpc^{-1}}$ with $h = 0.6732$ [29]. For convenience this is sometimes written using $\omega_X \equiv \Omega_X h^2$

1.5.1.4   Distance measures in an expanding universe

The description of the scale factor in the first section of this chapter hints that the concept of distances in Cosmology is a subtle one. In addition to the expansion of the

Universe, we must also consider the constant, finite speed of light and the implications this has for the differences between various definitions of distance.

The comoving spatial coordinates in (1.9) are characterised as being constant for freely-falling points or particles, so that the coordinate grid expands with the expansion of the Universe. The comoving distance between two such points is the spatial coordinate at some fixed time, usually chosen as the present time t_0. If we choose $a(t_0) = 1$, then the comoving distance is equal to the physical distance at t_0. If we choose the origin of the coordinate system so that the two points are radially separated, then the physical and comoving distances between them are related by (1.1)

$$d(t) = a(t)\bar{\chi} \, , \tag{1.43}$$

where the bar indicates that we are still working in the background case.

Now consider the case of an observation where a distant galaxy recedes from an observer on Earth. If a ray of light is emitted at time t_e from the galaxy, then in an infinitesimal time increment $\mathrm{d}t$, it will travel a distance of $a(t)\mathrm{d}\bar{\chi}$ *towards* the Earth. Taking the speed of light as 1, this gives

$$-a\mathrm{d}\bar{\chi} = \mathrm{d}t \, . \tag{1.44}$$

Hence,

$$\bar{\chi} = \int_{t_e}^{t_o} \frac{\mathrm{d}t}{a(t)} \tag{1.45}$$

is the comoving distance that the light travels to reach the observer on Earth at t_o.

By virtue of its motion, the receding galaxy induces a change in the wavelength of the light ray measured by the observer. This change can be described using the redshift $\bar{z}$ which is related to the scale factor by [1]

$$1 + \bar{z} = \frac{a_0}{a(t)} \, , \tag{1.46}$$

where a_0 is the scale factor at the present time, conventionally taken to be 1. Thus, in terms of redshift, (1.45) becomes

$$\bar{\chi}(\bar{z}) = \int_0^{\bar{z}} \frac{\mathrm{d}z'}{H(z')} = \int_0^{\bar{z}} \frac{\mathrm{d}z'}{H_0\sqrt{\Omega_{m0}(1+z')^3 + \Omega_{r0}(1+z')^4 + \Omega_{\Lambda 0}}} \, , \tag{1.47}$$

where we have used cosmological time to save including an extra factor of a.

Another measure of distance is the angular diameter distance $\bar{d}_A$, which is defined as the square root of the ratio between the intrinsic area of a source and the solid angle it subtends at the observer. In terms of the comoving distance, this is given by [30, 31]

$$\bar{d}_A = \frac{\bar{\chi}}{1 + \bar{z}} \ . \tag{1.48}$$
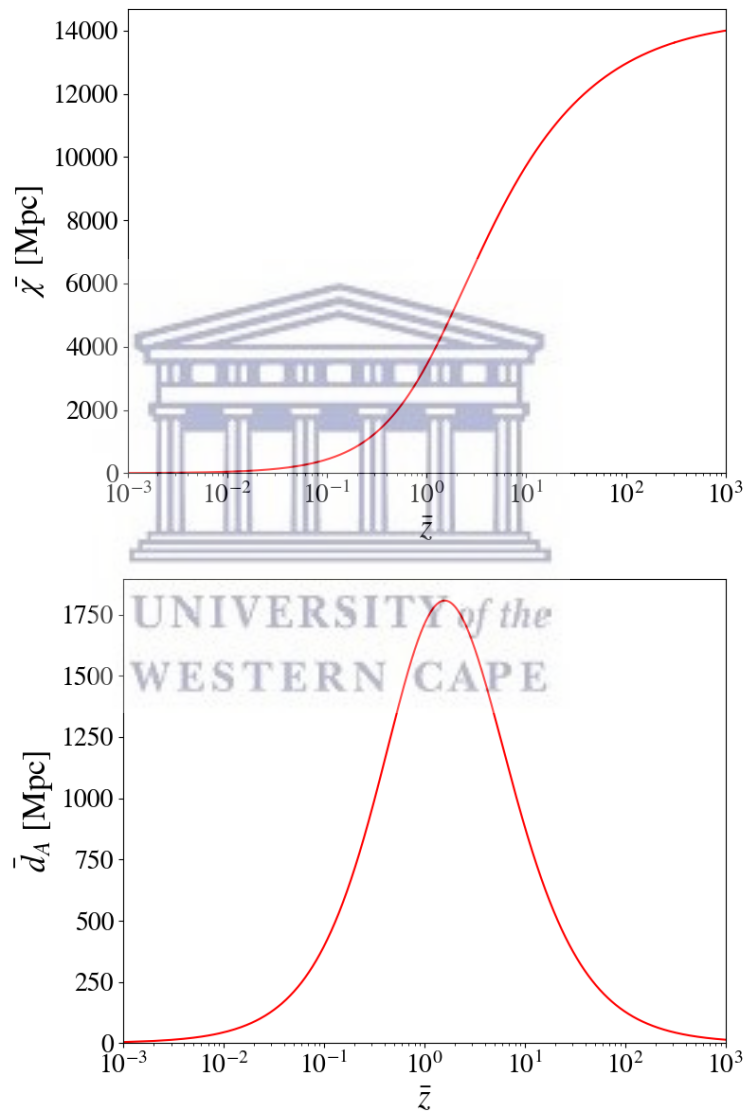
FIGURE 1.4: *Upper panel:* The comoving distance $\bar{\chi}$ plotted as a function of the background redshift $\bar{z}$. *Lower panel:* The angular diameter distance $\bar{d}_A$ plotted as a function of the background redshift, with maximum value at $\bar{z} \sim 1.6$.

Figure 1.4 shows results of numerical calculations of these two distances in the ΛCDM

model. From the figure we see that the comoving distance increases rapidly at low red-shifts and at high redshifts asymptotically approaches a maximum, whereas the angular diameter distance has a maximum at a particular redshift in an FLRW background, tapering off on either side and thus making it possible for objects to have the same $\bar{d}_A$ while being at two different redshifts.

1.5.2 The perturbed FLRW universe

We now move to the derivation of the evolution equations in a flat FLRW universe, where first-order linear perturbations have been added on top of the background. This is the simplest model necessary to be able to discuss the fluctuations observed in the Universe, but is nonetheless an effective tool for doing so.

If we consider the full metric tensor $g_{\mu\nu}$ that contains all the information about the observed Universe, then we can make a Taylor expansion about the FLRW background:

$$g_{\mu\nu} = \bar{g}_{\mu\nu} + \delta g^{(1)}_{\mu\nu} + \frac{1}{2}\delta g^{(2)}_{\mu\nu} + ... \tag{1.49}$$

Thus, to first order in perturbation, we have

$$g_{\mu\nu} = \bar{g}_{\mu\nu} + \delta g_{\mu\nu}, \tag{1.50}$$

where $\delta g_{\mu\nu} \equiv \delta g^{(1)}_{\mu\nu}$ is taken as the first-order perturbation hereafter.

The most general perturbed FLRW metric is given (in Poisson gauge) by [32, 33]

$$ds^2 = a^2 \Big[\underbrace{-(1+2\Phi)\mathrm{d}\eta^2 + (1-2\Psi)\delta_{ij}\mathrm{d}x^i\mathrm{d}x^j}_{\text{scalar part}} + \underbrace{2w_i\mathrm{d}x^i\mathrm{d}\eta}_{\text{vector part}} + \underbrace{\frac{1}{2}h_{ij}\mathrm{d}x^i\mathrm{d}x^j}_{\text{tensor part}} \Big] , \tag{1.51}$$

which allows for scalar, vector and tensor (gravitational waves) perturbations. In the following analysis we consider only scalar perturbations.

The next step is to re-derive the evolution equations by applying the Einstein field equations with the perturbed metric (1.50), using the background equations to isolate equations in the perturbations of variables and neglecting terms of second order or higher in perturbation.

1.5.2.1 Perturbed Einstein field equations

We consider a perturbed metric that assumes the following form:[2]

$$\mathrm{d}s^2 = a^2\big[-(1+2\Phi)\mathrm{d}\eta^2 + (1-2\Psi)\delta_{ij}\mathrm{d}x^i\mathrm{d}x^j\big]\ , \tag{1.52}$$

where the first-order variables Φ and Ψ are known as the Bardeen potentials and in our case we assume that there is no anisotropic stress, which means $\Psi = \Phi$ [2]. Hence, the non-zero Christoffel symbols from (1.13) are:

$$\begin{aligned}
\Gamma^0{}_{00} &= \mathcal{H} + \Phi'\ , & \Gamma^0{}_{0i} &= \partial_i\Phi\ , \\
\Gamma^i{}_{00} &= \delta^{ij}\partial_j\Phi\ , & \Gamma^0{}_{ij} &= \big[\mathcal{H} - \Phi' - 4\mathcal{H}\Phi\big]\delta_{ij}\ , \\
\Gamma^i{}_{j0} &= (\mathcal{H} - \Phi')\delta^i{}_j\ , & \Gamma^i{}_{jk} &= -2\delta^i{}_j\partial_k\Phi + \delta_{jk}\delta^{il}\partial_l\Phi\ ,
\end{aligned} \tag{1.53}$$

where we have already made the change to conformal time variables: Φ' denotes the derivative of Φ with respect to η and $\mathcal{H}$ is the conformal Hubble parameter. Then, the background Friedmann equation (from (1.28)) is

$$\mathcal{H}^2 = \frac{8\pi G a^2}{3}(\bar{\rho}_m + \bar{\rho}_r) + \frac{a^2\Lambda}{3}\ . \tag{1.54}$$

Recall $\Lambda = 8\pi G\bar{\rho}_\Lambda$. Similarly, in conformal variables, the Raychaudhuri equation (1.24) becomes

$$\mathcal{H}' = -\frac{4\pi G a^2}{3}\left(\bar{\rho}_m + \frac{2}{3}\bar{\rho}_r\right) + \frac{a^2\Lambda}{3}\ . \tag{1.55}$$

With the perturbed Christoffel symbols from (1.53), the non-zero elements of the Ricci tensor are calculated from (1.12) as:

$$\begin{aligned}
R_{00} &= -3\mathcal{H}' + \nabla^2\Phi + 6\mathcal{H}\Phi' + 3\Phi''\ , \tag{1.56}\\
R_{0i} &= 2(1+\mathcal{H})\partial_i\Phi\ , \tag{1.57}\\
R_{ij} &= \big[\mathcal{H}' + 2\mathcal{H}^2 - \Phi'' + \nabla^2\Phi - 4(\mathcal{H}' + 2\mathcal{H}^2)\Phi - 6\mathcal{H}\Phi'\big]\delta_{ij}\ ,
\end{aligned}$$

which yields the following for the Ricci scalar:

$$R = \frac{1}{a^2}\big[6(\mathcal{H}' + \mathcal{H}^2) + 2\nabla^2\Phi - 12(\mathcal{H}' + \mathcal{H}^2)\Phi - 6\Phi'' - 24\mathcal{H}\Phi'\big]\ . \tag{1.58}$$

---

[2]This metric is different to the one used in [115] and as a result some of the definitions in this work are different.

The perturbed 4-velocity is given by [1, 2]

$$u^\mu = \frac{1}{a}(1 - \Phi, \, v^i) \, , \tag{1.59}$$

using the normalization $g_{\mu\nu}u^\mu u^\nu = -1$. Here v^i is the peculiar velocity and is curl-free, meaning that

$$v^i = \partial^i V \, , \tag{1.60}$$

where V is the velocity potential.

The energy density and pressure are also perturbed and we write:

$$\rho = \bar{\rho} + \delta\rho \, , \qquad p = \bar{p} + \delta p \, , \tag{1.61}$$

so that, using (1.17), we can calculate the components of the perturbed energy-momentum tensor $T_{\mu\nu}$:
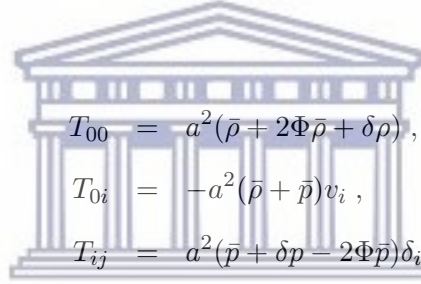
$$T_{00} = a^2(\bar{\rho} + 2\Phi\bar{\rho} + \delta\rho) \, , \tag{1.62}$$

$$T_{0i} = -a^2(\bar{\rho} + \bar{p})v_i \, , \tag{1.63}$$

$$T_{ij} = a^2(\bar{p} + \delta p - 2\Phi\bar{p})\delta_{ij} \, . \tag{1.64}$$

We then substitute the expressions for the Ricci tensor, Ricci scalar, 4-velocity and the energy-momentum tensor into the Einstein field equation (1.19), the components of which yield the following equations in the perturbations:

$$\nabla^2\Phi - 3\mathcal{H}(\Phi' + \mathcal{H}\Phi) = 4\pi Ga^2\delta\rho \, , \tag{1.65}$$

$$\Phi' + \mathcal{H}\Phi = -4\pi Ga^2(\bar{\rho} + \bar{p})V \, , \tag{1.66}$$

$$\Phi'' + 2\mathcal{H}\Phi' + (\mathcal{H} + 2\mathcal{H}' + \mathcal{H}^2)\Phi = 4\pi Ga^2\delta p \, . \tag{1.67}$$

1.5.2.2   Perturbed conservation equations

To derive the conservation equations in the perturbed case, we follow a similar procedure to the background case in Section 1.5. The energy-momentum conservation equation is, as before, given by

$$\nabla_\mu T^\mu_{\ \nu} = \partial_\mu T^\mu_{\ \nu} + \Gamma^\mu_{\ \mu\alpha}T^\alpha_{\ \nu} - \Gamma^\beta_{\ \mu\nu}T^\mu_{\ \beta} = 0 \, , \tag{1.68}$$

where we must once again raise one index of the energy-momentum tensor. In this case, the perturbed metric (1.52) must be used for this, in order that all the first-order terms in the components of the energy-momentum tensor (1.62) - (1.64) are captured. Thus, the non-zero components of $T^\mu_{\ \nu}$ are:

$$T^0_{\ 0} = -(\bar{\rho} + \delta\rho) \ , \qquad T^0_{\ i} = (\bar{\rho} + \bar{p})\partial_i V \ , \qquad T^i_{\ j} = (\bar{p} + \delta p)\delta^i_{\ j} \ . \qquad (1.69)$$

We substitute (1.69) into (1.68) and contract the equation as before. The background variables are removed using the background conservation equations, changing to conformal time where necessary. The perturbed version of the **Continuity equation** is given by

$$\delta\rho' + 3\mathcal{H}(\delta\rho + \delta p) = (\bar{\rho} + \bar{p})\left[3\Phi' - \nabla^2 V\right] \ , \qquad (1.70)$$

where V is the velocity potential and the Laplacian is defined as $\nabla^2 = \partial_i\partial^i$. This equation is similar to the one in the background case, but now the potential Φ and peculiar velocity on the right-hand side act as source terms for the perturbations in energy density and pressure. The perturbed **Euler equation** is given by

$$\left[(\bar{\rho} + \bar{p})V\right]' + 4\mathcal{H}(\bar{\rho} + \bar{p})V = -[\delta p + (\bar{\rho} + \bar{p})\Phi] \ , \qquad (1.71)$$

or, in terms of the peculiar velocity, by

$$\left[(\bar{\rho} + \bar{p})v_i\right]' + 4\mathcal{H}(\bar{\rho} + \bar{p})v_i = -[\partial_i(\delta p) + (\bar{\rho} + \bar{p})\partial_i\Phi] \ , \qquad (1.72)$$

which is an evolution equation for the peculiar velocity, dependent on the potential Φ and the perturbations in pressure.

Next, we define the density contrast in Poisson gauge:

$$\delta = \frac{\delta\rho}{\bar{\rho}} \ . \ , \qquad (1.73)$$

as well as the sound speed c_s for adiabatic pressure perturbations [34, 35]:

$$c_s^2 = \frac{\delta p}{\delta\rho} = \frac{\bar{p}'}{\bar{\rho}'} \ . \qquad (1.74)$$

Using the definitions of the EoS parameter, the density contrast and the sound speed (see (1.23), (1.73) and (1.74) respectively) we can rewrite the set of perturbation equations to yield:

$$\nabla^2\Phi - 3\mathcal{H}(\Phi' + \mathcal{H}\Phi) = 4\pi G a^2 \bar{\rho}\delta \, , \tag{1.75}$$

$$\Phi' + \mathcal{H}\Phi = -4\pi G a^2 \bar{\rho}(1+w)V \, , \tag{1.76}$$

$$\Phi'' + 3\mathcal{H}\Phi' + (2\mathcal{H}' + \mathcal{H}^2)\Phi = 4\pi G a^2 c_s^2 \bar{\rho}\delta \, , \tag{1.77}$$

and similarly for the perturbed conservation equations:

$$\delta' + 3\mathcal{H}(c_s^2 - w)\delta = (1+w)\big[3\Phi' - \nabla^2 V\big] \, , \tag{1.78}$$

$$\big[\bar{\rho}(1+w)V\big]' + c_s^2\bar{\rho}\delta = -\bar{\rho}(1+w)\big[\Phi + 4\mathcal{H}V\big] \, . \tag{1.79}$$

The equation (1.75) relates the density contrast δ to the potential Φ in a similar way to the Poisson equation in Newtonian mechanics. We may use this to rewrite (1.77) in terms of only the potential Φ:

$$\Phi'' + 3(1 + c_s^2)\mathcal{H}\Phi' + \big[2\mathcal{H}' + (1 + 3c_s^2)\mathcal{H}^2\big]\Phi = c_s^2\nabla^2\Phi \, , \tag{1.80}$$

Neglecting radiation, the Friedmann and Raychaudhuri equations, from (1.54) and (1.55) respectively, read:

$$\mathcal{H}^2 = \frac{8\pi G}{3}\bar{\rho} + \frac{a^2\Lambda}{3} \, , \tag{1.81}$$

$$\mathcal{H}' = -\frac{4\pi G}{3}\bar{\rho} + \frac{a^2\Lambda}{3} \, , \tag{1.82}$$

which gives

$$\mathcal{H}' = -\frac{1}{2}\mathcal{H}^2 + \frac{a^2\Lambda}{2} \, . \tag{1.83}$$

Using this result in (1.80) yields

$$\Phi'' + 3(1 + c_s^2)\mathcal{H}\Phi' + 3c_s^2\mathcal{H}^2\Phi + a^2\Lambda\Phi = c_s^2\nabla^2\Phi \, . \tag{1.84}$$

This equation describes the evolution of the Bardeen potential Φ and is known as the Bardeen equation.

1.5.2.3 Growth of structure in a ΛCDM universe

We focus here on observations of the Universe at relatively low redshift, so in the following we restrict our description to the Universe at late times, when the dominant contributions to the energy are from dark matter and dark energy, and the contribution from radiation has become negligible (see Figure 1.3). Thus, we may neglect the radiation component: $\bar{\rho}_r = 0$, $\delta\rho_r = 0$. On scales where linear perturbations are accurate, the baryonic matter is cold and shares the same velocity as CDM: $V_b = V_c = V$. We also take $\delta\rho_\Lambda = 0$, since the cosmological constant is not perturbed.

Thus, on linear scales, the perturbations reduce to perturbations in cold matter only and hereafter we use δ without subscript to refer to the *matter* density contrast in Poisson gauge:

$$\delta = \frac{\delta\rho_m}{\bar{\rho}_m} \ . \tag{1.85}$$

The "cold" matter particles of the ΛCDM model are non-interacting and do not exert or experience pressure. Thus we have, for matter: $w_m = 0$, $\bar{p}_m = 0$, $\delta p_m = 0$ and, using (1.74), $c_s = 0$. Substituting these results into (1.75) - (1.79) yields:

$$\nabla^2\Phi - 3\mathcal{H}(\Phi' + \mathcal{H}\Phi) = 4\pi G a^2 \bar{\rho}_m \delta \ , \tag{1.86}$$

$$\Phi' + \mathcal{H}\Phi = -4\pi G a^2 \bar{\rho}_m V \ , \tag{1.87}$$

$$\Phi'' + 3\mathcal{H}\Phi' + a^2\Lambda\Phi = 0 \ , \tag{1.88}$$

$$\delta' = 3\Phi' - \nabla^2 V \ , \tag{1.89}$$

$$V' = -\Phi - \mathcal{H}V \ , \tag{1.90}$$

where we have also used (1.84) to obtain (1.88).

Using (1.87) and the definition of Ω_m (1.30), we can rewrite (1.86) as

$$\nabla^2\Phi = \frac{3}{2}\Omega_m\mathcal{H}^2\big[\delta - 3\mathcal{H}V\big] = \frac{3}{2}\Omega_m\mathcal{H}^2\delta_{\mathrm{C}} \ . \tag{1.91}$$

As will be shown in Chapter 3, the term in the square brackets is in fact the comoving matter density contrast δ_{C} and so we recognize in (1.91) the form of the **Poisson equation**.

We now wish to determine the evolution of Φ using (1.88). Recall the definition of the dimensionless density parameter for Λ:

$$\Omega_\Lambda = \frac{\Lambda a^2}{3\mathcal{H}^2} = 1 - \Omega_m \tag{1.92}$$

where the second equality follows from (1.41) at late times. Together with (1.83), this yields

$$\mathcal{H}' = \left(1 - \frac{3}{2}\Omega_m\right)\mathcal{H}^2 . \tag{1.93}$$

We can also rewrite the conformal time derivatives in terms of derivatives with respect to the scale factor:

$$\frac{\mathrm{d}}{\mathrm{d}\eta} = a\mathcal{H}\frac{\mathrm{d}}{\mathrm{d}a} , \qquad \frac{\mathrm{d}^2}{\mathrm{d}\eta^2} = a^2\mathcal{H}^2\frac{\mathrm{d}^2}{\mathrm{d}a^2} + a\mathcal{H}^2\left(1 + \frac{\mathcal{H}'}{\mathcal{H}^2}\right)\frac{\mathrm{d}}{\mathrm{d}a} . \tag{1.94}$$

Using (1.92) - (1.94) we may rewrite the Bardeen equation (1.88) as

$$a^2\frac{\mathrm{d}^2\Phi}{\mathrm{d}a^2} + a\left(5 - \frac{3}{2}\Omega_m\right)\frac{\mathrm{d}\Phi}{\mathrm{d}a} + 3(1 - \Omega_m)\Phi = 0 . \tag{1.95}$$

To describe the time evolution of the perturbative potential Φ, we define the linear growth function $D(z)$ as [42, 43]

$$\frac{D}{a} = \frac{\Phi}{\Phi_\mathrm{d}}, \tag{1.96}$$

which is normalized to $D_d = a_d$ at the time of the decoupling between matter and radiation ($a_\mathrm{d} \sim 10^{-3}$). In Fourier space, the Poisson equation is

$$-k^2\Phi = \frac{3}{2}\Omega_m\mathcal{H}^2\delta_\mathrm{C} = \frac{3}{2}\Omega_{m0}H_0^2\frac{\delta_\mathrm{C}}{a} . \tag{1.97}$$

Hence, we may re-write the potentials in terms of the density contrast, and the linear growth factor becomes

$$D = a_\mathrm{d}\frac{\delta_\mathrm{C}}{\delta_\mathrm{Cd}} , \tag{1.98}$$

which describes the growth in the amplitude of the density perturbations above the background, normalized to the matter-dominated era.

In terms of the growth factor, the Bardeen equation (1.94) becomes

$$\frac{\mathrm{d}^2D}{\mathrm{d}a^2} + \frac{3}{a}\left(1 - \frac{\Omega_m}{2}\right)\frac{\mathrm{d}D}{\mathrm{d}a} - \frac{3}{2a^2}\Omega_m D = 0 , \tag{1.99}$$

which can be solved numerically, using as the initial condition a matter-dominated universe (see Figure 1.5).
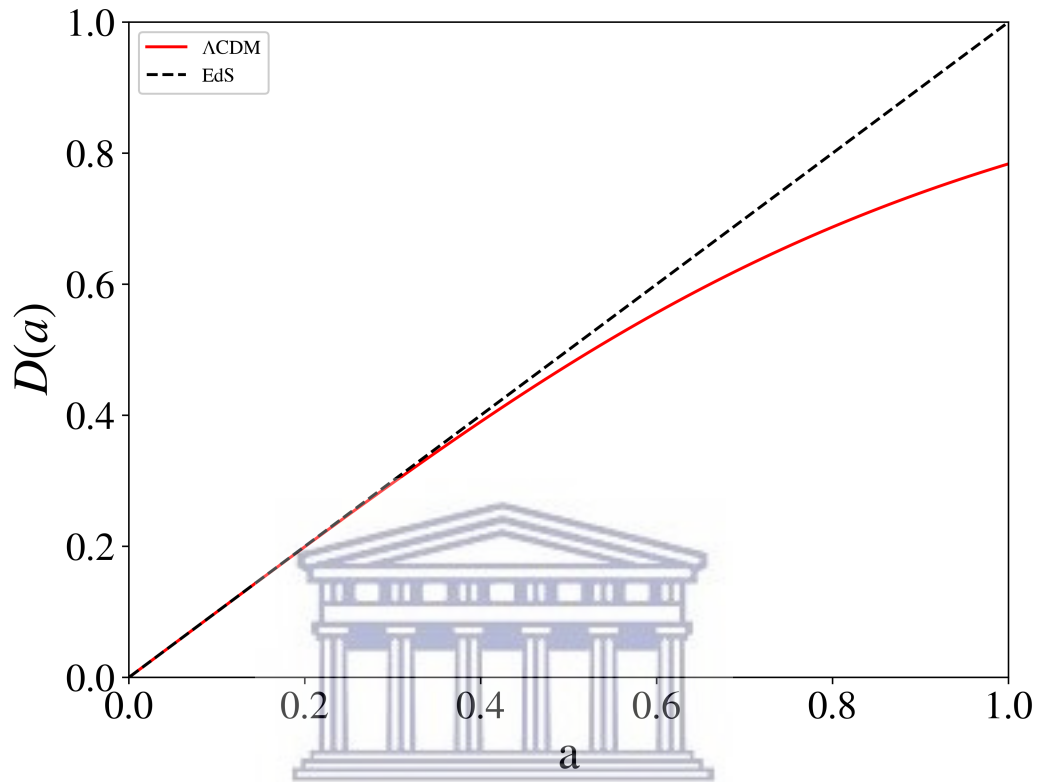
FIGURE 1.5: The evolution of the matter growth factor as a function of the scale factor for an EdS universe (dashed black) and a ΛCDM universe (solid red). The addition of a cosmological constant Λ to the EdS model results in a slower growth rate in the ΛCDM model at late times, when the scale factor approaches its present value.

In the case of an Einstein-de Sitter (EdS) Universe containing matter only ($\Omega_m = 1$ and $\Omega_r = \Omega_\Lambda = 0$), (1.99) reduces to a second order Cauchy-Euler equation and the solution may be found analytically to show that the growth factor evolves with the scale factor as

$$D^{(\text{EdS})}(a) = a \ , \tag{1.100}$$

and hence

$$\frac{\mathrm{d}D^{(\text{EdS})}}{\mathrm{d}a} = 1 \ . \tag{1.101}$$

Therefore, from (1.98), the gravitational potential Φ is constant in time: $\Phi = \Phi_{\mathrm{d}}$, and the EdS results (1.100) and (1.101) are suitable matter-dominant initial conditions.

The numerical result including the cosmological constant is shown in Figure 1.5. At later times we see that the growth of structure in a ΛCDM Universe is suppressed with respect to the EdS Universe, since it contains dark energy which works against the gravitational collapse of density perturbations.

It is useful to define the linear growth rate, f [1, 36]:

$$f = \frac{\mathrm{d}\ln D}{\mathrm{d}\ln a} = \frac{\mathrm{d}\ln\delta_{\mathrm{C}}}{\mathrm{d}\ln a} \; , \tag{1.102}$$

where the second equality follows from the proportionality between the growth and the comoving density contrast (1.98).

With this definition, the evolution equation (1.99) becomes a first-order equation for f:

$$a\frac{\mathrm{d}f}{\mathrm{d}a} + f^2 + \frac{1}{2}\left(4 - 3\Omega_m\right)f - \frac{3}{2}\Omega_m = 0 \; , \tag{1.103}$$

where we have used

$$\frac{\mathrm{d}f}{\mathrm{d}a} = \frac{f}{a} + \frac{a}{D}\frac{\mathrm{d}^2 D}{\mathrm{d}a^2} - \frac{f^2}{a} \; . \tag{1.104}$$

Once again we can also consider the EdS Universe and from the growth function solution (1.100), using the definition of the growth rate (1.102), we obtain

$$f^{(\mathrm{EdS})} = 1 \; . \tag{1.105}$$

There is an analytical approximation in the ΛCDM case, which can be parametrized by [36, 37, 41]

$$f(a) = \left[\Omega_m(a)\right]^{\gamma} \; , \tag{1.106}$$

as shown in Figure 1.6, where γ is called the growth index and fits the numerical solution of (1.103) well at a value $\gamma \sim 0.55$ [37, 38].
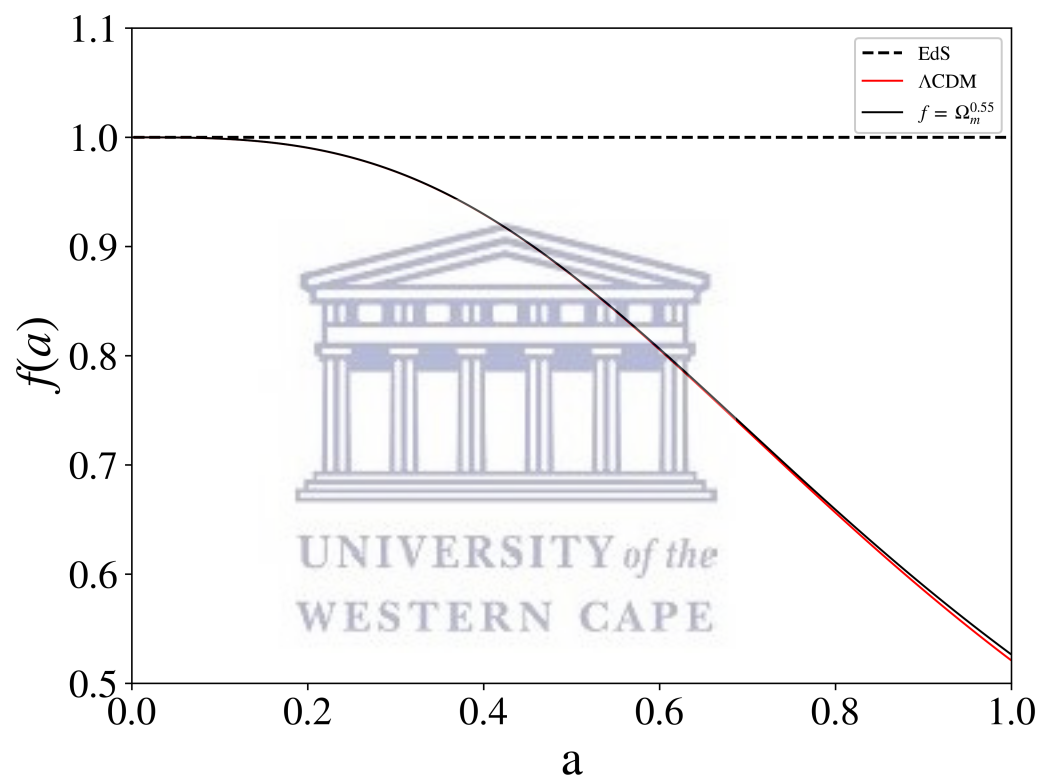
FIGURE 1.6: The evolution of the linear growth rate for an EdS Universe (dashed black) and a ΛCDM Universe (solid red). The parametrization with $\gamma = 0.55$ is shown in solid black. The addition of a cosmological constant Λ to the EdS model decreases the growth rate as a approaches its present-day value: $a_0 = 1$.

Chapter 2

Angular Power Spectra

So far we have discussed the nature of the Universe in which we live and built up the framework of the ΛCDM model which describes it. We now turn to explaining the framework with which we can treat observations of the Universe. In this chapter we present the theoretical derivations of expressions for the angular power spectra of galaxy number counts, HI intensity mapping and CMB lensing. We begin by defining the two-point correlation function in general and relating this to the angular power spectrum on a 2D spherical shell. Following this, we relate the angular power spectrum to the power spectrum of primordial curvature fluctuations, before finally describing the calculation which allows us to take account of an observational window function.

2.1 Two-point correlation function

Recall that the matter density contrast is defined in the Poisson gauge at a particular position $\boldsymbol{x}$ as

$$\delta(\boldsymbol{n}, z) = \delta(\boldsymbol{x}, \eta) = \frac{\rho(\boldsymbol{x}, \eta) - \bar{\rho}(\bar{\eta})}{\bar{\rho}(\bar{\eta})} \ , \tag{2.1}$$

where $\boldsymbol{n}$ is the observation direction, z is the redshift corresponding to the position and $\bar{\rho}$ is the background density of matter. The density field $\delta(\boldsymbol{x}, \eta)$ is a Gaussian random field which satisfies the following statistical properties:

$$0 = \langle \delta(\boldsymbol{x}) \rangle \ , \tag{2.2}$$

$$\xi_m(r) = \langle \delta(\boldsymbol{x}) \delta(\boldsymbol{x'}) \rangle \ , \tag{2.3}$$

30

where we have suppressed the dependence on conformal time for brevity and $\boldsymbol{r}$ is the displacement between the points $\boldsymbol{x}$ and $\boldsymbol{x}'$: $r = |\boldsymbol{x}' - \boldsymbol{x}|$ (see Fig. 2.1).

The statistical properties above mean that δ is zero on average and that its two-point correlation function $\xi_m(\boldsymbol{x}, \boldsymbol{x}')$ actually only depends on the distance r between the two points. This is a consequence of assuming statistical isotropy and homogeneity (since ξ_m is independent of $\boldsymbol{x}'$) in the density field of the Universe.

The ensemble average $\langle X \rangle$ of a variable X has some subtlety in its definition and bears discussion in more detail. The ensemble average is defined as the average value of a random variable, taken over many realizations of its associated random functions. In a cosmological context this is like measuring the average value from an ensemble of universe realisations. However, it is only possible for us to observe one realization of our Universe. This places a fundamental limit, known as cosmic variance, on the accuracy of our measurements and prevents us from directly measuring the ensemble average. Instead, we must rely on a kind of ergodic hypothesis, where we measure the spatially-averaged values as a substitute for the ensemble average [2].

2.1.1 Relationship to the power spectrum

Throughout this work we make use of the Fourier transform defined according to the following convention:

$$\delta_{\boldsymbol{k}}(\eta) = \int \mathrm{d}^3x \; \delta(\boldsymbol{x}, \eta) \; e^{-i\boldsymbol{k}\cdot\boldsymbol{x}}, \tag{2.4}$$

$$\delta(\boldsymbol{x}, \eta) = \frac{1}{(2\pi)^3} \int \mathrm{d}^3k \; \delta_{\boldsymbol{k}}(\eta) \; e^{i\boldsymbol{k}\cdot\boldsymbol{x}}. \tag{2.5}$$

We now consider the two-point correlation function of δ in Fourier space. Dropping the η dependence for brevity, we can use (2.4) and the statistical properties (2.2), (2.3) to

show that:

$$
\begin{aligned}
\langle \delta_{\boldsymbol{k}}\,\delta_{\boldsymbol{k}'}\rangle &= \int \mathrm{d}^3 x'\,\mathrm{d}^3 x\,\langle \delta(\boldsymbol{x})\delta\left(\boldsymbol{x}'\right)\rangle\,e^{-i\boldsymbol{k}\cdot\boldsymbol{x}}\,e^{-i\boldsymbol{k}'\cdot\boldsymbol{x}'} \\
&= \int \mathrm{d}^3 x'\,\mathrm{d}^3 r\,\xi_m(r)\,e^{-i\boldsymbol{k}\cdot\boldsymbol{x}}\,e^{-i\boldsymbol{k}'\cdot\boldsymbol{x}'}(e^{i\boldsymbol{k}\cdot\boldsymbol{x}'}e^{-i\boldsymbol{k}\cdot\boldsymbol{x}'}) \\
&= \int \mathrm{d}^3 x'\,\mathrm{d}^3 r\,\xi_m(r)e^{-i(\boldsymbol{k}+\boldsymbol{k}')\cdot\boldsymbol{x}'}\,e^{i\boldsymbol{k}\cdot(\boldsymbol{x}'-\boldsymbol{x})} \\
&= \int \mathrm{d}^3 x'\,e^{-i(\boldsymbol{k}+\boldsymbol{k}')\cdot\boldsymbol{x}'}\int \mathrm{d}^3 r\,\xi_m(r)e^{-i\boldsymbol{k}\cdot\boldsymbol{r}} \\
&= (2\pi)^3 \delta_D(\boldsymbol{k}+\boldsymbol{k}')\int \mathrm{d}^3 r\,\xi_m(r)e^{-i\boldsymbol{k}\cdot\boldsymbol{r}}\,,
\end{aligned}
\tag{2.6}
$$

where the definition of $\boldsymbol{r}$ at constant $\boldsymbol{x}'$ has been used to change the integration variable in the second line. The subscript m indicates that ξ_m is the two-point correlation function of matter fluctuations. The above expression can be rewritten as

$$
\langle \delta_{\boldsymbol{k}}(\eta)\,\delta_{\boldsymbol{k}'}(\eta)\rangle \equiv (2\pi)^3 \delta_D(\boldsymbol{k}+\boldsymbol{k}')P_m(k,\eta)\,,
\tag{2.7}
$$

where we define the 3D matter power spectrum $P_m(k,\eta)$ of the matter density fluctuations δ as[1]

$$
P_m(k,\eta) = \int \mathrm{d}^3 r\,\xi_m(r,\eta)e^{-i\boldsymbol{k}\cdot\boldsymbol{r}}\,,
\tag{2.8}
$$

which means that the power spectrum and two-point correlation function are related via Fourier transform. Once again, statistical isotropy is evident in the fact that the power spectrum depends only on the modulus of $\boldsymbol{k}$. The Dirac delta $\delta_D(\boldsymbol{k}+\boldsymbol{k}')$ in (2.7) implies that only modes with wave vector $\boldsymbol{k}$ of the same length, but of opposite direction will be correlated, and is a result of statistical homogeneity. This expression can be further simplified if we choose our coordinate system so that the spatial axis from which θ is measured is aligned with $\boldsymbol{k}$, which gives $\boldsymbol{k}\cdot\boldsymbol{r} = kr\cos\theta$ and thus

$$
\begin{aligned}
P_m(k) &= \int r^2 \mathrm{d}r\,\sin\theta\,\mathrm{d}\theta\,\mathrm{d}\phi\,\xi_m(r)e^{-ikr\cos\theta} \\
&= 4\pi \int r^2 \mathrm{d}r\,\xi_m(r)j_0(kr)\,.
\end{aligned}
\tag{2.9}
$$

---

[1]Hereafter we suppress the conformal time dependence of $\delta_{\boldsymbol{k}}$ and P_m for brevity.

where $j_0(kr)$ is the zeroth order spherical Bessel function. Similarly, using the inverse Fourier transform, we find that

$$\xi_m(r) \;=\; \frac{1}{2\pi^2}\int k^2 \mathrm{d}k \; P_m(k)j_0(kr)\,. \tag{2.10}$$

For some of the derivations that follow, it is useful to examine the quantity $\langle \delta_{\boldsymbol{k}}\,\delta^*_{\boldsymbol{k}'}\rangle$ and its relation to the power spectrum. In a similar way to before, we can show that

$$\langle \delta_{\boldsymbol{k}}\,\delta^*_{\boldsymbol{k}'}\rangle \;=\; (2\pi)^3\delta_D(\boldsymbol{k}-\boldsymbol{k}')\int \mathrm{d}^3 r \;\xi_m(r)e^{-i\boldsymbol{k}\cdot\boldsymbol{r}}\,. \tag{2.11}$$

Hence, using (2.8), the above expression can be rewritten as

$$\langle \delta_{\boldsymbol{k}}\,\delta^*_{\boldsymbol{k}'}\rangle \equiv (2\pi)^3\delta_D(\boldsymbol{k}-\boldsymbol{k}')P_m(k)\,. \tag{2.12}$$

2.1.2 Expansion in Legendre multipoles

We may also consider the power spectrum of galaxies, related to the galaxy number density contrast, defined analogously to the matter density contrast:

$$\delta_g(\boldsymbol{x}) = \delta_g(\boldsymbol{n},z) = \frac{\rho_g(\boldsymbol{n},z)-\bar{\rho}_g(\bar{z})}{\bar{\rho}_g(\bar{z})}\,, \tag{2.13}$$

with the associated correlation function defined as

$$\xi_g(r) = \langle \delta_g(\boldsymbol{x})\delta_g(\boldsymbol{x}')\rangle\,. \tag{2.14}$$

There is a dependence on the direction $\boldsymbol{n}$, which is the unit vector along the line of sight in the direction of observation. In reality, the correlation function is associated with pairs of galaxies and thus pairs of directions, one for each galaxy. However, under the flat-sky approximation we assume that correlated galaxies are sufficiently far away that they have similar redshifts z and approximately the same direction of observation $\boldsymbol{n}$ [39, 40]. The directional dependence enters into the anisotropic galaxy power spectrum which can hence be decomposed in Legendre polynomials $\mathcal{L}(\mu)$ [39, 40]:

$$P_g(k,\hat{\boldsymbol{k}}\cdot\boldsymbol{n}) = \sum_{\ell=0}^{\infty} P_g^\ell(k)\mathcal{L}_\ell(\hat{\boldsymbol{k}}\cdot\boldsymbol{n})\,, \tag{2.15}$$

where $\hat{\boldsymbol{k}} \cdot \boldsymbol{n}$ is the cosine of the angle between the line of sight $\boldsymbol{n}$ and wavenumber $\boldsymbol{k}$. The coefficients P_g^ℓ can be determined from the power spectrum using the orthogonality of the Legendre polynomials (A.3). Multiplying (2.15) by $\mathcal{L}_{\ell'}$ and integrating, we obtain

$$
\begin{aligned}
\int_{-1}^{1} \mathrm{d}(\hat{\boldsymbol{k}} \cdot \boldsymbol{n}) \ P_g(k, \hat{\boldsymbol{k}} \cdot \boldsymbol{n}) \mathcal{L}_{\ell'}(\hat{\boldsymbol{k}} \cdot \boldsymbol{n}) &= \int_{-1}^{1} \mathrm{d}(\hat{\boldsymbol{k}} \cdot \boldsymbol{n}) \sum_{\ell=0}^{\infty} P_g^\ell(k) \mathcal{L}_\ell(\hat{\boldsymbol{k}} \cdot \boldsymbol{n}) \mathcal{L}_{\ell'}(\hat{\boldsymbol{k}} \cdot \boldsymbol{n}) \\
&= \sum_{\ell=0}^{\infty} P_g^\ell(k) \frac{2}{2\ell+1} \delta_{\ell\ell'} \\
&= \frac{2}{2\ell'+1} P_g^{\ell'}(k) \, .
\end{aligned}
\tag{2.16}
$$

Re-labelling indices, we obtain

$$
P_g^\ell(k) = \left(\ell + \frac{1}{2}\right) \int_{-1}^{1} \mathrm{d}(\hat{\boldsymbol{k}} \cdot \boldsymbol{n}) \ P_g(k, \hat{\boldsymbol{k}} \cdot \boldsymbol{n}) \mathcal{L}_\ell(\hat{\boldsymbol{k}} \cdot \boldsymbol{n}) \, .
\tag{2.17}
$$

In a similar way, we can expand the two-point correlation function for galaxies in the flat-sky approximation in Legendre polynomials [39, 40]:

$$
\xi_g(r, \hat{\boldsymbol{r}} \cdot \boldsymbol{n}) = \sum_{\ell=0}^{\infty} \xi_g^\ell(r) \mathcal{L}_\ell(\hat{\boldsymbol{r}} \cdot \boldsymbol{n}) \, ,
\tag{2.18}
$$

where

$$
\xi_g^\ell(r) = \left(\ell + \frac{1}{2}\right) \int_{-1}^{1} \mathrm{d}(\hat{\boldsymbol{r}} \cdot \boldsymbol{n}) \ \xi_g(r, \hat{\boldsymbol{r}} \cdot \boldsymbol{n}) \mathcal{L}_\ell(\hat{\boldsymbol{r}} \cdot \boldsymbol{n}) \, .
\tag{2.19}
$$

This expression can also be written in terms of the coefficients P_g^ℓ, using the inverse Fourier transform of $\xi_g(r, \hat{\boldsymbol{r}} \cdot \boldsymbol{n})$ [39, 40]:

$$
\begin{aligned}
\xi_g^\ell(r) &= \left(\ell + \frac{1}{2}\right) \int_{-1}^{1} \mathrm{d}(\hat{\boldsymbol{r}} \cdot \boldsymbol{n}) \left(\int \frac{\mathrm{d}^3 k}{(2\pi)^3} \ P_g(k, \hat{\boldsymbol{k}} \cdot \boldsymbol{n}) e^{i\boldsymbol{k} \cdot \boldsymbol{r}}\right) \mathcal{L}_\ell(\hat{\boldsymbol{r}} \cdot \boldsymbol{n}) \\
&= \frac{2\ell+1}{2(2\pi)^3} \int \mathrm{d}^3 k \sum_{\ell'=0}^{\infty} P_g^{\ell'}(k) \int_{-1}^{1} \mathrm{d}(\hat{\boldsymbol{r}} \cdot \boldsymbol{n}) \ \mathcal{L}_{\ell'}(\hat{\boldsymbol{k}} \cdot \boldsymbol{n}) \ \mathcal{L}_\ell(\hat{\boldsymbol{r}} \cdot \boldsymbol{n}) \\
&\quad \times \left(\sum_{\ell''=0}^{\infty} (2\ell''+1) i^{\ell''} \mathcal{L}_{\ell''}(\hat{\boldsymbol{k}} \cdot \hat{\boldsymbol{r}}) \ j_{\ell''}(kr)\right) \\
&= \frac{2\ell+1}{2(2\pi)^3} \int k^2 \mathrm{d}k \sum_{\ell'=0}^{\infty} \sum_{\ell''=0}^{\infty} (2\ell''+1) i^{\ell''} j_{\ell''}(kr) \ P_g^{\ell'}(k) \\
&\quad \times \int_{-1}^{1} \mathrm{d}(\hat{\boldsymbol{r}} \cdot \boldsymbol{n}) \ \mathcal{L}_\ell(\hat{\boldsymbol{r}} \cdot \boldsymbol{n}) \int \mathrm{d}\Omega_{\hat{\boldsymbol{k}}} \ \mathcal{L}_{\ell'}(\hat{\boldsymbol{k}} \cdot \boldsymbol{n}) \mathcal{L}_{\ell''}(\hat{\boldsymbol{k}} \cdot \hat{\boldsymbol{r}}) \, ,
\end{aligned}
\tag{2.20}
$$

where the exponential term is rewritten using a plane wave expansion (A.6) in the second line and the integral over k is split as $\mathrm{d}^3 k = k^2 \mathrm{d}k \mathrm{d}\Omega_{\boldsymbol{k}}$.

The integral over $\mathrm{d}\Omega_{\hat{\boldsymbol{k}}}$ in (2.20) may be rewritten by expanding the Legendre polynomials in spherical harmonics (A.4) to yield

$$
\begin{aligned}
\int \mathrm{d}\Omega_{\hat{\boldsymbol{k}}} \mathcal{L}_{\ell'}(\hat{\boldsymbol{k}} \cdot \boldsymbol{n}) \, \mathcal{L}_{\ell''}(\hat{\boldsymbol{k}} \cdot \hat{\boldsymbol{r}}) \; &= \; \int \mathrm{d}\Omega_{\hat{\boldsymbol{k}}} \left(\frac{4\pi}{2\ell'+1} \sum_{m'=-\ell'}^{\ell'} Y_{\ell'm'}(\boldsymbol{n}) Y_{\ell'm'}^{*}(\hat{\boldsymbol{k}}) \right) \\
&\qquad \times \left(\frac{4\pi}{2\ell''+1} \sum_{m''=-\ell''}^{\ell''} Y_{\ell''m''}(\hat{\boldsymbol{k}}) Y_{\ell''m''}^{*}(\hat{\boldsymbol{r}}) \right) \\
&= \; \frac{(4\pi)^2}{(2\ell'+1)(2\ell''+1)} \sum_{m'=-\ell'}^{\ell'} \sum_{m''=-\ell''}^{\ell''} Y_{\ell'm'}(\boldsymbol{n}) Y_{\ell''m''}^{*}(\hat{\boldsymbol{r}}) \\
&\qquad \times \int \mathrm{d}\Omega_{\hat{\boldsymbol{k}}} Y_{\ell''m''}(\hat{\boldsymbol{k}}) Y_{\ell'm'}^{*}(\hat{\boldsymbol{k}}) \\
&= \; \frac{(4\pi)^2}{(2\ell'+1)(2\ell''+1)} \sum_{m'=-\ell'}^{\ell'} Y_{\ell'm'}(\boldsymbol{n}) Y_{\ell''m'}^{*}(\hat{\boldsymbol{r}}) \delta_{\ell'\ell''} \,, \quad (2.21)
\end{aligned}
$$

where the elimination of the inner sum in the third line uses the orthonormality of the spherical harmonics (A.5). Thus, substituting (2.21) back into (2.20) and taking the sum over ℓ'', we can use the fact that the sum over the spherical harmonics is simply an expansion of a Legendre polynomial (A.4):

$$
\sum_{m'=-\ell'}^{\ell'} Y_{\ell'm'}(\boldsymbol{n}) Y_{\ell'm'}^{*}(\hat{\boldsymbol{r}}) = \frac{2\ell'+1}{4\pi} \mathcal{L}_{\ell'}(\hat{\boldsymbol{r}} \cdot \boldsymbol{n}) \qquad (2.22)
$$

Thus the expression for ξ_g^ℓ becomes

$$
\begin{aligned}
\xi_g^\ell(r) \; &= \; \frac{2\ell+1}{4\pi^2} \int k^2 \mathrm{d}k \sum_{\ell'=0}^{\infty} i^{\ell'} j_{\ell'}(kr) \, P_g^{\ell'}(k) \int_{-1}^{1} \mathrm{d}(\hat{\boldsymbol{r}} \cdot \boldsymbol{n}) \, \mathcal{L}_\ell(\hat{\boldsymbol{r}} \cdot \boldsymbol{n}) \mathcal{L}_{\ell'}(\hat{\boldsymbol{r}} \cdot \boldsymbol{n}) \\
&= \; \frac{2\ell+1}{4\pi^2} \int k^2 \mathrm{d}k \sum_{\ell'=0}^{\infty} i^{\ell'} j_{\ell'}(kr) \, P_g^{\ell'}(k) \frac{2}{2\ell+1} \delta_{\ell\ell'} \\
&= \; \int \frac{k^2 \mathrm{d}k}{2\pi^2} \, i^\ell \, j_\ell(kr) \, P_g^\ell(k) \,, \qquad (2.23)
\end{aligned}
$$

where (A.3) is used in the second line.

2.1.3 Projection onto a 2D spherical shell

Actual observations are made on a spherical shell of radius $\chi(z)$, centered at our position. Thus, each point we observe in the sky has a position described by $\boldsymbol{x}(\boldsymbol{n}, z) = \chi(z)\boldsymbol{n}$, where $\boldsymbol{n}$ is the unit vector along the line from the centre of the shell to the point under
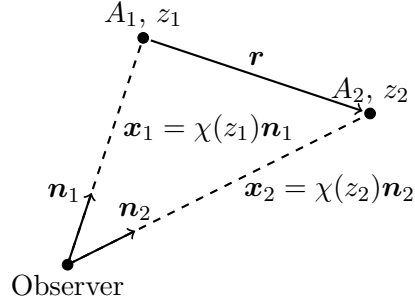
FIGURE 2.1: This figure is a geometrical representation of the arguments found in (2.42), with respect to the observer and two arbitrary galaxies A_1 and A_2 at redshifts z_1 and z_2 and in observed directions $\boldsymbol{n}_1$ and $\boldsymbol{n}_2$, respectively.

consideration on the shell: (θ, ϕ). The galaxy number density contrast may then be decomposed into spherical harmonics on the shell:

$$\delta_g(\boldsymbol{x}) = \delta_g(\boldsymbol{n}, z) = \sum_{\ell=0}^{\infty} \sum_{m=-\ell}^{\ell} a_{\ell m}(\chi(z)) Y_{\ell m}(\boldsymbol{n}) \, . \tag{2.24}$$

Note that only the projection coefficients $a_{\ell m}$ are dependent on the distance (redshift). In the following derivations this dependence is suppressed for convenience. The coefficients $a_{\ell m}$ may be related back to the original function using the orthonormality of the spherical harmonic functions (A.5). Multiplying (2.24) by the complex conjugate $Y_{\ell' m'}^*(\boldsymbol{n})$ and integrating over solid angles, we obtain

$$
\begin{aligned}
\int \mathrm{d}\Omega_{\boldsymbol{n}} \, \delta_g(\boldsymbol{n}, z) Y_{\ell' m'}^*(\boldsymbol{n}) &= \int \mathrm{d}\Omega_{\boldsymbol{n}} \sum_{\ell=0}^{\infty} \sum_{m=-\ell}^{\ell} a_{\ell m}(\chi(z)) Y_{\ell m}(\boldsymbol{n}) Y_{\ell' m'}^*(\boldsymbol{n}) \\
&= \sum_{\ell=0}^{\infty} \sum_{m=-\ell}^{\ell} a_{\ell m} \int \mathrm{d}\Omega_{\boldsymbol{n}} \, Y_{\ell m}(\boldsymbol{n}) Y_{\ell' m'}^*(\boldsymbol{n}) \\
&= a_{\ell' m'} \, .
\end{aligned}
\tag{2.25}
$$

Re-labelling indices, we obtain

$$a_{\ell m}(z) = \int \mathrm{d}\Omega_{\boldsymbol{n}} \, \delta_g(\boldsymbol{n}, z) Y_{\ell m}^*(\boldsymbol{n}) \, . \tag{2.26}$$

The above equation relates the coefficients $a_{\ell m}$ to the real-space δ_g, but it is also possible to rewrite these coefficients in terms of their Fourier modes, using the inverse Fourier transform:

$$a_{\ell m} = \frac{1}{(2\pi)^3} \int \mathrm{d}\Omega_{\boldsymbol{n}} \, \mathrm{d}^3 k \, \delta_{g\boldsymbol{k}} \, Y_{\ell m}^*(\boldsymbol{n}) \, e^{ik\chi \cos\theta} \tag{2.27}$$

where $\boldsymbol{k} \cdot \boldsymbol{x} = k\chi \cos\theta$ follows from our choice of coordinate system. The exponential term may be rewritten using (A.6). When substituted back into (2.27), this gives

$$
\begin{aligned}
a_{\ell m} &= \frac{1}{(2\pi)^3} \int \mathrm{d}^3k \ \delta_{g\boldsymbol{k}} \int \mathrm{d}\Omega_{\boldsymbol{n}} \ Y_{\ell m}^*(\boldsymbol{n}) \sum_{\ell'=0}^{\infty} (2\ell'+1) i^{\ell'} \mathcal{L}_{\ell'}(\cos\theta) j_{\ell'}(k\chi) \\
&= \frac{1}{(2\pi)^3} \int \mathrm{d}^3k \ \delta_{g\boldsymbol{k}} \sum_{\ell'=0}^{\infty} (2\ell'+1) i^{\ell'} j_{\ell'}(k\chi) \left(\int \mathrm{d}\Omega_{\boldsymbol{n}} \ \mathcal{L}_{\ell'}(\cos\theta) Y_{\ell m}^*(\boldsymbol{n}) \right) .
\end{aligned}
\tag{2.28}
$$

The simplification of the integral term in brackets requires some manipulation. If we expand a Legendre polynomial into spherical harmonics, we have (by (A.4)):

$$
\mathcal{L}_{\ell'}(\hat{\boldsymbol{k}} \cdot \boldsymbol{n}) = \frac{4\pi}{2\ell'+1} \sum_{m'=-\ell'}^{\ell'} Y_{\ell'm'}(\boldsymbol{n}) Y_{\ell'm'}^*(\hat{\boldsymbol{k}})
\tag{2.29}
$$

where our choice of coordinates implies that $\boldsymbol{k} \cdot \boldsymbol{n} = \cos\theta$. Thus the integral term becomes

$$
\begin{aligned}
\int \mathrm{d}\Omega_{\boldsymbol{n}} \ \mathcal{L}_{\ell'}(\cos\theta) Y_{\ell m}^*(\boldsymbol{n}) &= \int \mathrm{d}\Omega_{\boldsymbol{n}} \ \frac{4\pi}{2\ell'+1} \sum_{m'=-\ell'}^{\ell'} Y_{\ell'm'}(\boldsymbol{n}) Y_{\ell'm'}^*(\hat{\boldsymbol{k}}) Y_{\ell m}^*(\boldsymbol{n}) \\
&= \frac{4\pi}{2\ell'+1} \sum_{m'=-\ell'}^{\ell'} Y_{\ell'm'}^*(\hat{\boldsymbol{k}}) \int \mathrm{d}\Omega_{\boldsymbol{n}} \ Y_{\ell'm'}(\boldsymbol{n}) Y_{\ell m}^*(\boldsymbol{n}) \\
&= \frac{4\pi}{2\ell'+1} Y_{\ell'm}^*(\hat{\boldsymbol{k}}) \delta_{\ell\ell'} ,
\end{aligned}
\tag{2.30}
$$

where the result follows from the orthonormality relation (A.5). Substituting this back into (2.28), we obtain

$$
\begin{aligned}
a_{\ell m} &= \frac{1}{(2\pi)^3} \int \mathrm{d}^3k \ \delta_{g\boldsymbol{k}} \sum_{\ell'=0}^{\infty} (2\ell'+1) i^{\ell'} j_{\ell'}(k\chi) \frac{4\pi}{2\ell'+1} Y_{\ell'm}^*(\hat{\boldsymbol{k}}) \delta_{\ell\ell'} \\
&= \frac{i^{\ell}}{2\pi^2} \int \mathrm{d}^3k \ \delta_{g\boldsymbol{k}} \ j_{\ell}(k\chi) Y_{\ell m}^*(\hat{\boldsymbol{k}})
\end{aligned}
\tag{2.31}
$$

The complex conjugate is then given by

$$
a_{\ell m}^* = \frac{(-i)^{\ell}}{2\pi^2} \int \mathrm{d}^3k \ \delta_{g\boldsymbol{k}}^* \ j_{\ell}(k\chi) Y_{\ell m}(\hat{\boldsymbol{k}}) .
\tag{2.32}
$$

The integral in k is over all scales. However, since the Bessel functions are strongly peaked around $k\chi \sim \ell$, they act as weighting functions, with each multipole gaining a dominant contribution from only one wave number (or equivalently, a particular scale)

to first approximation. It is also important to note that since δ is a Gaussian random variable, so are the $a_{\ell m}$.

2.1.4 The statistical properties of the $a_{\ell m}$ and relation to the 3D power spectrum

The statistical properties of the $a_{\ell m}$ are thus:

$$\langle a_{\ell m} \rangle = 0 \,, \tag{2.33}$$

$$\langle a_{\ell m} a_{\ell' m'}^* \rangle = C_\ell \delta_{\ell \ell'} \delta_{mm'} \,, \tag{2.34}$$

where the primed and unprimed indices indicate that the coefficients are not necessarily both evaluated at the same redshift. These properties indicate that the $a_{\ell m}$ have zero mean and a variance described by the C_ℓ. The C_ℓ are referred to as the angular power spectrum (APS) and are defined in a model-independent fashion as

$$\langle a_{\ell m}(k\chi_1) a_{\ell' m'}^*(k\chi_2) \rangle = \frac{i^\ell(-i)^{\ell'}}{4\pi^4} \int \mathrm{d}^3 k \int \mathrm{d}^3 k' \, j_\ell(k\chi_1) \, j_{\ell'}(k'\chi_2) Y_{\ell m}^*(\hat{\boldsymbol{k}}) \, Y_{\ell' m'}(\hat{\boldsymbol{k}}')$$
$$\times \langle \delta_{g\boldsymbol{k}}(z_1) \, \delta_{g\boldsymbol{k}'}^*(z_2) \rangle \,. \tag{2.35}$$

It is also possible to relate the angular power spectrum to the 3D power spectrum P_g defined earlier, using the definitions of $a_{\ell m}$ and its complex conjugate (see (2.31) and (2.32)):

$$\langle a_{\ell m}(k\chi_1) a_{\ell' m'}^*(k\chi_2) \rangle = i^\ell(-i)^{\ell'} \frac{2}{\pi} \int \mathrm{d}^3 k \int \mathrm{d}^3 k' \, j_\ell(k\chi_1) \, j_{\ell'}(k'\chi_2) Y_{\ell m}^*(\hat{\boldsymbol{k}}) \, Y_{\ell' m'}(\hat{\boldsymbol{k}}')$$
$$\times \delta_D(\boldsymbol{k} - \boldsymbol{k}') P_g(\boldsymbol{k}, z_1, z_2)$$
$$= \frac{2}{\pi} \int k^2 \mathrm{d}k \, j_\ell(k\chi_1) \, j_{\ell'}(k\chi_2) P_g(\boldsymbol{k}, z_1, z_2) \delta_{\ell \ell'} \delta_{mm'} \,, \tag{2.36}$$

where $\chi_i = \chi(z_i)$ and the last step uses the orthonormality relation, (A.5). Here the $a_{\ell m}$ are represented in terms of the galaxy power spectrum $P_g(\boldsymbol{k}, z_1, z_2)$, which is formally defined by

$$P_g(\boldsymbol{k}, z_1, z_2) = \langle \delta_{g\boldsymbol{k}}(z_1) \delta_{g\boldsymbol{k}}(z_2) \rangle \,. \tag{2.37}$$

The C_ℓ of the APS also provides another possible basis for the expansion of the two-point correlation function. Consider the situation depicted in Fig. 2.1. From the definition of

the two-point correlation function, we have:

$$\xi_g(r) = \langle \delta_g(\boldsymbol{x}_1)\delta_g(\boldsymbol{x}_2)\rangle \tag{2.38}$$

Recall from (2.24) that the density contrast $\delta(\boldsymbol{x})$ may be expanded in terms of spherical harmonics $a_{\ell m}(\chi(z))$:

$$\delta_g(\boldsymbol{x}_i) = \delta_g(\boldsymbol{n}_i, z_i) = \sum_{\ell=0}^{\infty}\sum_{m=-\ell}^{\ell} a_{\ell m}(\chi(z_i))Y_{\ell m}(\boldsymbol{n}_i)\,, \tag{2.39}$$

so that the angular spectrum is defined (as in (2.34)) by

$$\langle a_{\ell m}(z_1)a_{\ell'm'}^*(z_2)\rangle = C_\ell(z_1, z_2)\delta_{\ell\ell'}\delta_{mm'}\,. \tag{2.40}$$

Hence, we may rewrite ξ:[2]

$$
\begin{aligned}
\xi_g(r) &= \left\langle \sum_{\ell=0}^{\infty}\sum_{m=-\ell}^{\ell} a_{\ell m}(\chi(z_1))Y_{\ell m}(\boldsymbol{n}_1) \sum_{\ell'=0}^{\infty}\sum_{m'=-\ell'}^{\ell'} a_{\ell'm'}^*(\chi(z_2))Y_{\ell'm'}(\boldsymbol{n}_2)\right\rangle \\
&= \sum_{\ell,m}\sum_{\ell',m'} \langle a_{\ell m}a_{\ell'm'}^*\rangle Y_{\ell m}(\boldsymbol{n}_1)Y_{\ell'm'}^*(\boldsymbol{n}_2) \\
&= \sum_{\ell,m}\sum_{\ell',m'} (C_\ell\delta_{\ell\ell'}\delta_{mm'})Y_{\ell m}(\boldsymbol{n}_1)Y_{\ell'm'}^*(\boldsymbol{n}_2) \\
&= \sum_{\ell} C_\ell\left(\frac{2\ell+1}{4\pi}\mathcal{L}_\ell(\boldsymbol{n}_1\cdot\boldsymbol{n}_2)\right),
\end{aligned}
\tag{2.41}
$$

where some of the arguments and sums are suppressed after the first line for the sake of brevity, and the final step uses (A.4). Thus, the expression for the expansion of ξ_g, reintroducing the correct dependences, is:

$$\xi_g(z_1, z_2, \boldsymbol{n}_1, \boldsymbol{n}_2) = \sum_{\ell=0}^{\infty} \frac{(2\ell+1)}{4\pi}C_\ell(z_1, z_2)\mathcal{L}_\ell(\boldsymbol{n}_1\cdot\boldsymbol{n}_2)\,, \tag{2.42}$$

where the various arguments are described in Fig. 2.1.

---

[2]When defined for the density, the conjugate $\delta^*(\boldsymbol{x}_2)$ is the same as $\delta(\boldsymbol{x}_2)$ since the density contrast is purely real.

2.1.5   Relation to the power spectrum of primordial curvature fluctuations

Conventionally the C_ℓ's are written in terms of the primordial curvature perturbations. Using the Fourier transform of the Poisson equation (see (1.91)), we find that

$$\frac{3}{2}\frac{\Omega_{m0}H_0^2}{a}\delta_{C\boldsymbol{k}}(z) = -k^2\Phi(\boldsymbol{k},z) \ . \tag{2.43}$$

However, the potential Φ can be related to the primordial curvature perturbations. First, we re-express Φ in terms of useful ratios, following the approach in [1]:

$$\Phi(k,a) \quad = \quad \Phi_{LS}(\boldsymbol{k},a_d)\frac{\Phi(k,a_d)}{\Phi_{LS}(\boldsymbol{k},a_d)}\frac{\Phi(k,a)}{\Phi(k,a_d)} \ , \tag{2.44}$$

where a_d refers to scale factors corresponding to times sufficiently later than equality that matter dominates and growth becomes scale-independent (i.e. decoupling) and $\Phi_{LS}(k,a_d)$ corresponds to the potential on large scales in the matter-dominated case [1]:

$$\Phi_{LS}(\boldsymbol{k},a_d) = \frac{9}{10}\Phi_p(\boldsymbol{k}) \ . \tag{2.45}$$

This can be re-written using the following definitions for the transfer function $T(k)$ and growth function $g(z)$ (see Chapter 1):

$$T(k) \quad \equiv \quad \frac{\Phi(k,a_d)}{\Phi_{LS}(\boldsymbol{k},a_d)} \ , \tag{2.46}$$

$$\frac{g(a)}{g_d} \quad \equiv \quad \frac{\Phi(k,a)}{\Phi(k,a_d)} \equiv \frac{D(a)}{a} \ . \tag{2.47}$$

In this way, $T(k)$ controls the scale-dependent changes in amplitude and is normalized to unity on large scales, while $g(a)$ is normalized to unity at the time of matter-radiation decoupling and describes the late-time scale-independent growth of the perturbations. Thus, our expression for Φ is now

$$\Phi(k,a) = \Phi_{LS}(\boldsymbol{k},a_d)\,T(k)\,\frac{D(a)}{a} \ , \qquad \text{for } a > a_d \ . \tag{2.48}$$

On large scales, during matter domination, the relationship between Φ and the field of primordial curvature fluctuations ζ is given by

$$\Phi_{LS}(\boldsymbol{k}, a_d) = -\frac{3}{5}\zeta(\boldsymbol{k}) \ . \tag{2.49}$$

The relation between Φ and ζ is then

$$\Phi(\boldsymbol{k}, a) = -\frac{3}{5} \ T(k) \ \frac{D(a)}{a} \ \zeta(\boldsymbol{k}) \ , \qquad \text{for } a > a_d \ . \tag{2.50}$$

Thus, (2.43) becomes

$$\delta_{C\boldsymbol{k}}(z) = \frac{2}{5} \frac{D(a) \ T(k) \ k^2}{\Omega_{m0}H_0^2 \ g_{\rm d}}\zeta(\boldsymbol{k}) \ , \tag{2.51}$$

where $g_{\rm d}$ may be determined from the following fitting formula [114]:

$$g(z) = \frac{5}{2}g_{\rm d}\Omega_m(z) \left[\Omega_m(z)^{4/7} - \Omega_\Lambda(z) + \left(1 + \frac{1}{2}\Omega_m(z)\right)\left(1 + \frac{1}{70}\Omega_\Lambda(z)\right)\right]^{-1} \ , \tag{2.52}$$

where g is normalized so that $g(z = z_{\rm d}) = 1$.

Thus, the conventional definition of C_ℓ is

$$C_\ell(z_1, z_2) = A \int \mathrm{d}\ln k \ \Delta_\ell(k, z_1) \ \Delta_\ell(k, z_2)\mathcal{P}_\zeta(k) \ , \tag{2.53}$$

where $\mathcal{P}_\zeta(k)$ is the dimensionless power spectrum of the primordial curvature fluctuations $\left(\mathcal{P}_\zeta(k) \equiv k^3 P_\zeta(k)/2\pi^2\right)$ and we have:

$$A = \frac{16\pi}{(5\Omega_{m0}H_0^2 \ g_{\rm d})^2} \ , \tag{2.54}$$

$$\Delta_\ell(k, z) = b(z)D(z) \ T(k) \ j_\ell(k\chi(z)) \ k^2 \ , \tag{2.55}$$

where b is the galaxy bias (see 3). The Δ_ℓ are the angular transfer functions which store information about the changes in amplitude of the fluctuations in galaxy number density relative to ζ, while the information about their stochasticity is confined to $\mathcal{P}_\zeta(k)$. The same result is found in [18], including extra terms which take into account the fact that the D_g considered therein is not comoving.

2.2 Correction for window function

Until now, all the derivations have been for the special case that the spherical shell we consider is infinitesimally thin. This means that observations are assumed to occur at only one value of redshift. In mathematical terms, this amounts to assuming a galaxy distribution in redshift that is a delta function. However, when actual observations are made, there is a spread in the redshifts of the observed galaxies, characterized by a window function. These window functions effectively determine bins or redshift ranges within which galaxies are counted, with a mean redshift $\hat{z}$ that is used to calculate noise and other characteristics. In the case that the window function is not a Dirac delta, (2.53) no longer holds and must be generalized to

$$C_\ell^W(z_1, z_2) = A \int d\ln k \; \Delta_\ell^W(k, z_1) \; \Delta_\ell^W(k, z_2) \mathcal{P}_\zeta(k) , \qquad (2.56)$$

where Δ_ℓ^W is the angular transfer function for the galaxy number density contrast, taking into account their window function $W(\hat{z})$ (a galaxy redshift distribution) and is given by

$$\Delta_\ell^W(k, \hat{z}) = \int dz \; W(\hat{z}, z) \Delta_\ell(k, z) , \qquad (2.57)$$

following [45] and [18], where the integration is over the redshift bin containing $\hat{z}$. The effect of a window function is included in the $a_{\ell m}$ by integrating over redshift:

$$a_{\ell m}^W(\hat{z}) \;\; = \;\; \int dz \; W(\hat{z}, z) \; a_{\ell m}(z) , \qquad (2.58)$$

where the superscript W indicates the inclusion of the effect of a window function. In particular, for the density contrast we have:

$$a_{\ell m}^W(\hat{z}) \;\; = \;\; \frac{i^\ell}{2\pi^2} \int d^3k \; dz \; W(\hat{z}, z) \; \delta(\boldsymbol{k}, z) \; j_\ell(k\chi) Y_{\ell m}^*(\hat{\boldsymbol{k}}) , \qquad (2.59)$$

and

$$C_\ell^W(z_1, z_2) = A \int d^3k \; dz \; \Delta_\ell^W(k, z_1) \Delta_\ell^W(k, z_2) \mathcal{P}_\zeta(k) , \qquad (2.60)$$

where

$$\Delta_\ell^W(k, \hat{z}) = \int dz \; W(\hat{z}, z) \; D(z) \; T(k) \; k^2 \; j_\ell(k\chi(z)) . \qquad (2.61)$$

Chapter 3

Lightcone Effects

Up until this point, we have derived expressions for the theoretical angular power spec-
trum of the galaxy number density contrast, but this is not what is directly observed. In
this chapter we consider the observed galaxy number counts, following closely the argu-
ments set out in [18]. In making this transition, there is a subtlety that must be taken
into account. The quantity measured in observations is the number of galaxies, but the
fluctuations in number measured by the observer are not the same as the fluctuations in
the number density measured at the source. Thus, the definition of the density contrast
used so far is slightly different to what is actually observed. This is because we make
observations on the past lightcone where various relativistic effects lead to additional
corrections.

Therefore, we carefully examine the definitions of the theoretical and observed quanti-
ties in order that we may relate them. We note that, in the definition of the galaxy
number density contrast (2.13), the background density $\bar{\rho}$ is taken to be measured at
the background redshift $\bar{z}$. However, the actual measured redshift is itself perturbed
and this must be taken into account before we can relate the expressions of the previous
chapter to observations. This leads to additional terms which are naturally grouped
as *redshift corrections* and *volume corrections*. We then consider the implications for
the calculation of the angular power spectrum and perform a detailed derivation of the
corresponding C_ℓ components of two standard terms (density and redshift-space distor-
tions). Following this, we consider deviations in a photon geodesic along the line of sight
as the photon passes through space from the source to the observer, describing these

43

as deviations in the luminosity distance. Using the resultant description we are able to derive detailed expressions for the additional redshift and volume correction terms, following closely the arguments and formalism set out in [18] and [49] with aid from [50].

3.1 Perturbations in the number density of galaxies

In the case of actual observations, the quantity of interest is not directly the galaxy density contrast, but rather the perturbation in the observed number counts of galaxies Δ, which is defined in [18] as

$$\Delta(\boldsymbol{n}, z) \;=\; \frac{N(\boldsymbol{n}, z) - \bar{N}(z)}{\bar{N}(z)} \;. \tag{3.1}$$

The number of sources counted by the observer in a solid angle $d\Omega_{\boldsymbol{n}}$ and redshift interval $\mathrm{d}z$ is given by (see Fig. 3.1)

$$d\mathcal{N} = N \, \mathrm{d}z \, \mathrm{d}\Omega_{\boldsymbol{n}} = \rho_g \mathrm{d}V \;. \tag{3.2}$$

Here N is the number of galaxies counted by the observer per redshift, per solid angle. By contrast, ρ_g is the proper number density, which is not measured by the observer, but is the quantity that would be measured in the source rest-frame. The observed volume element is $\mathrm{d}z \, \mathrm{d}\Omega_{\boldsymbol{n}}$, whereas $\mathrm{d}V$ is not the observed volume element, rather the proper volume element as measured by the source. Hence, the observed number density contrast is related to the proper number density contrast at the source by

$$\Delta \equiv \delta_N = \delta_g + \text{lightcone effects} \;, \tag{3.3}$$

where $\delta_g \equiv \delta\rho_g/\bar{\rho}_g$, as in (2.13).

In (3.1), $\bar{N}$ refers to the background value of N - its average over all observable directions. It is important to note that the definition specifies $\bar{N}$ taken at observed z and not $\bar{z}$ in the background. The latter would be analogous to the definition of the density contrast in (2.1) or (2.13) and would not account for the perturbations in redshift. In this chapter we will be explicit with the nature of the redshift, specifically whether it is a background or perturbed variable.
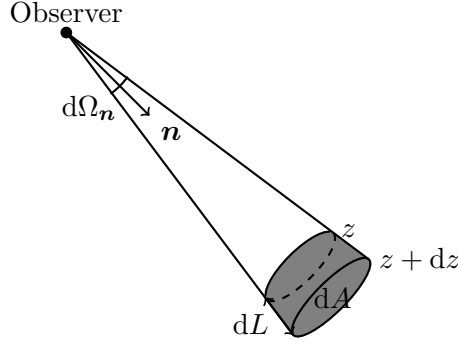
FIGURE 3.1: This figure shows an observation of sources within a particular redshift range $(z, z + \mathrm{d}z)$ and solid angle $\mathrm{d}\Omega_{\boldsymbol{n}}$ with labels for various quantities that will be useful in defining different measures of volume and number counts.

The galaxy number density contrast measured at the source is

$$\delta_g(\boldsymbol{n}, z) = \frac{\rho_g(\boldsymbol{n}, z) - \bar{\rho}_g(\bar{z})}{\bar{\rho}_g(\bar{z})} \,. \tag{3.4}$$

Because of the subtleties in this and related definitions, we spend some time here to make sure that all of the relevant quantities are unambiguously defined, following the work of [60]. First, we consider the observed number density and its relation to the observed volume and number counts.

The observed volume element (shaded in Fig. 3.1) of thickness $\mathrm{d}z$ in a solid angle $\mathrm{d}\Omega_{\boldsymbol{n}}$ about the unit direction of observation $\boldsymbol{n}$, has proper volume at the source given (in the background) by

$$\begin{aligned}
\mathrm{d}\bar{V}(\bar{z}, \boldsymbol{n}) &= \mathrm{d}\bar{A}(\bar{z}, \boldsymbol{n}) \, \mathrm{d}\bar{L}(\bar{z}, \boldsymbol{n}) = \left[d_{\mathrm{A}}^2(\bar{z}) \, \mathrm{d}\bar{\Omega} \right] \left[a(\bar{z}) \mathrm{d}\chi \right] \\
&= \frac{d_{\mathrm{A}}^2(\bar{z})}{(1 + \bar{z}) H(\bar{z})} \, \mathrm{d}\bar{\Omega} \, \mathrm{d}\bar{z} \,.
\end{aligned} \tag{3.5}$$

where d_{A} is the angular diameter distance along the line of sight. The comoving volume element is thus

$$\mathrm{d}\bar{V}_{\mathrm{com}} = \frac{\mathrm{d}\bar{V}}{a^3} = \frac{d_{\mathrm{A}}^2(\bar{z})(1 + \bar{z})^2}{H(\bar{z})} \, \mathrm{d}\bar{\Omega} \, \mathrm{d}\bar{z} = \frac{\chi^2}{H(\bar{z})} \, \mathrm{d}\bar{\Omega} \, \mathrm{d}\bar{z} \,, \tag{3.6}$$

where $\chi = (1 + z) d_{\mathrm{A}}$ is the comoving distance along the line of sight.

The background number of sources $\mathrm{d}\bar{\mathcal{N}}$ observed in the volume element is given by (3.2)

$$\mathrm{d}\bar{\mathcal{N}}(\bar{z}, \boldsymbol{n}) = \bar{N}(\bar{z}) \, \mathrm{d}\bar{z} \, \mathrm{d}\bar{\Omega} \,, \tag{3.7}$$

where $\bar{N}$ is the observed background redshift distribution. A typical model for galaxy surveys is of the form

$$\bar{N} = \frac{\mathrm{d}\bar{\mathcal{N}}}{\mathrm{d}\bar{z}\,\mathrm{d}\bar{\Omega}} \propto \bar{z}^2 \exp\left[-\left(\frac{\bar{z}}{\bar{z}_{\mathrm{m}}}\right)^{3/2}\right].$$ (3.8)

We can also write the background number counts in terms of the volume element at the source, as in (3.2). The observed background number per $\bar{z}$ per Ω are therefore related to the proper number density at the source by

$$\bar{N}(\bar{z}) = \bar{\rho}_g \frac{\bar{d}_A^2(\bar{z})}{(1+\bar{z})H(\bar{z})},$$ (3.9)

which we can rewrite as

$$\bar{N}(\bar{z}) = \bar{\rho}_g a^3 \times \frac{\chi^2}{H(\bar{z})}$$ (3.10)

to make it clear that $\bar{N}$ is the product of the comoving background number density $(\bar{\rho}_g a^3)$ and the comoving volume element per redshift per solid angle. Note that this is not the quantity that appears in the definition of the perturbation in galaxy number counts (3.1), because the redshift and volume are perturbed and so we cannot rely on the background alone. In order to relate δ_g and Δ we must first examine the relation of $\bar{N}(z)$ to $\bar{N}(\bar{z})$.

3.1.1 Relating Δ to δ_g

Following the arguments set out in [18], Δ may be related to the perturbation variable $\delta_{g,z}$ which is the source number density contrast at fixed observed redshift:

$$
\begin{aligned}
\delta_{g,z}(\boldsymbol{n}, z) &= \frac{\rho_g(\boldsymbol{n},z) - \bar{\rho}_g(z)}{\bar{\rho}_g(z)} = \frac{\dfrac{N(\boldsymbol{n},z)}{V(\boldsymbol{n},z)} - \dfrac{\bar{N}(z)}{\bar{V}(z)}}{\dfrac{\bar{N}(z)}{\bar{V}(z)}} \\
&= \left(\frac{N(\boldsymbol{n},z)}{\bar{V}(z) + \delta V(\boldsymbol{n},z)} - \frac{\bar{N}(z)}{\bar{V}(z)}\right)\frac{\bar{V}(z)}{\bar{N}(z)} \\
&= \frac{N(\boldsymbol{n},z)\bar{V}(z) - \bar{N}(z)[\bar{V}(z) + \delta V(\boldsymbol{n},z)]}{\bar{N}(z)\left[\bar{V}(z) + \delta V(\boldsymbol{n},z)\right]} \\
&= \left(\frac{N(\boldsymbol{n},z) - \bar{N}(z)}{\bar{N}(z)} - \frac{\delta V(\boldsymbol{n},z)}{\bar{V}(z)}\right)\frac{\bar{V}(z)}{\bar{V}(z) + \delta V(\boldsymbol{n},z)},
\end{aligned}
$$ (3.11)

where ρ_g is the number density of galaxies and in the second line we have assumed that the volume can be written as the sum of a background term and a perturbation: $V(\boldsymbol{n}, z) = \bar{V}(z) + \delta V(\boldsymbol{n}, z)$. This expression may be further simplified as follows:

$$
\begin{aligned}
\delta_{g,z}(\boldsymbol{n}, z) &\approx \left(\frac{N(\boldsymbol{n}, z) - \bar{N}(z)}{\bar{N}(z)} - \frac{\delta V(\boldsymbol{n}, z)}{\bar{V}(z)} \right) \left(1 - \frac{\delta V(\boldsymbol{n}, z)}{\bar{V}(z)} \right) \\
&\approx \frac{N(\boldsymbol{n}, z) - \bar{N}(z)}{\bar{N}(z)} - \frac{\delta V(\boldsymbol{n}, z)}{\bar{V}(z)} \,,
\end{aligned}
\tag{3.12}
$$

up to first order. Hence

$$
\Delta(\boldsymbol{n}, z) = \delta_{g,z}(\boldsymbol{n}, z) + \frac{\delta V(\boldsymbol{n}, z)}{\bar{V}(z)} \,.
\tag{3.13}
$$

Note the difference between the above definition of $\delta_{g,z}(\boldsymbol{n}, z)$ and the $\delta_g(\boldsymbol{n}, z)$ defined in (3.4). The subtle distinctions are described in [18] and the following derivation follows closely from the arguments laid out therein. The important subtlety here is the difference between perturbed and background redshifts. Comparing the definition of $\delta_{g,z}(\boldsymbol{n}, z)$ (3.11) with (3.4), we notice that $\delta_{g,z}(\boldsymbol{n}, z)$ does not assume that the average galaxy number density $\bar{\rho}_g$ is measured at the background value of the redshift, but also allows for the redshift itself to be perturbed. Hence, $\delta_{g,z}$ (and thus $\Delta(\boldsymbol{n}, z)$, by (3.13)) may be related to $\delta_g(\boldsymbol{n}, z)$ as follows:

$$
\begin{aligned}
\delta_{g,z}(\boldsymbol{n}, z) &= \frac{\rho_g(\boldsymbol{n}, z) - \bar{\rho}_g(z)}{\bar{\rho}_g(z)} = \frac{(\delta_g(\boldsymbol{n}, z)\bar{\rho}_g(\bar{z}) + \bar{\rho}_g(\bar{z})) - \bar{\rho}_g(z)}{\bar{\rho}_g(z)} \\
&= \delta_g(\boldsymbol{n}, z) - \frac{\partial \bar{\rho}_g}{\partial \bar{z}} \frac{\delta z(\boldsymbol{n}, z)}{\bar{\rho}_g(\bar{z})} \,,
\end{aligned}
\tag{3.14}
$$

where the final step uses a first-order Taylor expansion of $\bar{\rho}_g$:

$$
\bar{\rho}_g(z) = \bar{\rho}_g(\bar{z}) + \frac{\partial \bar{\rho}_g}{\partial \bar{z}} \delta z(\boldsymbol{n}, z) \,.
\tag{3.15}
$$

In this way, the measured Δ and δ_g are related by

$$
\Delta(\boldsymbol{n}, z) = \delta_g(\boldsymbol{n}, z) - \frac{\partial \bar{\rho}_g}{\partial \bar{z}} \frac{\delta z(\boldsymbol{n}, z)}{\bar{\rho}_g(\bar{z})} + \frac{\delta V(\boldsymbol{n}, z)}{\bar{V}(z)} \,.
\tag{3.16}
$$

There are two corrective terms to the galaxy number density contrast which we will refer to hereafter as the redshift correction: $\frac{d\bar{\rho}_g}{d\bar{z}} \frac{\delta z(\boldsymbol{n}, z)}{\bar{\rho}_g(\bar{z})}$ and the volume correction: $\frac{\delta V(\boldsymbol{n}, z)}{\bar{V}(z)}$.

3.1.2 Relating δ_g and δ_m

A bias factor can be introduced to relate the matter density perturbations and the fluctuations in galaxy number counts. On scales where linear perturbations are accurate, it is assumed to be scale independent. It must be defined in the matter rest-frame, which coincides with the comoving gauge (C) [45, 61]. It is defined between the density perturbations in this gauge as follows:

$$\delta_{gC}(\boldsymbol{x}, \eta) = b(\eta)\delta_{mC}(\boldsymbol{x}, \eta) , \tag{3.17}$$

where the subscripts g and m indicate perturbations in galaxy number density and matter density, respectively. The transformation between the Poisson gauge and the comoving gauge is given by [44]

$$\delta\beta_{\mathrm{C}} = \delta\beta - \bar{\beta}'V , \tag{3.18}$$

for the perturbation $\delta\beta$ in some quantity β and where V is the velocity potential. Hence, for δ_g, we have

$$\delta_g = \delta_{g\mathrm{C}} + \frac{\bar{\rho}'_g}{\bar{\rho}_g}V . \tag{3.19}$$

If we define a quantity b_e as the dimensionless measure of the extent to which comoving galaxy number density is *not* conserved, i.e.

$$b_e = \frac{1}{\mathcal{H}} \frac{(a^3\bar{\rho}_g)'}{a^3\bar{\rho}_g} , \tag{3.20}$$

then [45]

$$\begin{aligned}
\delta_g &= \delta_{g\mathrm{C}} + (b_e - 3)\mathcal{H}V , \\
&= b\delta_{m\mathrm{C}} + (b_e - 3)\mathcal{H}V .
\end{aligned} \tag{3.21}$$

b_e is called the evolution bias and it will be described in more detail later (see Section 3.4.1). The expression for the observed perturbations in number counts is thus given by

$$\Delta(\boldsymbol{n}, z) = b(z)\delta_{mC}(\boldsymbol{n}, z) + (b_e(z) - 3)\mathcal{H}(z)V(\boldsymbol{n}, z) - \frac{\partial\bar{\rho}_g}{\partial\bar{z}}\frac{\delta z(\boldsymbol{n}, z)}{\bar{\rho}_g(\bar{z})} + \frac{\delta V(\boldsymbol{n}, z)}{\bar{V}(z)} . \tag{3.22}$$

3.1.3 Redefining $a_{\ell m}$

Since Δ is the variable that is actually measured, it makes sense to redefine the $a_{\ell m}$ and C_ℓ using the decomposition of Δ in spherical harmonics. Thus, similarly to before, we have

$$\Delta(\boldsymbol{n}, z) = \sum_{\ell=0}^{\infty} \sum_{m=-\ell}^{\ell} a_{\ell m}(z) Y_{\ell m}(\boldsymbol{n}) \,, \tag{3.23}$$

with

$$a_{\ell m}(z) = \int \mathrm{d}\Omega_{\boldsymbol{n}} \ \Delta(\boldsymbol{n}, z) Y_{\ell m}^*(\boldsymbol{n}) = \frac{i^\ell}{2\pi^2} \int \mathrm{d}^3 k \ \Delta(\boldsymbol{k}, z) j_\ell(k\chi) Y_{\ell m}^*(\boldsymbol{k}) \,, \tag{3.24}$$

and

$$C_\ell(z_1, z_2) = A \int \mathrm{d}\ln k \ \Delta_\ell(k, z_1) \ \Delta_\ell(k, z_2) \mathcal{P}_\zeta(k) \,, \tag{3.25}$$

where the Δ_ℓ now store information about the amplitudes of the fluctuations in observed galaxy number density as opposed to source number density. As shown in (3.16) above, $\Delta(\boldsymbol{n}, z)$ is separable into additive terms. In the following derivations, the contributions of each term named X will be written with a superscript label:

$$a_{\ell m}^X(z) = \int \mathrm{d}\Omega_{\boldsymbol{n}} \ \Delta^X(\boldsymbol{n}, z)(\boldsymbol{n}, z)(\boldsymbol{n}, z) Y_{\ell m}^*(\boldsymbol{n}) = \frac{i^\ell}{2\pi^2} \int \mathrm{d}^3 k \ \Delta^X(\boldsymbol{k}, z) j_\ell(k\chi) Y_{\ell m}^*(\boldsymbol{k}) \,. \tag{3.26}$$

For example, the first term of $\Delta(\boldsymbol{n}, z)$ in (3.22) will be referred to as $a_{\ell m}^\delta$:

$$a_{\ell m}^\delta(z) = \frac{i^\ell}{2\pi^2} \int \mathrm{d}^3 k \ \delta_g(\boldsymbol{k}, z) j_\ell(k\chi) Y_{\ell m}^*(\boldsymbol{k}) \,, \tag{3.27}$$

with $a_{\ell m}$ reserved for the full expression of the projection coefficients including all contributions, as defined in (3.24). The expression for the C_ℓ corresponding to (3.27) is then

$$C_\ell^\delta(z_1, z_2) = A \int \mathrm{d}\ln k \ \Delta_\ell^\delta(k, z_1) \ \Delta_\ell^\delta(k, z_2) \mathcal{P}_\zeta(k) \,, \tag{3.28}$$

where

$$\Delta_\ell^\delta(k, z) = b(z) \ D(z) \ T(k) \ j_\ell(k\chi(z)) \ k^2 \,, \tag{3.29}$$

as in (2.55).

In the following sections we will examine the redshift and volume corrections in greater detail, deriving full expressions for their components.

3.2 Redshift-space distortions

The peculiar velocities that galaxies possess affect their apparent location, causing a perturbation in the volume used to compute densities. Redshift-space distortion (RSD) refers to the component of this effect along the line of sight and in real space this gives a correction to $\Delta(\boldsymbol{n}, z)$ of

$$\Delta^{RSD}(\boldsymbol{n}, z) = -\frac{1}{\mathcal{H}(z)} \frac{\partial}{\partial \chi} (\boldsymbol{v}(\boldsymbol{n}, z) \cdot \boldsymbol{n}) = -\frac{1}{\mathcal{H}(z)} \boldsymbol{n} \cdot \nabla (\boldsymbol{v}(\boldsymbol{n}, z) \cdot \boldsymbol{n}) . \tag{3.30}$$

This is commonly referred to as the Kaiser formula, originally derived in [47]. This correction arises from the redshift correction term in (3.16), as will be shown in a later section (see 3.4). For the moment, we take the correction in (3.30) as given and use it to illustrate the calculation of a C_ℓ component other than density. According to (3.26), the contribution to the $a_{\ell m}$ is thus

$$a_{\ell m}^{RSD}(z) = \int \mathrm{d}\Omega_{\boldsymbol{n}} \, \Delta^{RSD}(\boldsymbol{n}, z) Y_{\ell m}^*(\boldsymbol{n}) . \tag{3.31}$$

We can use the Fourier transform of the peculiar velocity field to rewrite the above expression as

$$
\begin{aligned}
a_{\ell m}^{RSD} &= -\int \mathrm{d}\Omega_{\boldsymbol{n}} \, \frac{1}{\mathcal{H}} \frac{\partial}{\partial \chi} \left[\frac{1}{(2\pi)^3} \int \mathrm{d}^3 k \, \boldsymbol{v_k} \cdot \boldsymbol{n} \, e^{i\chi \boldsymbol{k} \cdot \boldsymbol{n}} \right] Y_{\ell m}^*(\boldsymbol{n}) \\
&= -\int \mathrm{d}\Omega_{\boldsymbol{n}} \, \frac{1}{\mathcal{H}} \frac{\partial}{\partial \chi} \left[\frac{1}{(2\pi)^3} \int \mathrm{d}^3 k \, (i V_{\boldsymbol{k}} \boldsymbol{k}) \cdot \boldsymbol{n} \, e^{i\chi \boldsymbol{k} \cdot \boldsymbol{n}} \right] Y_{\ell m}^*(\boldsymbol{n}) \\
&= -\int \mathrm{d}\Omega_{\boldsymbol{n}} \, \frac{1}{\mathcal{H}} \frac{\partial}{\partial \chi} \left[\frac{1}{(2\pi)^3} \int \mathrm{d}^3 k \, \frac{i V_{\boldsymbol{k}}}{k} \, \boldsymbol{k} \cdot \boldsymbol{n} \, e^{i\chi \boldsymbol{k} \cdot \boldsymbol{n}} \right] Y_{\ell m}^*(\boldsymbol{n}) \\
&= -\int \mathrm{d}\Omega_{\boldsymbol{n}} \, \frac{1}{\mathcal{H}} \frac{\partial}{\partial \chi} \left[\frac{1}{(2\pi)^3} \int \mathrm{d}^3 k \, V_{\boldsymbol{k}} \frac{\partial}{\partial \chi} \, e^{i\chi \boldsymbol{k} \cdot \boldsymbol{n}} \right] Y_{\ell m}^*(\boldsymbol{n}) \\
&= \frac{-1}{(2\pi)^3 \mathcal{H}} \int \mathrm{d}^3 k \, V_{\boldsymbol{k}} k^2 \frac{\partial^2}{\partial (k\chi)^2} \left[\int \mathrm{d}\Omega_{\boldsymbol{n}} \, e^{i\chi k \cos\theta} Y_{\ell m}^*(\boldsymbol{n}) \right] \\
&= \frac{-i^\ell}{2\pi^2} \int \mathrm{d}^3 k \, \frac{k^2 V_{\boldsymbol{k}}}{\mathcal{H}} \, Y_{\ell m}^*(\boldsymbol{n}) \, j_\ell''(k\chi) , \tag{3.32}
\end{aligned}
$$

where we have used $\boldsymbol{x} = \chi \boldsymbol{n}$, $\boldsymbol{v} = \nabla V$ and $\boldsymbol{k} \cdot \boldsymbol{n} = k \cos\theta$ and where the derivative of j_ℓ is taken with respect to $k\chi$.[1] The final step in (3.32) follows from a result proved

---

[1]Note that this differs from (37) of [18], since there the magnitude of the velocity vector in Fourier space $v_{\boldsymbol{k}}$ is used, whereas we use the velovity potential $V_{\boldsymbol{k}}$.

previously (see (2.27) to (2.31)), i.e.

$$\int \mathrm{d}\Omega_{\boldsymbol{n}} e^{ik\chi\cos\theta} Y^*_{\ell m}(\boldsymbol{n}) = 4\pi i^\ell j_\ell(k\chi) Y^*_{\ell m}(\boldsymbol{k}). \tag{3.33}$$

From first-order perturbation theory, the continuity equation gives

$$\delta'_m + \nabla \cdot \boldsymbol{v} = 0 \,. \tag{3.34}$$

The growth rate f is defined by

$$\delta'_m = f\mathcal{H}\delta_m \tag{3.35}$$

Combining (3.34) and (3.35) and taking the Fourier transform gives

$$k^2 V_{\boldsymbol{k}} = -f\mathcal{H}\delta_{m,\boldsymbol{k}} \,, \tag{3.36}$$

which yields

$$a^{RSD}_{\ell m} = \frac{i^\ell}{2\pi^2} \int \mathrm{d}^3k \; f\delta_{m,\boldsymbol{k}} Y^*_{\ell m}(\boldsymbol{k}) \; j''_\ell(k\chi) \,. \tag{3.37}$$

The corresponding expression for the C_ℓ is then

$$
\begin{aligned}
C^{RSD}_\ell(z_1,z_2)\delta_{\ell\ell'}\delta_{mm'} &= \frac{i^\ell(-i)^{\ell'}}{4\pi^4} \int \mathrm{d}^3k \int \mathrm{d}^3k' f(z_1)f(z_2) \; j''_\ell(k\chi_1) \; j''_{\ell'}(k'\chi_2) \\
&\quad \times Y^*_{\ell m}(\boldsymbol{k}) \; Y_{\ell'm'}(\boldsymbol{k}') \langle \delta_{\boldsymbol{k}} \, \delta^*_{\boldsymbol{k}'} \rangle \\
&= \frac{2}{\pi} \int \mathrm{d}^3k \int \mathrm{d}^3k' \, f(z_1)f(z_2) \; j''_\ell(k\chi_1) \; j''_{\ell'}(k'\chi_2) Y^*_{\ell m}(\boldsymbol{k}) \; Y_{\ell'm'}(\boldsymbol{k}') \\
&\quad \times \delta_D(\boldsymbol{k}-\boldsymbol{k}') \left(\frac{2D(z) \, T(k) \, k^2}{5\Omega_{m0}H_0^2 g_\infty}\right)^2 P_\zeta(k,z) \\
&= \left(\frac{2}{5\Omega_{m0}H_0^2 g_\infty}\right)^2 \frac{2}{\pi} \int k^2\mathrm{d}k \; \mathrm{d}\Omega_k \; f(z_1)f(z_2)D(z_1)D(z_2)(T(k) \, k^2)^2 \\
&\quad \times j''_\ell(k\chi_1) \; j''_{\ell'}(k\chi_2)Y^*_{\ell m}(\boldsymbol{k}) \; Y_{\ell'm'}(\boldsymbol{k})P_\zeta(k,z) \\
&= A \int \frac{\mathrm{d}k}{k} \; f(z_1)f(z_2)D(z_1)D(z_2)(T(k) \, k^2)^2 \\
&\quad \times j''_\ell(k\chi_1) \; j''_{\ell'}(k\chi_2)\mathcal{P}_\zeta(k)\delta_{\ell\ell'}\delta_{mm'} \,,
\end{aligned}
\tag{3.38}
$$

where $\chi_i = \chi(z_i)$. The last step uses the orthonormality relation (A.5) and introduces the dimensionless power spectrum of ζ. Thus C^{RSD}_ℓ may be written as

$$C^{RSD}_\ell(z_1,z_2) = A \int \mathrm{d}\ln k \; \Delta^{RSD}_\ell(k,z_1) \; \Delta^{RSD}_\ell(k,z_2)\mathcal{P}_\zeta(k) \,, \tag{3.39}$$

where

$$\Delta_\ell^{RSD}(k, z) = f(z) \, D(z) \, T(k) \, k^2 \, j_\ell''(k\chi(z)) \,. \tag{3.40}$$

Finally, the effect of a window function may be included, giving

$$a_{\ell m}^{RSD,W}(\hat{z}) \;\; = \;\; \frac{i^\ell}{2\pi^2} \int d^3k \; dz \; W(\hat{z}, z) \, f(z) \, \delta_m(\boldsymbol{k}, z) Y_{\ell m}^*(\boldsymbol{k}) \, j_\ell''(k\chi(z)) \,, \quad \tag{3.41}$$

and

$$C_\ell^{RSD,W}(z_1, z_2) = A \int d^3k \; \Delta_\ell^{RSD,W}(k, z_1) \, \Delta_\ell^{RSD,W}(k, z_2) \, \mathcal{P}_\zeta(k) \,, \tag{3.42}$$

where

$$\Delta_\ell^{RSD,W}(k, \hat{z}) = \int dz \; W(\hat{z}, z) \, f(z) \, D(z) \, T(k) \, k^2 \, j_\ell''(k\chi(z)) \,. \tag{3.43}$$

3.3   Distortions in the luminosity distance

In order to derive the expressions for the redshift and volume corrections in (3.16), we can consider the perturbations in the geodesics of photons received from a source, which leads naturally to a description of fluctuations in the measured luminosity distance. Investigating these effects allows us develop a framework for expanding the expression for Δ into calculable terms.

3.3.1   Definitions

Suppose we have a source with known luminosity L, emitting a beam of photons at a point S in space-time. If we consider an observer who measures a flux F at an event O (see Figure 3.2), then the luminosity distance between the source and the observer is defined as

$$d_{\mathrm{L}}(S, O) = \sqrt{\frac{L}{4\pi F}} \,. \tag{3.44}$$

We consider a source and observer which have four-velocities u_S and u_O respectively and exist in an inhomogeneous, anisotropic Universe with metric $ds^2 = g_{\mu\nu}dx^\mu dx^\nu$. If
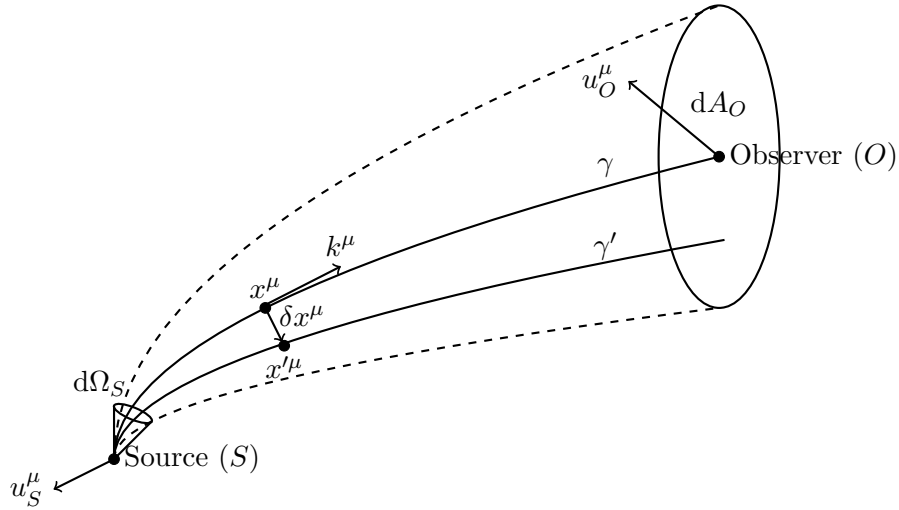
FIGURE 3.2: This figure shows the path taken by a photon (along geodesic γ) as it travels from a source to an observer. Definitions for various quantities are shown geometrically as is another geodesic (γ') which is distorted infinitesimally from the original.

the infinitesimal solid angle within which photons are emitted by the source is $d\Omega_S$, and dA_O is the infinitesimal area element on the screen space of O, i.e. the surface normal to the photon beam, then we have the following:

$$
\begin{aligned}
d_{\mathrm{L}}^2(S,O) \equiv \frac{L}{4\pi F} &= \frac{dE_S}{d\tau_S}\frac{1}{d\Omega_S}\frac{d\tau_O}{dE_O}dA_O \\
&= \frac{dE_S}{dE_O}\frac{d\tau_O}{d\tau_S}\frac{dA_O}{d\Omega_S} \\
&= (1+z)^2\frac{dA_O}{d\Omega_S} \,,
\end{aligned}
\tag{3.45}
$$

where the subscripts S and O indicate measurements made at the source and observer respectively and $1 + z = \frac{\omega_S}{\omega_O}$ is the redshift of the source as measured by the observer. As the grouping of terms in the second line above is meant to illustrate, one factor of $(1+z)$ arises due to the redshifting of the emitted energy along the photon's path, while the other is from the effect of time dilation due to the relative motion of observer and source.

Next, as done in [49], we parametrize the photon trajectories in the beam by a family of one-parameter curves: $x^\mu = f^\mu(\lambda, \boldsymbol{y})$, where λ now acts as an affine parameter along each light ray and the 3-vector $\boldsymbol{y}$ selects a particular ray.[2] The tangent vector to the

---

[2] $\boldsymbol{y}$ does not have a geometric definition in space time, and isn't included in Figure 3.2.

curve f^μ is

$$k^\mu(\lambda, \boldsymbol{y}) = \frac{\partial f^\mu(\lambda, \boldsymbol{y})}{\partial \lambda} \; . \tag{3.46}$$

This vector is the wave-vector (4-momentum) of the photon moving along the particular geodesic, at the point in space-time determined by λ. Following [49], in the rest-frame of an observer field with a 4-velocity u^μ (where $u^\mu(S) = u_S^\mu$ and $u^\mu(O) = u_O^\mu$), the **measured direction of a photon**, with affine parameter λ along a geodesic corresponding to $\boldsymbol{y}$, is given by

$$- n^\mu = \frac{1}{\omega}(k^\mu + k^\nu u_\nu u^\mu) = \frac{k^\mu}{\omega} - u^\mu \; , \tag{3.47}$$

where the minus sign on the left of the first equality arises since we adopt a convention *opposite* to [49] for the direction of observation $\boldsymbol{n}$ and where ω is the angular frequency of the photon:

$$\omega(\lambda, \boldsymbol{y}) = -g_{\mu\nu}(\lambda, \boldsymbol{y})k^\mu(\lambda, \boldsymbol{y})u^\nu(\lambda, \boldsymbol{y}) \; . \tag{3.48}$$

In particular, we consider the central photon beam γ, which is described by $f^\mu(\lambda, \boldsymbol{0})$, and an infinitesimally nearby geodesic γ' described by $f^\mu(\lambda, \delta\boldsymbol{y})$. We now examine the deviation in coordinates between these two geodesics, as measured in the rest-frame of an observer at $x^\mu = f^\mu(\lambda, \boldsymbol{0})$:

$$\delta x^\mu \equiv x'^\mu - x^\mu = \frac{\partial f^\mu}{\partial y^i}\delta y^i \; . \tag{3.49}$$

A useful result of this definition is that δx^μ and k^μ are orthogonal. The rays are generated simultaneously by event S and thus they will all have the same phase for equal values of λ, i.e. phase $\mathcal{S}$ is constant along the vectors in the field δx^μ, with $k_\mu = -\nabla_\mu \mathcal{S}$. Thus orthogonality is ensured:

$$\delta x^\mu k_\mu = -\delta x^\mu \nabla_\mu \mathcal{S} = -\nabla_{\delta \boldsymbol{x}} \mathcal{S} = 0 \; . \tag{3.50}$$

Next, following [49] and [50], we define a vector $\delta\theta^\mu$ which is a measure of the angular separation between the two geodesics γ and γ' (see Fig. 3.3):

$$
\begin{aligned}
\delta\theta^\mu &= \frac{\delta x^\mu(\lambda + \delta\lambda) - \delta x^\mu(\lambda)}{\delta\ell} \\
&= \frac{[f^\mu(\lambda + \delta\lambda, \delta\boldsymbol{y}) - f^\mu(\lambda + \delta\lambda, \boldsymbol{0})] - [f^\mu(\lambda, \delta\boldsymbol{y}) - f^\mu(\lambda, \boldsymbol{0})]}{\delta\ell} \; ,
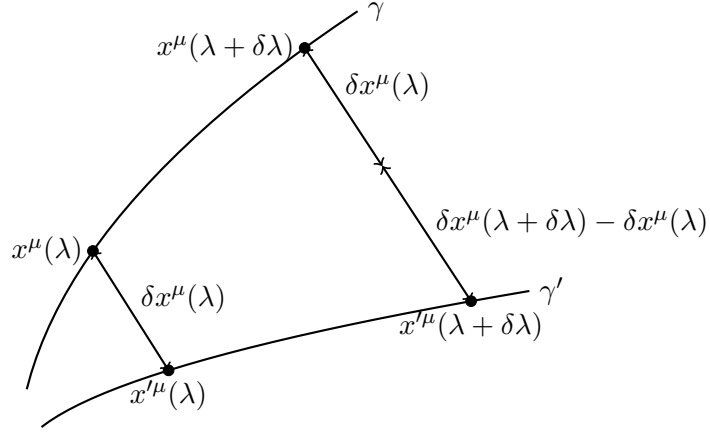\end{aligned}
\tag{3.51}
$$

FIGURE 3.3: This figure may be used to aid in the visualisation of the definition of $\delta\theta^\mu$.

where $\delta\ell$ is the infinitesimal distance along the geodesic in the rest-frame of the observer field:

$$
\begin{aligned}
\delta\ell &= |u_\mu dx^\mu| = |u_\mu[f^\mu(\lambda + \delta\lambda) - f^\mu(\lambda)]\delta\lambda| \\
&= |u_\mu \frac{\partial f^\mu}{\partial\lambda}\delta\lambda| = |u_\mu k^\mu|\delta\lambda = \omega\delta\lambda \ .
\end{aligned}
\tag{3.52}
$$

Using this to further simplify the expression for the angular deviation, we obtain

$$
\delta\theta^\mu = \frac{\delta x^\mu(\lambda + \delta\lambda) - \delta x^\mu(\lambda)}{\omega\delta\lambda} = \frac{1}{\omega}\frac{D\delta x^\mu}{d\lambda} = \frac{1}{\omega}\nabla_{\boldsymbol{k}}\delta x^\mu \ ,
\tag{3.53}
$$

where $\frac{D}{d\lambda} = k^\nu\nabla_\nu$ is the covariant derivative which takes into account the fact that the vector bases of γ and γ' change as one moves along the geodesics.

The vectors k^μ and δx^μ (see Fig. 3.3) form a 2-surface and in the resulting 2-surface elements we can choose coordinates (λ, y) such that $\boldsymbol{k} = \partial/\partial\lambda$ and $\delta\boldsymbol{x} = \partial/\partial y$. Then we have

$$
\begin{aligned}
\delta x^\mu_{,\nu}k^\nu - k^\mu_{,\nu}\delta x^\nu &= \frac{\partial\delta x^\mu}{\partial\lambda} - \frac{\partial k^\mu}{\partial y} \\
&= \frac{\partial^2 f^\mu}{\partial\lambda\partial y} - \frac{\partial^2 f^\mu}{\partial y\partial\lambda} = 0 \ .
\end{aligned}
\tag{3.54}
$$

We can show that the partial derivatives in (3.54) may be replaced with covariant derivatives:

$$
\begin{aligned}
\delta x^{\mu}_{;\nu} k^{\nu} - k^{\mu}_{;\nu} \delta x^{\nu} &= \left(\frac{\partial \delta x^{\mu}}{\partial \lambda} + \Gamma^{\mu}_{\alpha\nu} \delta x^{\alpha} k^{\nu} \right) - \left(\frac{\partial k^{\mu}}{\partial y} + \Gamma^{\mu}_{\nu\alpha} k^{\alpha} \delta x^{\nu} \right) \\
&= 0 \, ,
\end{aligned}
\tag{3.55}
$$

where we have used the result from (3.54).

Since this is a covariant tensor equation, it is independent of the choice of coordinate system and we have

$$
(\nabla_{\delta \boldsymbol{x}} k)^{\mu} = (\nabla_{\boldsymbol{k}} \delta x)^{\mu} \, ,
\tag{3.56}
$$

which recovers the result in [50].

3.3.2 Reparametrization

The rays that are emitted simultaneously in an infinitesimal beam would be observed simultaneously, i.e. in the rest-frame of the observer. Thus δx^{μ} must sweep out a surface normal to u^{μ}_{O}. This is not necessarily true given the current definitions. However, as shown in [49] and [50], it is possible to choose a parametrization where this is true. We rewrite the variables parametrizing the geodesics as follows:

$$
\hat{\lambda} \to \lambda + h(\boldsymbol{y}) \, , \; \hat{\boldsymbol{y}} \to \boldsymbol{g}(\boldsymbol{y}) \, ,
\tag{3.57}
$$

where the circumflex denotes the variables in the original parametrization. If we now consider the deviation vector $\delta \hat{x}^{\mu}$ in the original parametrization, we may expand its definition in terms of derivatives with respect to the variables in the new parametrization:

$$
\begin{aligned}
\delta \hat{x}^{\mu} = \frac{\partial f^{\alpha}}{\partial \hat{y}^{i}} \delta \hat{y}^{i} &= \left[\frac{\partial f^{\alpha}}{\partial \lambda} \frac{\partial \lambda}{\partial \hat{y}^{i}} + \frac{\partial f^{\alpha}}{\partial y^{j}} \frac{\partial y^{j}}{\partial \hat{y}^{i}} \right] \frac{\partial \hat{y}^{i}}{\partial y^{k}} \delta y^{k} \\
&= \left[k^{\alpha} \frac{\partial \lambda}{\partial y^{j}} \frac{\partial y^{j}}{\partial \hat{y}^{i}} + \frac{\partial f^{\alpha}}{\partial y^{j}} \frac{\partial y^{j}}{\partial \hat{y}^{i}} \right] \frac{\partial \hat{y}^{i}}{\partial y^{k}} \delta y^{k} \\
&= \left[k^{\alpha} \frac{\partial h}{\partial y^{j}} + \frac{\partial f^{\alpha}}{\partial y^{j}} \right] \delta^{j}_{k} \delta y^{k} \, .
\end{aligned}
\tag{3.58}
$$

Thus, using the definition of the deviation vector for the new parametrization, we have

$$\delta\hat{x}^{\mu} \quad \rightarrow \quad \delta x^{\mu} + k^{\mu}\delta h \ , \tag{3.59}$$

where $\delta h = \frac{\partial h}{\partial y^{j}}\delta y^{j}$.

In addition, for the metric we obtain

$$g_{\mu\nu}\delta\hat{x}^{\mu}\delta\hat{x}^{\nu} \quad \rightarrow \quad g_{\mu\nu}(\delta x^{\mu} + k^{\mu}\delta h)(\delta x^{\nu} + k^{\nu}\delta h) = g_{\mu\nu}\delta x^{\mu}\delta x^{\nu} \ , \tag{3.60}$$

where the invariance of the metric in the second equation above follows from (3.50) and the fact that k^{μ} is the tangent field of a null geodesic ($k^{\mu}k_{\mu} = 0$). Now, since an observer's four velocity u^{μ} must be time-like, we have $(k^{\mu}u_{\mu})(\lambda) \neq 0$, so it is possible to choose a parametrization with δh such that

$$\delta x^{\mu}u_{\mu} \rightarrow (\delta x^{\mu} + k^{\mu}\delta h)u_{\mu} = 0 \tag{3.61}$$

holds at a general point along the geodesic. In particular, this is true at the observer under the new parametrization:

$$\delta x_{O}^{\mu}u_{\mu}(\lambda_{O}) = 0 \ . \tag{3.62}$$

The same is true at the source, but for another reason: $\delta x^{\mu}(\lambda_{S}) = 0$ for rays originating from a single event. As for the angular deviation, $u_{\alpha}k^{\alpha} = -\omega$ gives

$$(\nabla_{\delta\boldsymbol{x}}u)_{\alpha}k^{\alpha} + u_{\alpha}(\nabla_{\delta\boldsymbol{x}}k)^{\alpha} = \delta x^{\mu}(\nabla_{\mu}u)_{\alpha}k^{\alpha} + u_{\alpha}(\nabla_{\delta\boldsymbol{x}}k)^{\alpha} = 0 \ . \tag{3.63}$$

Thus, at the source, $\delta x^{\mu} = 0$ and we have

$$[u_{\alpha}(\nabla_{\delta\boldsymbol{x}}k)^{\alpha}](\lambda_{S}) = 0 \ , \tag{3.64}$$

so that

$$\delta\theta_{S}^{\alpha}u_{\alpha}(\lambda_{S}) = 0 \ . \tag{3.65}$$

Furthermore, since k^α is null, we have

$$k_\alpha (\nabla_{\delta \boldsymbol{x}} k)^\alpha \;=\; \frac{1}{2} \nabla_{\delta \boldsymbol{x}} (k_\alpha k^\alpha) = 0 \;, \tag{3.66}$$

so that

$$k_\alpha \delta \theta^\alpha \;=\; 0 \;. \tag{3.67}$$

Thus, according to (3.50), (3.62), (3.65) and (3.67), the quantities δx_O^μ and $\delta \theta_S^\mu$ are normal, at the observer and the source respectively, to the 4-vectors k^μ, u^μ and (by (3.47)) to n^μ, the corresponding photon direction. The quantities δx_O^μ and $\delta \theta_S^\mu$ are thus defined in a 2-space (the "screen space"), which is normal to both the four-velocity and the photon direction.

We can project vectors onto the screen space defined at a point $x^\mu = f^\mu(\lambda, \boldsymbol{y})$ along a ray, using the projector as defined in [49]:

$$P_\nu^\mu = \delta_\nu^\mu + u^\mu u_\nu - n^\mu n_\nu \;. \tag{3.68}$$

3.3.3   Transport equation

Using the Ricci identity and following [49] and [50], we have

$$
\begin{aligned}
k^\mu \delta x^\nu R^\alpha_{\beta\mu\nu} k^\beta &= k^\mu \delta x^\nu (\nabla_\mu \nabla_\nu - \nabla_\nu \nabla_\mu) k^\alpha = \delta x^\nu \nabla_{\boldsymbol{k}} \nabla_\nu k^\alpha - k^\mu \nabla_{\delta \boldsymbol{x}} (\nabla_\mu k^\alpha) \\
&= \nabla_{\boldsymbol{k}} (\delta x^\nu \nabla_\nu k^\alpha) - (\nabla_{\boldsymbol{k}} \delta x^\nu)(\nabla_\nu k^\alpha) - \nabla_{\delta \boldsymbol{x}} (k^\mu \nabla_\nu k^\alpha) + (\nabla_{\delta \boldsymbol{x}} k^\mu)(\nabla_\mu k^\alpha) \\
&= \nabla_{\boldsymbol{k}} (\delta x^\nu \nabla_\nu k^\alpha) - (\nabla_{\boldsymbol{k}} \delta x^\nu)(\nabla_\nu k^\alpha) - \nabla_{\delta \boldsymbol{x}} (\nabla_{\boldsymbol{k}} k^\alpha) + (\nabla_{\boldsymbol{k}} \delta x^\mu)(\nabla_\mu k^\alpha) \\
&= \nabla_{\boldsymbol{k}} (\delta x^\nu \nabla_\nu k^\alpha) = \nabla_{\boldsymbol{k}} (\omega \delta \theta^\alpha) \;,
\end{aligned}
\tag{3.69}
$$

where in the third equality the product rule has been used and in the fourth and fifth equalities the result from (3.56) was used, along with the fact that $\boldsymbol{k}$ is tangent to the geodesic (i.e. $\nabla_{\boldsymbol{k}} k^\alpha = 0$). The final equality uses the definition of $\delta \theta^\mu$, (3.53). Thus, we have a system of linear equations:

$$\nabla_{\boldsymbol{k}} \delta x^\alpha \;=\; \omega \delta \theta^\alpha \;, \tag{3.70}$$

$$\nabla_{\boldsymbol{k}} \omega (\delta \theta^\alpha) \;=\; R^\alpha_{\beta\mu\nu} k^\beta k^\mu \delta x^\nu \;, \tag{3.71}$$

or, more explicitly:

$$\frac{d(\delta x^\alpha)}{d\lambda} = -\Gamma^\alpha_{\mu\nu}k^\mu \delta x^\nu + \omega\delta\theta^\alpha \tag{3.72}$$

$$\equiv C^\alpha_\nu \delta x^\nu + \omega\delta\theta^\alpha \ , \tag{3.73}$$

$$\frac{d(\omega\delta\theta^\alpha)}{d\lambda} = R^\alpha_{\beta\mu\nu}k^\beta k^\mu \delta x^\nu - \Gamma^\alpha_{\mu\nu}k^\mu \omega\delta\theta^\nu \tag{3.74}$$

$$\equiv A^\alpha_\nu \delta x^\nu + C^\alpha_\nu \omega\delta\theta^\nu \ , \tag{3.75}$$

where, as in [49], we have defined:

$$C^\alpha_\beta = -\Gamma^\alpha_{\mu\beta}k^\mu \ , \tag{3.76}$$

$$A^\alpha_\beta = R^\alpha_{\mu\nu\beta}k^\mu k^\nu \ . \tag{3.77}$$

We can rewrite the system of equations in vector notation, following [49]:

$$\boldsymbol{Z} = \begin{pmatrix} \delta\boldsymbol{x} \\ \omega\delta\boldsymbol{\theta} \end{pmatrix} \ , \tag{3.78}$$

to summarise the equations as

$$\frac{d\boldsymbol{Z}(\lambda)}{d\lambda} = B(\lambda)\boldsymbol{Z}(\lambda) \ , \tag{3.79}$$

where

$$B(\lambda) = \begin{pmatrix} C^\alpha_\beta(\lambda) & \delta^\alpha_\beta \\ A^\alpha_\beta(\lambda) & C^\alpha_\beta(\lambda) \end{pmatrix} \ . \tag{3.80}$$

The initial conditions of this system of equations are as follows:

- The coordinate deviation between rays is initially zero, since they originate from the same event:

$$\delta x^\alpha(\lambda_S) = 0 \ . \tag{3.81}$$

- The angular deviation at the source is normal to the source velocity, [see (3.65)]

$$(\delta\theta^\alpha u_\alpha)(\lambda_S) = 0 \ . \tag{3.82}$$

Since (3.79) is linear, it implies that there exists a linear mapping between the initial values (at the source) and the general solution, which we call the Jacobi mapping.

Thus,

$$\delta x^\mu(\lambda) = \mathcal{J}^\mu_\alpha(\lambda)\delta\theta^\alpha_S \ , \tag{3.83}$$

where we have used $\delta x^\alpha_S = 0$.

In particular, we are interested in the value of δx^μ at the observer, so we consider

$$\delta x^\mu_O = \mathcal{J}^\mu_\alpha(\lambda_O)\delta\theta^\alpha_S \ . \tag{3.84}$$

Since δx^μ and $\delta\theta^\mu$ are both in the screen space, they are equal to their projections. Thus, multiplying on both sides by $(P_O)^\nu_\mu$ and expanding $\delta\theta^\alpha_S$ as a projection of itself, we obtain

$$\delta x^\nu_O = J^\nu_\beta(O,S)\delta\theta^\beta_S \ , \tag{3.85}$$

where

$$J^\nu_\beta(O,S) = (P_O)^\nu_\mu \mathcal{J}^\mu_\alpha(\lambda_O)(P_S)^\alpha_\beta \tag{3.86}$$

is the true, two dimensional Jacobi mapping in the screen space.

Now, if we examine the geometry of Fig. 3.2, we see that the infinitesimal beam area at the observer may be computed as the product of two deviation vectors that span the screen space:

$$\mathrm{d}A_O = \varepsilon_{AB}\delta x^A_1(\lambda_O)\delta x^B_2(\lambda_O) \ , \tag{3.87}$$

where ε is the Levi-Civita symbol.

Thus

$$\begin{aligned} \mathrm{d}A_O &= \varepsilon_{AB}J^A_C J^B_D \delta\theta^C_1 \delta\theta^D_2 = |\det J|\, \varepsilon_{CD}\, \delta\theta^C_1 \delta\theta^D_2 \\ &= |\det J|\, \mathrm{d}\Omega_S \ . \end{aligned} \tag{3.88}$$

This recovers the result of [49] and [50]:

$$\frac{dA_O}{d\Omega_S} = |\det J| \ . \tag{3.89}$$

which means that the luminosity distance, given by (3.45), is related to the Jacobi map as follows:

$$d_{\mathrm{L}}^2(S, O) = (1 + z)^2 |\det J| . \tag{3.90}$$

3.3.4 Introducing a conformal factor

When applying the above formalism to a FLRW universe, it is useful to rewrite the metric in such a way that the scale factor is removed as a conformal factor, i.e. using the conformal definition of time. In this section, we derive the relations between important quantities in the original and modified metrics, following the derivations set out in [49]. Consider a new metric $g_{\mu\nu}$ defined by

$$\mathrm{d}\hat{s}^2 = \hat{g}_{\mu\nu}\mathrm{d}x^\mu\mathrm{d}x^\nu = a^2 g_{\mu\nu}\mathrm{d}x^\mu\mathrm{d}x^\nu = a^2\mathrm{d}s^2 . \tag{3.91}$$

For a light-like geodesic in $\mathrm{d}\hat{s}^2$ with affine parameter $\hat{\lambda}$ and tangent vector $\hat{k}$, we have

$$\frac{\mathrm{d}\hat{\lambda}}{\mathrm{d}\lambda} = a^2 . \tag{3.92}$$

and

$$\hat{k}^\mu = \frac{\mathrm{d}x^\mu}{\mathrm{d}\hat{\lambda}} = \frac{k^\mu}{a^2} ; \tag{3.93}$$

Then, suppose $\hat{u}^\mu = \frac{\mathrm{d}x^\mu}{\mathrm{d}\hat{\tau}}$ is the 4-velocity (such that $\hat{g}_{\mu\nu}\hat{u}^\mu\hat{u}^\nu = -1$) for an observer and with respect to the metric $\mathrm{d}\hat{s}$, with proper time $\hat{\tau}$. The corresponding 4-velocity of the observer with respect to the metric $\mathrm{d}s^2$ is then $u^\mu = \frac{\mathrm{d}x^\mu}{\mathrm{d}\tau}$, where the new proper time τ is related to the original by $\frac{\mathrm{d}\hat{\tau}}{\mathrm{d}\tau} = a$, since

$$\mathrm{d}\hat{\tau}^2 = -\mathrm{d}\hat{s}^2|_{flow\ line} = a^2\mathrm{d}s^2|_{flow\ line} = a^2\mathrm{d}\tau^2 . \tag{3.94}$$

So, the 4-velocities are related by

$$\hat{u}^\mu = \frac{dx^\mu}{d\hat{\tau}} = \frac{1}{a}u^\mu . \tag{3.95}$$

The redshifts may also be related:

$$1 + \hat{z} = \frac{\hat{\omega}_S}{\hat{\omega}_O} = \frac{(\hat{g}_{\mu\nu}\hat{k}^\mu\hat{u}^\nu)_S}{(\hat{g}_{\mu\nu}\hat{k}^\mu\hat{u}^\nu)_O} = \frac{a_O(g_{\mu\nu}k^\mu u^\nu)_S}{a_S(g_{\mu\nu}k^\mu u^\nu)_O} = \frac{a_O}{a_S}(1 + z) . \tag{3.96}$$

Under conformal transformations, only distances (and not angles) are affected, picking up the conformal factor. Hence, the Jacobi maps in the two metrics and their determinants may be related by

$$\hat{J}^\alpha_\beta(O,S) = \frac{\delta \hat{x}^\alpha_O}{\delta \theta^\beta_S} = a_O \frac{\delta x^\alpha_O}{\delta \theta^\beta_S} = a_O J^\alpha_\beta(O,S) \,, \tag{3.97}$$

$$\det \hat{J}(O,S) = a_O^2 \det J(O,S) \,. \tag{3.98}$$

Finally, the relationship between luminosity distances is given by

$$\hat{d}_L = (1 + \hat{z})\sqrt{|\det \hat{J}(O,S)|} = \frac{a_O^2}{a_S} d_{\mathrm{L}} \,. \tag{3.99}$$

3.3.5   Application to perturbed FLRW universe

We now apply the definition of the luminosity distance to a perturbed Friedmann universe. As before, we consider only scalar perturbations and in the Newtonian gauge the metric is

$$\tilde{g}_{\mu\nu} dx^\mu dx^\nu = a^2[-(1 + 2\Phi)d\eta^2 + (1 - 2\Psi)\gamma_{ij} dx^i dx^j] \,. \tag{3.100}$$

Further, we include our assumptions of no anisotropic stress (i.e. $\Psi = \Phi$), and a spatially flat universe ($K = 0 \Rightarrow \gamma_{ij} = \delta_{ij}$). Thus the conformal metric becomes

$$ds^2 = -(1 + 2\Phi)d\eta^2 + (1 - 2\Phi)\delta_{ij} dx^i dx^j \,, \tag{3.101}$$

by (3.91). We will eventually use (3.99) to relate the calculated luminosity distance to the one in the full, expanding Friedmann universe.

By (1.59) with a=1, the 4-velocity of the observer and source in the spacetime (3.101) are both given by

$$u^\mu = (1 - \Phi, v^i) \,, \tag{3.102}$$

assuming that they are both moving with the cosmic fluid, where v^i is the peculiar velocity field.

We also require the 4-vector k^μ for the photon. This can be obtained by integrating the null geodesic equation for (3.101), which has a Minkowski background. In the Minkowski background $\mathcal{H} = 0$ and we can choose the normalization of the affine parameter in such a

way that $\bar{k}^0 = 1$ and $\bar{k}^i = -n^i$, with $n_i n^i = 1$. Thus, $\bar{k}^\alpha = (1, -n^i)$. We assume that the perturbed value of the photon four-velocity at the observer is equal to the background ($k_O^0 = 1$). In addition to our definition of $\boldsymbol{n}$, this is another difference to the convention adopted in [49], where it is assumed that the perturbed value of the photon four-velocity at the *source* is equal to the background.

The geodesic equation gives

$$\frac{\mathrm{d}k^\mu}{\mathrm{d}\lambda} = -\Gamma^\mu_{\alpha\beta} k^\alpha k^\beta = -\delta\Gamma^\mu_{\alpha\beta} \bar{k}^\alpha \bar{k}^\beta , \tag{3.103}$$

where the second equality follows since $\mathcal{H} = 0 \Rightarrow \bar{\Gamma}^\mu_{\alpha\beta} = 0$.

Thus, using (1.53) with $\mathcal{H} = 0$, we find that

$$\frac{\mathrm{d}k^0}{\mathrm{d}\lambda} = 2n^i \partial_i \Phi , \tag{3.104}$$

and

$$\frac{\mathrm{d}k^i}{\mathrm{d}\lambda} = -2\partial^i \Phi - 2n^i(\Phi' - n^i \partial_i \Phi) . \tag{3.105}$$

By (3.47), we have

$$n^i \partial_i \Phi = \Phi' - \frac{\mathrm{d}\Phi}{\mathrm{d}\lambda} . \tag{3.106}$$

Thus, integrating (3.104) and (3.105) and using (3.106), we obtain:

$$
\begin{aligned}
k^0(\lambda_S) - k^0(\lambda_O) &= 2\int_{\lambda_O}^{\lambda_S} d\lambda (n^i \partial_i \Phi) \\
&= -2(\Phi_S - \Phi_O) + 2\int_{\lambda_O}^{\lambda_S} d\lambda \Phi' , \tag{3.107}
\end{aligned}
$$

$$
k^i(\lambda_S) - k^i(\lambda_O) = -2n^i(\Phi_S - \Phi_O) - 2\int_{\lambda_O}^{\lambda_S} d\lambda \partial^i \Phi , \tag{3.108}
$$

which recovers the result stated in [49] (apart from the difference in definition of $\boldsymbol{n}$ and assumptions about the source/observer 4-velocity).

We may consider the perturbation of the background 4-vector:

$$k_X^\mu = \bar{k}_X^\mu + \delta k_X^\mu , \tag{3.109}$$

where $(\delta)k_X^\mu = (\delta)k^\mu(\lambda_X)$ and $\delta k_O^0 = 0$ if we assume that the photon four-velocity at the observer is equal to the background. This leads to:

$$\delta k_S^0 \;\equiv\; \delta k^0 = -2(\Phi_S - \Phi_O) + 2\int_{\lambda_O}^{\lambda_S} d\lambda \Phi' \,, \qquad (3.110)$$

$$k_S^i - k_O^i = \delta k_S^i - \delta k_O^i \;\equiv\; \delta k^i = -2n^i(\Phi_S - \Phi_O) - 2\int_{\lambda_O}^{\lambda_S} d\lambda \partial^i\Phi \,, \qquad (3.111)$$

3.4 Redshift perturbation

The redshift in perturbed Minkowski space may then be determined:

$$
\begin{aligned}
1 + z \;&=\; \frac{\omega_S}{\omega_O} = \frac{(g_{\mu\nu}k^\mu u^\nu)_S}{(g_{\mu\nu}k^\mu u^\nu)_O} && (3.112)\\
&=\; \frac{-(1+2\Phi_S)\left[1 - 2\Phi\big|_O^S + 2\int_{\lambda_O}^{\lambda_S} d\lambda \Phi'\right](1-\Phi_S) + (1-2\Phi_S)\bar{k}_S^i v_{iS}}{-(1+2\Phi_O)(1-\Phi_O) + (1-2\Phi_O)\bar{k}_O^i v_{iO}} \,,
\end{aligned}
$$

using the zeroth component of the geodesic equation (3.107). Together with the ith component (3.108) this gives, to first order:

$$
\begin{aligned}
1 + z \;&=\; 1 + \Phi_S - \Phi_O - 2(\Phi_S - \Phi_O) + 2\int_{\lambda_O}^{\lambda_S} d\lambda \Phi' - v_i\bar{k}^i\big|_O^S \\
&=\; 1 - [\Phi - \boldsymbol{v}\cdot\boldsymbol{n}]_O^S + 2\int_{\lambda_O}^{\lambda_S} d\lambda \Phi'(\lambda) \,, && (3.113)
\end{aligned}
$$

consistent with [18, 49] (apart from the difference in convention for $\boldsymbol{n}$). In a Friedmann universe we have (from (3.96), dropping the tilde on z)

$$1 + z \;=\; \frac{1}{a}\left[1 - [\Phi - \boldsymbol{v}\cdot\boldsymbol{n}]_O^S + 2\int_{\lambda_O}^{\lambda_S} d\lambda \Phi'(\lambda)\right] \,. \qquad (3.114)$$

We can take $\Phi_O = 0 = v_O$, since these quantities cannot be predicted by perturbation theory [18].

Hence, the perturbation in redshift is

$$\delta z = z - \bar{z} = -\frac{1}{a}\left(\Phi - \boldsymbol{v}\cdot\boldsymbol{n}\right) + \frac{2}{a}\int_0^\lambda d\tilde{\lambda}\,\Phi'(\tilde{\lambda}) \,, \qquad (3.115)$$

where $1 + \bar{z} = 1/a$ is the usual background redshift and where $\lambda_S = \lambda$ and $\lambda_O = 0$ are the values of the affine parameter corresponding to the initial photon position and

observer position respectively, according to our definition with $\boldsymbol{n}$ pointing towards the photon's initial position.

Thus, the redshift correction in (3.16) becomes

$$\frac{\partial \bar{\rho}_g}{\partial \bar{z}} \frac{\delta z(\boldsymbol{n}, z)}{\bar{\rho}_g(\bar{z})} = \frac{1}{\bar{\rho}_g(\bar{z})} \frac{\partial \bar{\rho}_g}{\partial \bar{z}} \left[-\frac{1}{a} \left(\Phi - \boldsymbol{v} \cdot \boldsymbol{n} \right) + \frac{2}{a} \int_0^\lambda \mathrm{d}\tilde{\lambda} \Phi'(\tilde{\lambda}) \right] . \tag{3.116}$$

3.4.1 Evolution bias

The number of sources is not a conserved quantity. Galaxies are able to form and merge and as a result their number density must be allowed to change. The evolution bias is a quantity which describes the intrinsic change in the number of sources with time (or redshift). Hence the proper number density obeys a modified continuity equation:

$$\bar{\rho}_g' + 3\mathcal{H}\bar{\rho}_g = b_e \mathcal{H}\bar{\rho}_g , \tag{3.117}$$

where the evolution bias b_e vanishes if the source number is conserved, i.e. if $(a^3 \bar{\rho}_g)' = 0$. As stated, the number of sources will evolve with redshift, in general. The evolution bias is determined if we know $\bar{\rho}_g(z)$:

$$b_e = \frac{1}{\mathcal{H}} \frac{(a^3 \bar{\rho}_g)'}{(a^3 \bar{\rho}_g)} = \frac{\partial \ln (a^3 \bar{\rho}_g)}{\partial \ln a} = \frac{1}{a} \frac{\partial (a^3 \bar{\rho}_g)}{\partial a} \frac{1}{a^3 \bar{\rho}_g} = -\frac{1}{a\bar{\rho}_g} \frac{\partial \bar{\rho}_g}{\partial \bar{z}} + 3 . \tag{3.118}$$

Hence, the redshift correction (3.116) is

$$\frac{\partial \bar{\rho}_g}{\partial \bar{z}} \frac{\delta z(\boldsymbol{n}, z)}{\bar{\rho}_g(\bar{z})} = -(b_e - 3) \left[-\Phi + \boldsymbol{v} \cdot \boldsymbol{n} + 2 \int_0^\lambda \mathrm{d}\tilde{\lambda} \Phi'(\tilde{\lambda}) \right] . \tag{3.119}$$

3.5 Volume perturbation

Recall the perturbed FLRW metric:

$$\tilde{g}_{\mu\nu} dx^\mu dx^\nu = a^2 [-(1 + 2\Phi)d\eta^2 + (1 - 2\Phi)\gamma_{ij} dx^i dx^j] , \tag{3.120}$$

and the four-velocity of a source (dropping the tilde on u):

$$u^\mu = \frac{1}{a}(1 - \Phi, v^i) . \tag{3.121}$$

Consider a small element of volume dV as measured in the rest-frame of the source [18, 62]:

$$dV = \sqrt{-g}\,\epsilon_{\mu\alpha\beta\gamma}u^\mu dx^\alpha dx^\beta dx^\gamma \;, \tag{3.122}$$

where $\epsilon_{\mu\alpha\beta\gamma}$ is the Levi-Civita symbol [2] and g is the determinant of the metric. To first order we have

$$\sqrt{-g} = a^4(1 - 2\Phi) \;. \tag{3.123}$$

Measurements are made from the rest-frame of the observer, so we must perform a coordinate transformation between the coordinates at the source and those at the observer [18, 62]:

$$dV = \sqrt{-g}\,\epsilon_{\mu\alpha\beta\gamma}u^\mu \frac{\partial x^\alpha}{\partial z}\frac{\partial x^\beta}{\partial\theta_{\rm O}}\frac{\partial x^\gamma}{\partial\phi_{\rm O}}\mathcal{J}\,dz d\theta_{\rm O} d\phi_{\rm O} \;, \tag{3.124}$$

where z is the observed redshift and the Jacobian of the mapping is

$$\mathcal{J} = \left|\frac{\partial\,(\theta_{\rm S},\phi_{\rm S})}{\partial\,(\theta_{\rm O},\phi_{\rm O})}\right| \;. \tag{3.125}$$

Here the spherical polar angles $(\theta_{\rm S},\phi_{\rm S})$ and $(\theta_{\rm O},\phi_{\rm O})$ are the angular coordinates measured from the respective positions of the source and observer. If χ is the radial comoving distance to dV, then in spherical coordinates the infinitesimal length element is given as $dx^\mu = (-d\eta, d\chi, \chi d\theta_{\rm S}, \chi\sin\theta_{\rm S}d\phi_{\rm S})$. In a perturbed universe, both the radial and angular coordinates are perturbed with respect to the background observer and therefore we have, at first order:

$$\theta_{\rm S} = \theta_{\rm O} + \delta\theta \;, \qquad \phi_{\rm S} = \phi_{\rm O} + \delta\phi \;, \qquad \chi = \bar\chi + \delta\chi \;. \tag{3.126}$$

Thus, to first order, the Jacobian (3.125) is given by

$$\mathcal{J} = 1 + \frac{\partial\delta\theta}{\partial\theta} + \frac{\partial\delta\phi}{\partial\phi} \;. \tag{3.127}$$

We can define a density $\mathcal{V}$ such that [18]:

$$dV = \mathcal{V}\,dz d\theta_{\rm O} d\phi_{\rm O} \;, \tag{3.128}$$

and thus

$$\frac{\delta V}{\bar V} = \frac{\mathcal{V} - \bar{\mathcal{V}}}{\bar{\mathcal{V}}} \;. \tag{3.129}$$

In the background limit, this quantity simplifies to

$$\frac{a^4}{\mathcal{H}}\bar{\chi}^2 sin\theta_{\rm O} \; , \tag{3.130}$$

which follows from (3.5), using $\mathrm{d}\Omega = \sin\theta \mathrm{d}\theta \mathrm{d}\phi$. Hereafter we suppress the overbars on χ and take it to mean the background comoving distance.

A lengthy calculation (see Appendix B and [18]) leads to

$$
\begin{aligned}
\frac{\delta V(z,\boldsymbol{n})}{\bar{V}(z)} &= -4\Phi + 4\boldsymbol{v}\cdot\boldsymbol{n} + \frac{1}{\mathcal{H}}\left[\frac{\partial}{\partial\lambda}\left(\boldsymbol{v}\cdot\boldsymbol{n}\right) + \Phi' + n^i\partial_i\Phi\right]\\
&\quad + \left(\frac{\mathcal{H}'}{\mathcal{H}^2} + \frac{2}{\bar{\chi}\mathcal{H}}\right)\left[\Phi - \boldsymbol{v}\cdot\boldsymbol{n} - 2\int_0^\lambda \mathrm{d}\tilde{\lambda}\Phi'\right]\\
&\quad - \frac{4}{\bar{\chi}}\int_0^\lambda \mathrm{d}\tilde{\lambda}\Phi + 6\int_0^\lambda \mathrm{d}\tilde{\lambda}\Phi' - 2\int_0^\lambda \mathrm{d}\tilde{\lambda}\frac{\chi-\tilde{\chi}}{\chi\tilde{\chi}}\tilde{\nabla}_\Omega^2\Phi \; ,
\end{aligned}
\tag{3.131}
$$

where $\tilde{\nabla}_\Omega^2 = \cot\theta_{\rm O}\partial_{\theta_{\rm O}} + \partial_{\theta_{\rm O}}^2 + \left(1/\sin^2\theta_{\rm O}\right)\partial_{\phi_{\rm O}}^2$ is the angular part of the Laplacian operator. We can substitute (3.131) in (3.22) to show that the fluctuation in the observed galaxy number count at first order is given by,

$$
\begin{aligned}
\Delta(\boldsymbol{n},z) &= \underbrace{b\delta_{\rm C}}_{\text{Density term}} + \underbrace{\mathcal{H}(b_e - 3)V}_{\text{GR bias correction}} + \frac{1}{\mathcal{H}}\frac{\partial}{\partial\lambda}\left(\boldsymbol{v}\cdot\boldsymbol{n}\right) - \frac{1}{\mathcal{H}}\boldsymbol{v}'\cdot\boldsymbol{n} + \underbrace{\left(b_e - \frac{\mathcal{H}'}{\mathcal{H}^2} - \frac{2}{\chi\mathcal{H}}\right)(\boldsymbol{v}\cdot\boldsymbol{n})}_{\text{Doppler}}\\
&\quad - \underbrace{\left(b_e - \frac{\mathcal{H}'}{\mathcal{H}^2} - \frac{2}{\chi\mathcal{H}}\right)\Phi - \Phi + \frac{1}{\mathcal{H}}\Phi'}_{\text{Sachs-Wolfe}} + 2\underbrace{\left(b_e - \frac{\mathcal{H}'}{\mathcal{H}^2} - \frac{2}{\chi\mathcal{H}}\right)\int_0^\lambda \mathrm{d}\tilde{\lambda}\Phi'}_{\text{Integrated Sachs-Wolfe}}\\
&\quad - \underbrace{\frac{4}{\chi}\int_0^\lambda \mathrm{d}\tilde{\lambda}\Phi}_{\text{Time-delay(Shapiro)}} + 2\underbrace{\int_0^\lambda \mathrm{d}\tilde{\lambda}\frac{\chi-\tilde{\chi}}{\chi\tilde{\chi}}\tilde{\nabla}_\Omega^2\Phi}_{\text{Lensing}} \; ,
\end{aligned}
\tag{3.132}
$$

where we have made use of the Euler equation (see (1.72)) for pressureless matter:

$$\boldsymbol{v}'\cdot\boldsymbol{n} + \mathcal{H}\boldsymbol{v}\cdot\boldsymbol{n} + n^i\partial_i\Phi = 0 \; . \tag{3.133}$$

The result of (3.132) shows the observed fluctuation in galaxy number counts, with contributions from redshift and volume perturbations. However, it is not yet representative of actual observations. Every survey has a limit to its flux sensitivity and so there will be a threshold flux below which objects will be not detected by the telescope. Thus the number of observed sources also depends on their apparent fluxes [63]. This effect,

called a magnification bias (mb), leads to an additional correction of the form [62]:

$$\Delta_{mb} = 5s\kappa_{\mathrm{GR}} \tag{3.134}$$

where κ is the lensing convergence and s is the effective slope of the number counts at the flux limit. This correction is based on the magnification or demagnification of the observed sources due of lensing by overdense or underdense regions between the observer and sources, which changes their apparent size and luminosity [62]. The lensing convergence takes into account the amplification or de-amplification of their fluxes and takes the form:

$$\kappa_{\mathrm{GR}} = \kappa + \text{relativistic corrections} , \tag{3.135}$$

with

$$\kappa = \int_0^\lambda \mathrm{d}\tilde{\lambda} \, \frac{\chi - \tilde{\chi}}{\chi\tilde{\chi}} \, \tilde{\nabla}_\Omega^2 \Phi , \tag{3.136}$$

where κ is the standard lensing term and the lensing term of (3.132) is -2κ. The relativistic corrections are other terms which contribute to corrections in the Doppler, Sachs-Wolfe, integrated Sachs-Wolfe and time-delay (Shapiro effect) terms [62]. They may be determined by solving the Sachs equation (see Section 3.3.3 for the equivalent transport equation) in a perturbed Friedmann universe, and the full relativistic expression for the correction due to the magnification bias is [62]

$$
\begin{aligned}
\Delta_{mb}(z, \boldsymbol{n}) \;=\; & -5s \int_0^\lambda \mathrm{d}\tilde{\lambda} \frac{\chi - \tilde{\chi}}{\chi\tilde{\chi}} \tilde{\nabla}_\Omega^2 \Phi + 5s\left(\frac{1}{\chi\mathcal{H}} - 1\right)(\boldsymbol{v}\cdot\boldsymbol{n}) \\
& + \frac{10s}{\chi} \int_0^\lambda \mathrm{d}\tilde{\lambda}\Phi - 10s\left(1 - \frac{1}{\chi\mathcal{H}}\right)\int_0^\lambda \mathrm{d}\tilde{\lambda}\Phi' \\
& + 5s\left(2 - \frac{1}{\chi\mathcal{H}}\right)\Phi ,
\end{aligned} \tag{3.137}
$$

where s is the magnification bias

$$s = \left.\frac{\partial a^3 \bar{\rho}_g}{\partial m}\right|_{m=m_*} , \tag{3.138}$$

where m_* is the threshold magnitude.

Adding the result of (3.137) to (3.132) we obtain

$$
\begin{aligned}
\Delta(\boldsymbol{n}, z) = {} & \underbrace{b_1 \delta_{\mathrm{C}}}_{\text{Density term}} + \underbrace{\mathcal{H}(b_e - 3)V}_{\text{GR bias correction}} \\
& + \frac{1}{\mathcal{H}} \left(\frac{\partial}{\partial \lambda} (\boldsymbol{v} \cdot \boldsymbol{n}) - \boldsymbol{v'} \cdot \boldsymbol{n} \right) + \underbrace{\left[b_e - \frac{\mathcal{H}'}{\mathcal{H}^2} - 5s + \frac{(5s-2)}{\chi \mathcal{H}} \right] (\boldsymbol{v} \cdot \boldsymbol{n})}_{\text{Doppler}} \\
& - \underbrace{\left[b_e - \frac{\mathcal{H}'}{\mathcal{H}^2} - 5s + \frac{(5s-2)}{\chi \mathcal{H}} \right] \Phi - (1-5s)\Phi + \frac{1}{\mathcal{H}} \Phi'}_{\text{Sachs}-\text{Wolfe}} \\
& - \underbrace{2 \left[b_e - \frac{\mathcal{H}'}{\mathcal{H}^2} - 5s + \frac{(5s-2)}{\chi \mathcal{H}} \right] \int_0^\lambda \mathrm{d}\tilde{\lambda} \Phi'}_{\text{Integrated Sachs}-\text{Wolfe}} - \underbrace{2 \frac{(5s-2)}{\chi} \int_0^\lambda \mathrm{d}\tilde{\lambda} \Phi}_{\text{Time}-\text{delay(Shapiro)}} \\
& - \underbrace{(5s-2) \int_0^\lambda \mathrm{d}\tilde{\lambda} \frac{\chi - \tilde{\chi}}{\chi \tilde{\chi}} \tilde{\nabla}_\Omega^2 (\Phi)}_{\text{Lensing}} .
\end{aligned}
\tag{3.139}
$$

The third term on the right-hand side is simplified to the contribution from RSD using the following relation (see (3.47)):

$$
\frac{\partial}{\partial \lambda} (\boldsymbol{v} \cdot \boldsymbol{n}) = \frac{\partial}{\partial \eta} (\boldsymbol{v} \cdot \boldsymbol{n}) - \frac{\partial}{\partial \chi} (\boldsymbol{v} \cdot \boldsymbol{n}) = \boldsymbol{v'} \cdot \boldsymbol{n} - \frac{\partial}{\partial \chi} (\boldsymbol{v} \cdot \boldsymbol{n}) ,
\tag{3.140}
$$

where $\frac{\partial}{\partial \chi} = n_i \partial^i$.

Therefore (3.139) becomes [32]

$$
\begin{aligned}
\Delta(\boldsymbol{n}, z) = {} & \underbrace{b \delta_{\mathrm{C}}}_{\text{Density term}} + \underbrace{\mathcal{H}(b_e - 3)V}_{\text{GR bias correction}} \\
& - \underbrace{\frac{1}{\mathcal{H}} \frac{\partial}{\partial \chi} (\boldsymbol{v} \cdot \boldsymbol{n})}_{\text{Redshift space distortion}} - \underbrace{\left[b_e - \frac{\mathcal{H}'}{\mathcal{H}^2} - 5s + \frac{(5s-2)}{\chi \mathcal{H}} \right] (\boldsymbol{v} \cdot \boldsymbol{n})}_{\text{Doppler}} \\
& - \underbrace{\left[b_e - \frac{\mathcal{H}'}{\mathcal{H}^2} - 5s + \frac{(5s-2)}{\chi \mathcal{H}} \right] \Phi - (1-5s)\Phi + \frac{1}{\mathcal{H}} \Phi'}_{\text{Sachs}-\text{Wolfe}} \\
& - \underbrace{2 \left[b_e - \frac{\mathcal{H}'}{\mathcal{H}^2} - 5s + \frac{(5s-2)}{\chi \mathcal{H}} \right] \int_0^\lambda \mathrm{d}\tilde{\lambda} \Phi'}_{\text{Integrated Sachs}-\text{Wolfe}} - \underbrace{2 \frac{(5s-2)}{\chi} \int_0^\lambda \mathrm{d}\tilde{\lambda} \Phi}_{\text{Time}-\text{delay(Shapiro)}} \\
& - \underbrace{(5s-2) \int_0^\lambda \mathrm{d}\tilde{\lambda} \frac{\chi - \tilde{\chi}}{\chi \tilde{\chi}} \tilde{\nabla}_\Omega^2 (\Phi)}_{\text{Lensing}} .
\end{aligned}
\tag{3.141}
$$

For brevity we can write (3.141) as follows:

$$\Delta(\boldsymbol{n}, z) = \Delta^\delta + \Delta^{GRbias} + \Delta^{\mathrm{RSD}} + \Delta^{\mathrm{Dop.}} + \Delta^{\mathrm{pot.}} + \Delta^\kappa , \qquad (3.142)$$

where $\Delta^\delta + \Delta^{GRbias}$ is the galaxy density term with the gauge transformation, Δ^{RSD} is the redshift space distortion term, $\Delta^{\mathrm{Dop.}}$ is the Doppler term, $\Delta^{\mathrm{pot.}}$ are the potential terms (non-integrated and integrated terms) and Δ^κ is the lensing term. Each of these terms may be expanded in spherical harmonics similarly to the density and redshift-space distortion terms dealt with earlier. These contributions are determined numerically using the code CAMB [45], taking into account the redshift distributions, window functions and other specifics for different kinds of survey. Until now we have only discussed surveys counting galaxies. There are other means by which we can gain information about the distribution of dark matter and some of these are discussed in the following sections.

3.6 HI intensity mapping

Emission of the 21cm line from neutral Hydrogen (HI) may also be used as a tracer of the underlying dark matter distribution. The overall approach is similar to that of galaxy number counts, but there are some important differences. Firstly, HI intensity mapping detects the total signal in each pixel, without detecting individual HI galaxies. In this case the quantity of interest is the number density of neutral Hydrogen atoms n_{HI}. Once again, a bias may be introduced to relate this to the underlying δ_m, using

$$\delta_{nC}(\boldsymbol{x}, \eta) = b_{\mathrm{HI}}(\eta)\delta_{mC}(\boldsymbol{x}, \eta) , \qquad (3.143)$$

where δ_{nC} is the perturbation in the number density of neutral Hydrogen (HI) atoms in the comoving gauge (C). In the Poisson gauge, similarly to galaxy number counts, the HI number density is

$$\delta_n = b_{\mathrm{HI}}\delta_{mC} + (b_e^{\mathrm{HI}} - 3)\mathcal{H}V . \qquad (3.144)$$

The expression for the evolution bias of a general tracer A is given by

$$b_e^{\mathrm{A}}(z) = -\frac{\partial \ln(a^3 \bar{\rho}_A)}{\partial \ln(1+z)} , \qquad (3.145)$$

where $a^3\bar{\rho}_A$ is the comoving background source number density for tracer A. The relationship between the background comoving number density of neutral Hydrogen atoms and the background brightness temperature, measured in an intensity mapping survey T_{HI}, is [59]

$$a^3\bar{\rho}_{\mathrm{HI}} \propto \frac{\bar{T}^{\mathrm{HI}}(z)H(z)}{(1+z)^2} \,, \tag{3.146}$$

which gives

$$(b_e)_{\mathrm{IM}}^{\mathrm{HI}} = \frac{\partial \ln\left(\bar{T}^{\mathrm{HI}}\mathcal{H}\right)}{\partial \ln a} - 3 \,. \tag{3.147}$$

If we define the perturbation in brightness temperature Δ_T analogous to the galaxy number count perturbation Δ_g, then it takes a similar form, related to the latter by [59]

$$\Delta_T(\boldsymbol{n}, z) = \Delta_g(\boldsymbol{n}, z) - 2\frac{\delta d_{\mathrm{L}}(\boldsymbol{n}, z)}{\bar{d}_{\mathrm{L}}(z)} \,, \tag{3.148}$$

where $\bar{d}_{\mathrm{L}}$ is the background luminosity distance between the observer and the source, along with its perturbation δd_{L} at first order. This enters into the expression because the relation between the perturbed brightness temperature and the comoving number density contains the determinant of the Jacobi map in the observer's frame [59, 64].

The effective result of this additional term is to remove the contribution of the lensing, since the luminosity fluctuations also contain a lensing convergence term which exactly cancels the one in Δ_g [59]. Thus, the HI brightness temperature fluctuations (and associated angular power spectrum) may be treated like those of the galaxy number counts, provided that the effective magnification is set to

$$\left(s_{\mathrm{IM}}^{\mathrm{HI}}\right)_{\mathrm{eff}} = \frac{2}{5} \,. \tag{3.149}$$

Hence, we have

$$\Delta_T = \Delta_N\left(b_e = \frac{\partial \ln\left(\bar{T}^{\mathrm{HI}}\mathcal{H}\right)}{\partial \ln a} - 3, s = \frac{2}{5}\right) \,. \tag{3.150}$$

3.7 CMB lensing power spectrum

Another source of information regarding the perturbations in the dark matter density distribution is found in the weak lensing of CMB photons by dark matter along the line of sight. This deflection causes a shift in the apparent position of hot and cold spots in
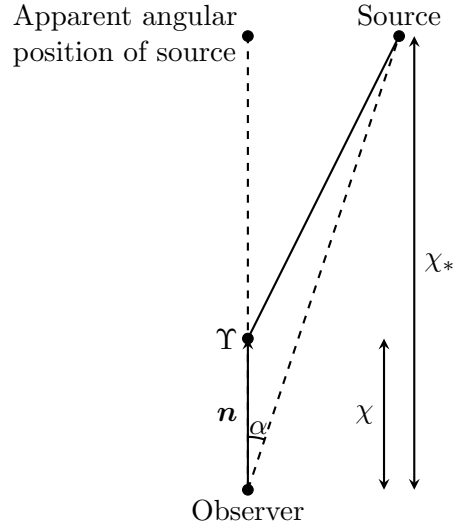
FIGURE 3.4: This figure shows the geometry of the weak lensing phenomenon. Photons from the source travel towards the observer, passing a dark matter potential Υ which changes their direction and thus the perceived direction of the source.

the CMB, which in turn affects the power spectra of CMB temperature and polarization. In this section, following [48], the lensing potential is defined and an expression is derived for the associated power spectrum.

Consider the geometry described in Fig. 3.4, where the deviation of a photon from a source is shown. Assuming a universe with flat curvature, the weak lensing deflection angle α of a source with comoving distance χ_* is given by

$$\alpha(\chi_*) = -2 \int_0^{\chi_*} d\chi \frac{\chi_* - \chi}{\chi_* \chi} \boldsymbol{\nabla_n} \Upsilon(\chi \boldsymbol{n}, \eta_0 - \chi) , \tag{3.151}$$

where Υ is the potential of the matter responsible for the lensing, and η_0 is the present conformal time so that $\eta = \eta_0 - \chi$ is the conformal time at which the photon was at position $\chi \boldsymbol{n}$. $\boldsymbol{\nabla_n}$ is the covariant derivative on the sphere with surface normal $\boldsymbol{n}$.

The lensing potential is ϕ defined as

$$\phi(\boldsymbol{n}) = -2 \int_0^{\chi_*} d\chi \frac{\chi_* - \chi}{\chi_* \chi} \Upsilon(\chi \boldsymbol{n}, \eta_0 - \chi) , \tag{3.152}$$

so that the deflection angle is given by

$$\alpha = \boldsymbol{\nabla_n} \phi . \tag{3.153}$$

In a similar way to the dark matter density contrast, we can define the power spectrum of the potential Υ:

$$\langle \Upsilon(\boldsymbol{k},\eta)\Upsilon^*(\boldsymbol{k}',\eta')\rangle = \frac{2\pi^2}{k^3}P_\Upsilon(k,\eta,\eta')\delta(\boldsymbol{k}-\boldsymbol{k}') \,, \tag{3.154}$$

where the conformal time η plays the role of redshift and $\Upsilon(\boldsymbol{k},\eta)$ denotes the Fourier transform of $\Upsilon(\boldsymbol{x},\eta)$, defined according to (2.5). In terms of this power spectrum, the power spectrum of the lensing potential is then given by

$$\langle \phi(\boldsymbol{n})\phi(\boldsymbol{n}')\rangle = 4\int_0^{\chi_*}\mathrm{d}\chi \int_0^{\chi_*}\mathrm{d}\chi' \left(\frac{\chi_*-\chi}{\chi_*\chi}\right)\left(\frac{\chi_*-\chi'}{\chi_*\chi'}\right)\int \frac{\mathrm{d}^3k}{(2\pi)^6}\frac{2\pi^2}{k^3}P_\Upsilon(k,\eta,\eta')e^{i\boldsymbol{k}\cdot\boldsymbol{x}}e^{-i\boldsymbol{k}\cdot\boldsymbol{x}'} \,. \tag{3.155}$$

Using the plane wave expansion (A.6) and the expansion of Legendre polynomials in spherical harmonics (A.4) we have

$$e^{i\boldsymbol{k}\cdot\boldsymbol{x}} = 4\pi\sum_{\ell=0}^{\infty}\sum_{m=-\ell}^{\ell} i^\ell Y_{\ell m}(\hat{\boldsymbol{k}})Y_{\ell m}^*(\boldsymbol{n})j_\ell(k\chi) \,, \tag{3.156}$$

taking $\boldsymbol{x}=\chi\boldsymbol{n}$. Substituting this into (3.155) and using the orthonormality of the spherical harmonics (A.5) we obtain

$$\langle \phi(\boldsymbol{n})\phi(\boldsymbol{n}')\rangle = \frac{2}{\pi}\sum_{\ell=0}^{\infty}\sum_{m=-\ell}^{\ell}\int_0^{\chi_*}\mathrm{d}\chi \int_0^{\chi_*}\mathrm{d}\chi'\left(\frac{\chi_*-\chi}{\chi_*\chi}\right)\left(\frac{\chi_*-\chi'}{\chi_*\chi'}\right)$$
$$\times \int \frac{\mathrm{d}k}{k}P_\Upsilon(k,\eta,\eta')Y_{\ell m}(\boldsymbol{n})Y_{\ell m}^*(\boldsymbol{n}')j_\ell(k\chi)j_\ell(k\chi') \,. \tag{3.157}$$

As in the case of the dark matter density contrast, we may now expand the lensing potential in spherical harmonics:

$$\phi(\boldsymbol{n},z) = \sum_{\ell=0}^{\infty}\sum_{m=-\ell}^{\ell}\phi_{\ell m}Y_{\ell m}(\boldsymbol{n}) \,. \tag{3.158}$$

and define the angular power spectrum as

$$\langle \phi_{\ell m}\phi_{\ell'm'}^*\rangle = C_\ell^\phi \delta_{\ell\ell'}\delta_{mm'} \,. \tag{3.159}$$

Comparison with (3.157) yields

$$\phi_{\ell m} = \frac{2}{\pi} \int_0^{\chi_*} \mathrm{d}\chi \int_0^{\chi_*} \mathrm{d}\chi' \left(\frac{\chi_* - \chi}{\chi_* \chi} \right) \left(\frac{\chi_* - \chi'}{\chi_* \chi'} \right) \int \frac{\mathrm{d}k}{k} P_\Upsilon(k, \eta_0 - \chi, \eta_0 - \chi') j_\ell(k\chi) j_\ell(k\chi') \ . \tag{3.160}$$

Using a transfer function T_Υ, defined by

$$\Upsilon(\boldsymbol{k}, \eta) = T_\Upsilon(k, \eta) \zeta(k) \ , \tag{3.161}$$

we may rewrite the angular power spectrum of the lensing potential in terms of the power spectrum of the primordial curvature perturbation ζ:

$$C_\ell^\phi(\chi_1, \chi_2) = \frac{2}{\pi} \int \frac{\mathrm{d}k}{k} \mathcal{P}_\zeta(k) \Delta_\ell^\phi(\chi_1) \Delta_\ell^\phi(\chi_2) \ , \tag{3.162}$$

where

$$\Delta_\ell^\phi(\chi) = \int_0^{\chi_*} \mathrm{d}\chi T_\Upsilon(k, \eta_0 - \chi, \eta_0 - \chi') j_\ell(k\chi) \left(\frac{\chi_* - \chi}{\chi_* \chi} \right) \ . \tag{3.163}$$

Chapter 4

Primordial Non-Gaussianity

We have obtained expressions for the information that observational surveys will provide. Using these, we will be able to forecast the constraints that will be possible with these surveys, according to the formalism that will be introduced in the next chapter (see Chapter 5). In this chapter we consider which variables we aim to constrain and the motivation for doing so.

The primary parameter on which we wish to place constraints is the primordial non-Gaussianity parameter f_{NL}, because it acts as a powerful probe of the physics of the early Universe [84, 85]. According to the consistency relation applied to single field slow-roll (SFSR) models, the f_{NL} parameter is first order in slow-roll parameters: $f_{\mathrm{NL}} \simeq -5(n_s - 1)/12$ [86, 87, 89]. In comparison, for many multi-field inflation models it is expected to obey $f_{\mathrm{NL}} \gtrsim 1$ [88]. Thus, if it can be sufficiently well-constrained by observation, it may be possible to rule out some inflationary models. This chapter describes the primordial non-Gaussianity (PNG), the motivation to constrain it and the forecasts of the constraints possible using the multi-tracer approach.

4.1 Tracers to constrain PNG

The current tightest constraints on the primordial non-Gaussianity (PNG) are calculated using the bispectrum from *Planck* measurements of the three-point correlation function

75

of the anisotropies in the CMB temperature and polarization maps:

$$f_{\rm NL} = -0.9 \pm 5.1 \ , \tag{4.1}$$

at 68% CL [91]. However, the large-scale structure (LSS) is becoming increasingly useful as an alternate choice of observable: $-51 < f_{\rm NL} < 21$ at 95% CL from eBOSS DR14 data [104]. It is for this reason that galaxy number counts and HI intensity mapping are chosen as complementary tracers in this work.

The power spectrum of an LSS tracer is able to constrain $f_{\rm NL}$ because the PNG produces a scale dependence in the bias, via the long-wavelength primordial gravitational potential Φ. In turn, this modulates the local short-scale power spectrum of galaxy clustering, producing a measurable signal which can be used to constrain the PNG [92, 93]. The specific form of scale-dependence which results when Φ is present in the halo bias cannot be created by late time processes, which makes the halo bias a robust probe of non-Gaussianity in the primordial Universe. In the case of a *local* model of PNG, a k^{-2} scaling arises, making the signal most prominent on the largest scales of the matter power spectrum [98–102] (see Fig. 4.1). At these scales, larger than the equality scale, cosmic variance has a strong effect, placing a fundamental limit on the possible precision in measurements of $f_{\rm NL}$ from a single LSS tracer [103].

The cross-correlation between CMB lensing and clustering of galaxies has also recently been shown to be particularly effective in constraining local PNG [96, 97]. So, by combining these tracers using the multi-tracer approach, we will be able to constrain the PNG below the cosmic variance limit, conceivably to a sufficiently high degree to discriminate between possible inflationary models.

4.2 Defining $f_{\rm NL}$

As shown before, the primordial gravitational potential is given by $\Phi_p(\boldsymbol{k}) = -\frac{3}{5}\zeta(\boldsymbol{k})$. The primordial non-Gaussianity parameter $f_{\rm NL}$ is then defined by

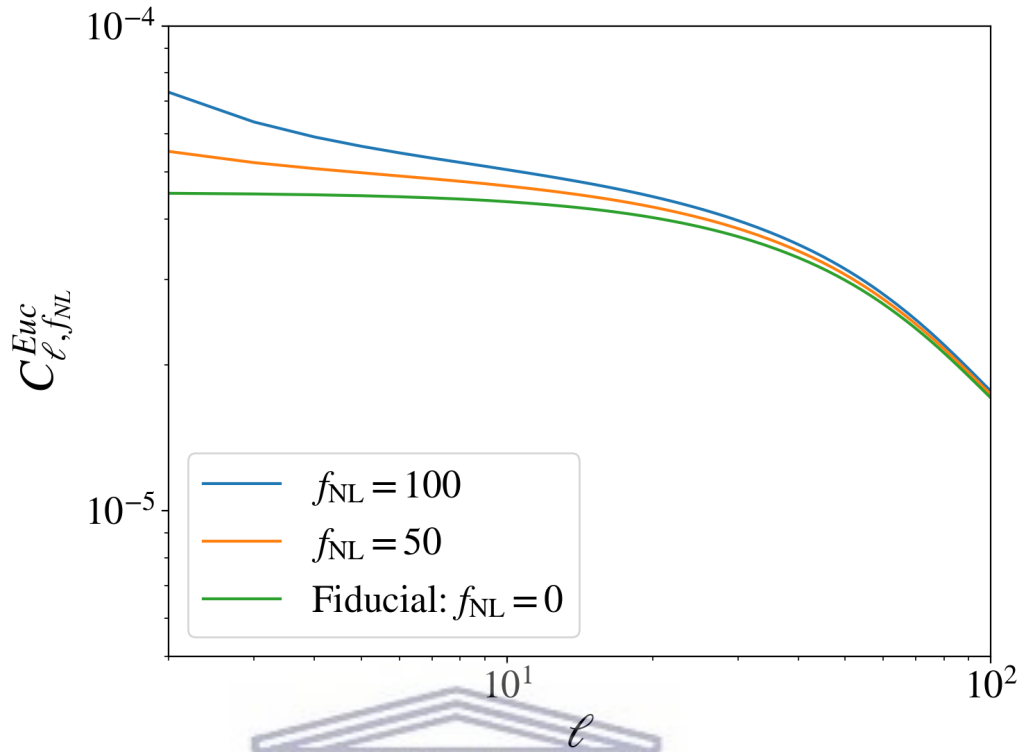$$-\Phi_p = \varphi_G + f_{\rm NL}\left(\varphi_G^2 - \langle\varphi_G^2\rangle\right) \ , \tag{4.2}$$

FIGURE 4.1: Angular power spectra from a bin of a Euclid-like survey (see Section 5.2) in three different cases. In green we see the fiducial model with no PNG. In orange the case where $f_{\rm NL} = 50$ and in blue the angular power spectrum when $f_{\rm NL} = 100$. We see that the presence of PNG results in an increased amplitude at only the very largest scales.

where the Gaussian field $\varphi_G = \frac{3}{5}\zeta_G$ is the potential related to the Gaussian limit of the curvature perturbation. In this definition, the parameter $f_{\rm NL}$ is assumed to be independent of scale. In this work we also consider a generalization of this model where $f_{\rm NL}$ becomes a function of scale: [105–107]

$$f_{\rm NL}(k) = f_{\rm NL} \left(\frac{k}{k_{\rm piv}} \right)^{n_{\rm NL}}, \tag{4.3}$$

where $k_{\rm piv}$ is a pivot scale fixed here to $0.035h/{\rm Mpc}$ and $n_{\rm NL}$ is known as the running index. Currently, the tightest observational constraint on $n_{\rm NL}$ comes from the bispectra of the CMB anisotropies: $-0.6 < n_{\rm NL} < 1.4$ at 68% CL from WMAP9 data, in the case of a single-field curvaton [108, 109].

4.3   Scale-dependent halo bias

In order to show how PNG results in a scale-dependence in the halo bias, we can describe the large-scale halo bias in the context of the peak-background split (PBS) [110–113]. Within this formalism, the Gaussian field is split into respective long- and short-scale modes $\varphi = \varphi_\ell + \varphi_s$, where the long scales correspond to the clustering scale of halos, or the large-scale power spectrum, and the short scales are comparable to the extent of the halos themselves.

In the convention used here, the perturbed metric is given by

$$a^{-2}ds^2 = -(1 + 2\Phi)d\eta^2 + (1 - 2\Psi)dx_i dx^i \ . \tag{4.4}$$

In the same convention, the Poisson equation at late times is given by

$$\nabla^2 \Phi = \frac{3}{2}\Omega_{m0}H_0^2 \frac{\delta_{mC}}{a} \tag{4.5}$$

with δ_{mC} the comoving dark matter density contrast. This allows us to connect the density contrast to the gravitational potential Φ.

Now, at late times, we can also connect the gravitational potential Φ to the primordial potential $\Phi_{\rm p}$ using (see (2.50))

$$\Phi(\boldsymbol{k}, z) = \frac{T(k)\Phi_p(\boldsymbol{k})D(z)}{a(z)} \ , \tag{4.6}$$

where D is normalized so that the definition of $f_{\rm NL}$ is consistent with the definition of $f_{\rm NL}$ for local PNG in the CMB temperature, i.e. it is normalized with respect to the matter-dominated era: $D(z = 0) \approx 0.8$, since in the matter-dominated era

$$D(a) = a \tag{4.7}$$

This is the same normalization as in (2.48). However, there are two conventions used in the literature to define $f_{\rm NL}$ in (4.2): the LSS convention where Φ is normalized at $z = 0$, and the CMB convention where Φ is instead the primordial potential. The

relation between the two normalizations is

$$f_{\text{NL}}^{\text{LSS}} = \frac{D(z=z_{\text{d}})(1+z)}{D(z=0)} f_{\text{NL}}^{\text{CMB}} \; . \tag{4.8}$$

In the analysis that follows we have chosen to adopt the CMB convention. If we wish to make use of the alternate LSS normalization for the growth factor (i.e. $D(z=0)=1$), for example in the CAMB code, we need to rewrite the potential as follows:

$$\Phi(\boldsymbol{k},z) = \frac{T(k)\Phi_p(\boldsymbol{k})D(z)}{a(z)g_{\text{d}}} \; , \tag{4.9}$$

where g_{d} may be determined from (2.52), in order to ensure a consistent normalization with the CMB.

From the Poisson equation (4.5), we can write the matter density contrast as

$$\delta_{mC}(\boldsymbol{k},z) = -\alpha(k,z)\Phi_p(\boldsymbol{k}) \; , \tag{4.10}$$

with

$$\alpha(k,z) \equiv \frac{2k^2 T(k)D(z)}{3\Omega_{m0}H_0^2} \; . \tag{4.11}$$

Then, using (4.2) and (4.10), we obtain

$$\delta_{mC}(\boldsymbol{k},z) = \delta_{mC,G}(\boldsymbol{k},z)[1 + f_{\text{NL}}\varphi_G(\boldsymbol{k})] \; , \tag{4.12}$$

where

$$\delta_{mC,G}(\boldsymbol{k},z) = \alpha(k,z)\varphi_G(\boldsymbol{k}) \; , \tag{4.13}$$

is the Gaussian comoving density contrast.

The comoving galaxy density contrast is given in the Gaussian case by

$$\delta_{gC,G}(\boldsymbol{k},z) = b_G(z)\delta_{mC,G}(\boldsymbol{k},z) \; . \tag{4.14}$$

From (4.12) we see that the non-Gaussian bias will no longer be scale-independent, but will correct b_G by a factor $\propto f_{\text{NL}}$.

In presence of local PNG defined as in (4.2), the Laplacian of the primordial potential is

$$\nabla^2 \Phi_p \simeq \nabla^2 \varphi_G + 2 f_{\mathrm{NL}} \left(\varphi_G \nabla^2 \varphi_G + |\nabla \varphi_G|^2 \right) \ . \tag{4.15}$$

We split the potential into long and short wavelength modes at leading order:

$$\Phi_\ell \approx \varphi_\ell \ , \tag{4.16}$$

$$\Phi_s \approx \varphi_s \left(1 + 2 f_{\mathrm{NL}} \varphi_\ell \right) \ , \tag{4.17}$$

where we reiterate that the long and short wavelength modes are associated respectively with the large-scale clustering characteristics of the matter distribution and the small-scale clustering of halo formation.

The long-wavelength overdensity δ_ℓ is unaffected by the presence of PNG, retaining the Gaussian form:

$$\delta_\ell(\boldsymbol{k}, z) = \alpha(k, z) \varphi_\ell(\boldsymbol{k}) \ . \tag{4.18}$$

These long-wavelength modes effectively control fluctuations in the background density of the local cosmology. However, the short-wavelength fluctuations become coupled to the long-wavelength modes, which results in an excess or deficit in halo formation, depending on the large-scale density fluctuations. At lowest order, neglecting white-noise contributions, we have

$$\delta_s(\boldsymbol{k}, z) = \alpha(k, z) \varphi_s(\boldsymbol{k}) \left(1 + 2 f_{\mathrm{NL}} \varphi_\ell(\boldsymbol{k}) \right) \ . \tag{4.19}$$

Hence, if PNG is present, the local number of halos is affected not only by the large-scale matter perturbations, but also by the coupling between long- and short-wavelength modes. The coupling results in an effective local rescaling of the amplitude of the small-scale matter fluctuations.

In Lagrangian space the local halo number density is given by [110, 111]

$$n_h = \bar{n}_h \left(1 + b_{\mathrm{L}} \delta_\ell \right) \ , \tag{4.20}$$

where b_{L} is the Lagrangian-space bias. Thus we have

$$b_{\mathrm{L}} = \frac{\mathrm{d} \ln n_h}{\mathrm{d} \delta_\ell} \ , \tag{4.21}$$

and, in terms of the Eulerian-space convention used implicitly up to this point, the bias is given by $b = 1 + b_{\rm L}$. Taylor expanding at first order in these parameters yields

$$
\begin{aligned}
b_{\rm L} &= \frac{\partial \ln n_h}{\partial \delta_\ell} + \frac{\partial \ln n_h}{\partial \left(1 + 2 f_{\rm NL} \varphi_\ell\right)} \frac{\partial \left(1 + 2 f_{\rm NL} \varphi_\ell\right)}{\partial \varphi_\ell} \frac{\partial \varphi_\ell}{\partial \delta_\ell} \\
&= \frac{\partial \ln n_h}{\partial \delta_\ell} + \frac{2 f_{\rm NL}}{\alpha} \frac{\partial \ln n_h}{\partial \ln \sigma_8^{\rm loc}} = b_{\rm L}^{\rm G} + \Delta b \,,
\end{aligned}
\tag{4.22}
$$

where we have parametrized the local amplitude of small-scale fluctuations with $\sigma_8^{\rm loc} = \sigma_8 \left(1 + 2 f_{\rm NL} \varphi_\ell\right)$, scaled by $\left(1 + 2 f_{\rm NL} \varphi_\ell\right)$ as implied by (4.19), and we have introduced the scale-dependent contribution to the large-scale bias:

$$
\Delta b(k, z) = f_{\rm NL} \frac{\beta_f}{\alpha(k, z)} \,,
\tag{4.23}
$$

where we take $\beta_f = 2\delta_c(b - 1)$, which assumes a barrier-crossing model with barrier height δ_c and is in good agreement ($\sim 10\%$ error) with N-body simulations [98]. Finally, on large scales we can relate the halo density contrast to the linear density field as

$$
\delta_h(k, z) = \left[b(z) + \Delta b(k, z)\right] \delta_m(k, z) \,,
\tag{4.24}
$$

where $b = 1 + b_{\rm L}^{\rm G}$ is the familiar Eulerian-space bias, in the Gaussian case. Notice that the non-Gaussian linear bias is no longer scale-independent, rather correcting the Gaussian linear bias b by a factor $\propto f_{\rm NL}/k^2$.

Chapter 5

Calculating Constraints

5.1 The Fisher forecasting formalism

Fisher Forecasting is a Bayesian method which can be used in general to calculate the constraints on parameters, given data and a corresponding model [51]. In this case, the data are simulated observations of the angular power spectrum, while the model consists of cosmological parameters that specify the theoretical angular power spectrum. The expressions that follow are specific to an application of this method to cosmological observations and assume the special case that the probability distributions of the parameters are Gaussian.

5.1.1 The Fisher information matrix

In the case of cosmological observations on the sky, the Fisher matrix may be calculated according to the following [52, 53]:

$$\mathbf{F}_{\alpha\beta} = f_{sky} \sum_{\ell=2}^{\ell_{max}} \left(\frac{2\ell+1}{2} \right) Tr \left[C_{\ell,obs}^{-1} \frac{\partial C_{\ell,obs}}{\partial \theta_\alpha} C_{\ell,obs}^{-1} \frac{\partial C_{\ell,obs}}{\partial \theta_\beta} + C_{\ell,obs} M_{\ell,\alpha\beta} \right] , \qquad (5.1)$$

where θ_α are the parameters in question (see Section 5.3) and $M_{\ell,\alpha\beta} = \left(\frac{\partial Z_\ell}{\partial \theta_\alpha} \frac{\partial Z_\ell^T}{\partial \theta_\beta} + \frac{\partial Z_\ell}{\partial \theta_\beta} \frac{\partial Z_\ell^T}{\partial \theta_\alpha} \right)$, where the matrix Z_ℓ corresponds to some fiducial model. In a realistic treatment, the observed angular power spectrum $C_{\ell,obs}$ must be used. This contains information relating to the limitations of the instruments used for observation, since what is actually

82

observed is not the theoretical power spectrum derived previously (see (3.25)). Instead, we observe the signal of the theoretical power spectrum C_ℓ (calculated numerically using CAMB[1] [45, 52, 94, 95]) with additional noise terms (see (5.4) and (5.5)). These terms are dependent on the survey type and will be discussed in more detail later in this chapter, together with the survey specifications used in this work. The sky fraction f_{sky}, which takes into account the portion of the sky covered by an observation, is also included here. The expression also takes into account the maximum multipole limit ℓ_{max}, which is related to smallest scale that a particular survey is able to resolve. Depending on the survey, the minimum multipole included in the sum may also be adjusted to account for the removal of lower multipoles during foreground cleaning and for the fact that the sky coverage (and thus the number of available large-scale modes) may be limited.

5.1.2 Marginalized and fixed parameters

The constraints on parameters may be extracted from the Fisher matrix as conditional or marginalized errors. Conditional errors are the constraints possible in the most optimistic case where the values of all the other parameters under consideration are known with complete certainty, i.e. the other parameters are fixed at their fiducial values. In this case the conditional error on the parameter θ_α is given by

$$\sigma_{\alpha\alpha} = \frac{1}{\sqrt{F_{\alpha\alpha}}} .$$
(5.2)

The marginalized error is a less optimistic, though a more realistic measure of the error on a particular parameter, which takes into account the errors on the other parameters by marginalizing over all possible values which they can assume. The marginalized error on parameter θ_α may be calculated from the Fisher matrix using the following:

$$\sigma_{\alpha\alpha} = \sqrt{(F^{-1})_{\alpha\alpha}} .$$
(5.3)

---

[1]https://github.com/cmbant/CAMB

5.2 Survey specifications

There are three survey types considered in this work, namely CMB lensing, HI intensity mapping (HI IM) and photometric galaxy clustering surveys. Each has its own specifications and systematic effects to take into account (see Table 5.1 for a summary of the survey specifications). In this section we describe each of the surveys as well as the observational effects particular to each and how these are included in the Fisher formalism in a combined "multi-tracer" approach.

As mentioned, the measurement of observed power spectrum does not equate to measuring the theoretical power spectrum as derived in Chapter 4, even once all the relativistic light-cone effects are included. There are additional systematic effects from experimental limitations which must be taken into account to obtain more realistic constraints.

5.2.1 Noise

The cases of CMB and HI intensity mapping may be treated analogously to each other, taking care of the instrumental effects of noise and the beam (the effect of limited angular resolution). As in [55] and [54], the form that the observed signal takes for both of these kinds of surveys is

$$C_{\ell,obs}^{ij} = C_\ell^{ij} + \frac{\mathcal{N}_{instr,\ell}^{ij}}{\mathcal{B}_\ell^i \mathcal{B}_\ell^j} . \tag{5.4}$$

Here $\mathcal{N}_{instr}$ is thermal noise and $\mathcal{B}_\ell^i$ is the contribution of the beam in harmonic space.

In the case of galaxy number counts, the dominant contribution to noise is the Poisson shot noise $\mathcal{N}_{Poiss}$, and the observed power spectrum is

$$C_{\ell,obs}^{ij} = C_\ell^{ij} + \mathcal{N}_{Poiss}^{ij} . \tag{5.5}$$

The particular noise characteristics for each of these surveys will be discussed later in this section.

5.2.2 CMB lensing specifications

The CMB provides data in the form of the CMB temperature, polarization and lensing angular power spectra. In this work we consider a possible ground-based CMB Stage 4 (CMB-S4) configuration. For temperature and polarization CMB angular power spectra, the instrumental noise is defined by [66]

$$\mathcal{N}_\ell^{\mathrm{T,P}} = \sigma_{\mathrm{T,P}} \ . \tag{5.6}$$

We assume noise of $\sigma_{\mathrm{T}} = \sigma_{\mathrm{P}}/\sqrt{2} = 1\,\mu\mathrm{K}$-arcmin [65] and a Gaussian beam with the following form in angular space [66]:

$$\mathcal{B}_\ell^i = e^{\frac{-\ell(\ell+1)(\theta_\mathcal{B}^i)^2}{2}} \ , \tag{5.7}$$

with

$$\theta_\mathcal{B}^i = \frac{\theta_{FWHM}^i}{2\sqrt{2\ln 2}} \ , \tag{5.8}$$

where $\theta_{FWHM}^i = 3$ arcmin [65]. We also implement a low multipole cut of $\ell_{\min} = 30$ in each spectrum [65] and different cuts at high-ℓ of $\ell_{\max}^{\mathrm{T}} = 3000$ in temperature and $\ell_{\max}^{\mathrm{P}} = 5000$ in polarization, with the sky fraction taken as $f_{\mathrm{sky}} = 0.4$.

For the case of CMB lensing, we assume that lensing reconstruction can be performed iteratively, using the minimum variance quadratic estimator on the full sky. This involves the combining of the TT, EE, BB, TE, TB and EB CMB estimators, calculated according to [67], with `quicklens`[2], followed by iterative lensing reconstruction [68, 69]. The lensing spectrum multipole cuts are the same as those for the temperature spectrum.

Hereafter "CMB" will refer to the full set of angular power spectra of the CMB anisotropies, i.e. temperature, E-mode polarization, CMB lensing, and their cross-correlations.

5.2.3 HI intensity mapping specifications

An intensity mapping survey measures the total intensity of emission in each pixel for a given set of atomic line(s), which leads to the measurement of very accurate redshifts

---

[2]https://github.com/dhanson/quicklens

[70–75]. The surveys do not allow us to count individual galaxies, since these aren't resolved themselves. However, the galaxies can host atoms emitting in the chosen lines and the fluctuations in the measured brightness temperature are expected to be a biased tracer of the underlying cold dark matter distribution.

In this work we consider the particular line associated with HI emission and make use of the fitting formulae from [76] for the SKA1-MID HI linear bias:

$$b_{\mathrm{HI}}(z) = \frac{b_{\mathrm{HI}}(0)}{0.677105}\Big[0.66655 + 0.17765\,z + 0.050223\,z^2\Big]\,, \tag{5.9}$$

as well as for the background HI brightness temperature:

$$\bar{T}_{\mathrm{HI}}(z) = 0.055919 + 0.23242\,z - 0.024136\,z^2\ \mathrm{mK}\,, \tag{5.10}$$

where $\Omega_{\mathrm{HI}}(0)b_{\mathrm{HI}}(0) = 4.3 \times 10^{-4}$ and $\Omega_{\mathrm{HI}}(0) = 4.86 \times 10^{-4}$.

An IM survey consisting of N_{dish} dishes, each in single dish mode (i.e. not interferometer mode) will have a noise variance in the i-frequency channel given by [66, 73]

$$\mathcal{N}^{\mathrm{HI}}_{instr,\ell}(\nu_{\mathrm{i}}) \equiv \sigma_{\mathrm{HI}}(\nu_{\mathrm{i}}) = \frac{4\pi f_{\mathrm{sky}}T^2_{\mathrm{sys}}(\nu_{\mathrm{i}})}{2N_{\mathrm{dish}}t_{\mathrm{tot}}\Delta\nu}\,, \tag{5.11}$$

$$\tag{5.12}$$

assuming scale-independence and no correlation between the noise in different frequency channels, where t_{tot} is the total observing time and the system temperature is given by

$$T_{\mathrm{sys}}(\nu)\ \ = T_{instr} + T_{sky}\,, \tag{5.13}$$

where the instrument and sky temperatures are given by $T_{instr} = 25$ K and $T_{sky} = 60\left(\frac{300\,\mathrm{MHz}}{\nu}\right)^{2.55}$ K respectively.

We assume a Gaussian beam for HI IM with the same form as for the CMB [54, 55]:

$$\mathcal{B}^i_\ell = e^{\frac{-\ell(\ell+1)\left(\theta^i_{FWHM}\right)^2}{16\ln 2}}\,, \tag{5.14}$$

with

$$\theta^i_{FWHM} \approx \frac{c}{\nu^i D_{dish}}\,. \tag{5.15}$$
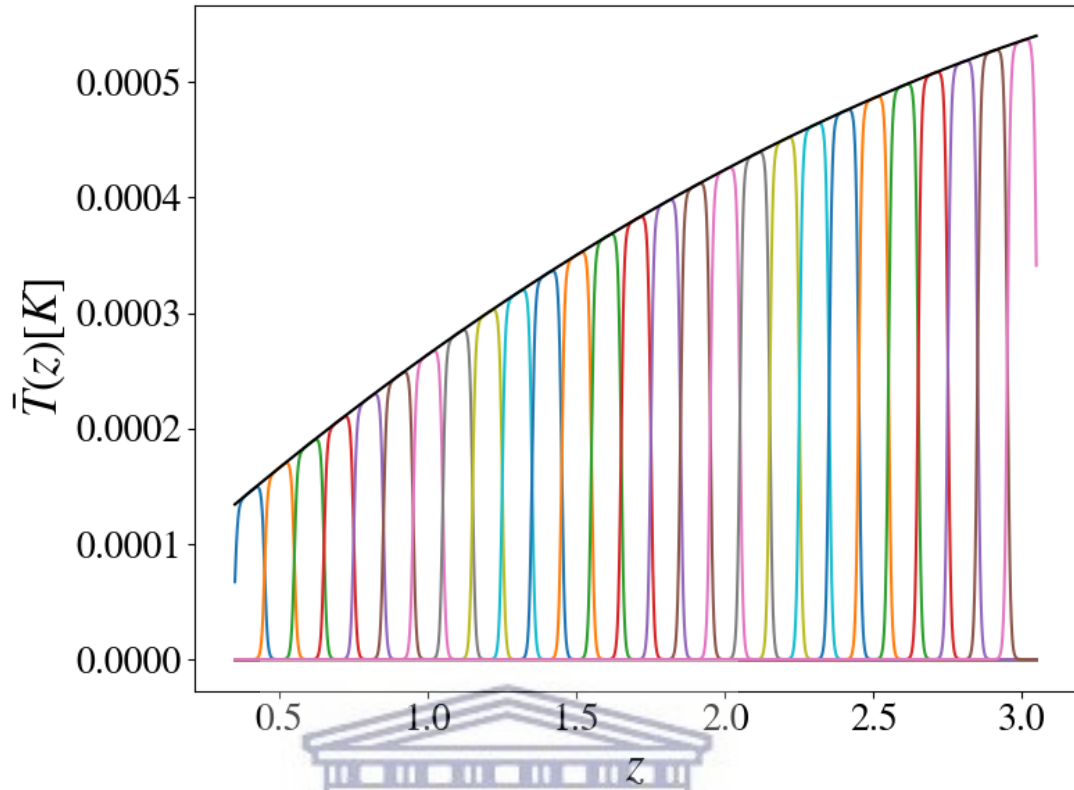
FIGURE 5.1: HI intensity mapping redshift distribution. In black: The brightness temperature (effective redshift distribution) function used for HI IM. In colours: The distribution integrated over smoothed top-hat window functions (see (5.24)) in each one of the 27 bins of width 0.1 in redshift.

For SKA1-MID, we assume $N_{\mathrm{dish}} = 197$ dishes of diameter $D_{\mathrm{dish}} = 15$ m, observing for $t_{\mathrm{tot}} = 10^4$ hr over 20 000 deg^2 of sky. The redshift range assumed is $0.35 \leq z \leq 3.05$ (1050 $\geq \nu \geq 350\,\mathrm{MHz}$, Band 1) [77], divided in 27 tomographic bins, each with width $\delta z = 0.1$. The cleaning of foregrounds from HI IM effectively removes the largest scales, $\ell_{\mathrm{min}} \lesssim 5$ [56, 57] and so we implement a minimum a multipole cut at $\ell_{min} = 5$.

5.2.4 Photometric galaxy survey specifications

In this work we consider two planned future photometric galaxy surveys. Each survey requires the specification of the total redshift distribution of sources $\bar{N}$, which has the following general form:

$$\bar{N}(z) \propto z^{\alpha} \exp\left[-\left(\frac{z}{z_0}\right)^{\beta}\right] \mathrm{gal/arcmin}^2 \,, \tag{5.16}$$

as well as the linear bias. Provision is made to account for uncertainties in the redshift, and thus the distribution of sources in the ith redshift bin is modified according to [78], which gives

$$\bar{N}^i(z) = \int_{z_{\mathrm{ph}}^i}^{z_{\mathrm{ph}}^{i+1}} \mathrm{d}z_{\mathrm{ph}} \bar{N}(z) p(z_{\mathrm{ph}}|z) \ , \tag{5.17}$$

where the ith observed photometric bin occupies the range $z_{\mathrm{ph}}^i, z_{\mathrm{ph}}^{i+1}$ and we adopt a Gaussian distribution for the probability distribution of photometric redshift estimates z_{ph}, given true redshifts z:

$$p(z_{\mathrm{ph}}|z) = \frac{1}{\sqrt{2\pi}\sigma_z} \exp\left[-\frac{(z - z_{\mathrm{ph}})^2}{2\sigma_z^2}\right] \ . \tag{5.18}$$

$\bar{N}^i$ is the redshift distribution (number density per redshift per solid angle) of sources that was defined previously (see (3.2)), but now takes into account the uncertainty in redshift measurements.

The Poisson noise contribution is calculated for the ith bin as the inverse of the number density per solid angle in the ith bin [54, 58]:

$$\mathcal{N}_{Poiss,i}^{jk} = \frac{\delta^{jk}}{\bar{n}^i} \ , \tag{5.19}$$

where $\bar{n}^i$ is calculated by integrating over redshift:

$$\bar{n}^i = \int \mathrm{d}z \ \bar{N}^i(z) \ . \tag{5.20}$$

For both galaxy surveys we impose a multipole cut on small-scales, assuming that observations will be able to probe non-linear scales up to $k_{\mathrm{max}} = 0.3 \ h/\mathrm{Mpc}$ which relates to a redshift-dependent maximum multipole $\ell_{\mathrm{max}} \simeq \chi(z)k_{\mathrm{max}} - 1/2$.

5.2.4.1 Euclid-like survey

Euclid is a space-based experiment of the ESA Cosmic Vision program, with the satellite set to be launched in 2022 [79]. It is scheduled to perform both a photometric and a spectroscopic galaxy survey. Here, we focus on a survey with specifications similar to the Euclid photometric survey. In particular, such a survey would observe a sky area of $\Omega_{\mathrm{sky}} = 15\,000 \ \mathrm{deg}^2$, with an average source count of $\bar{N} = 30$ sources per arcmin^2. The
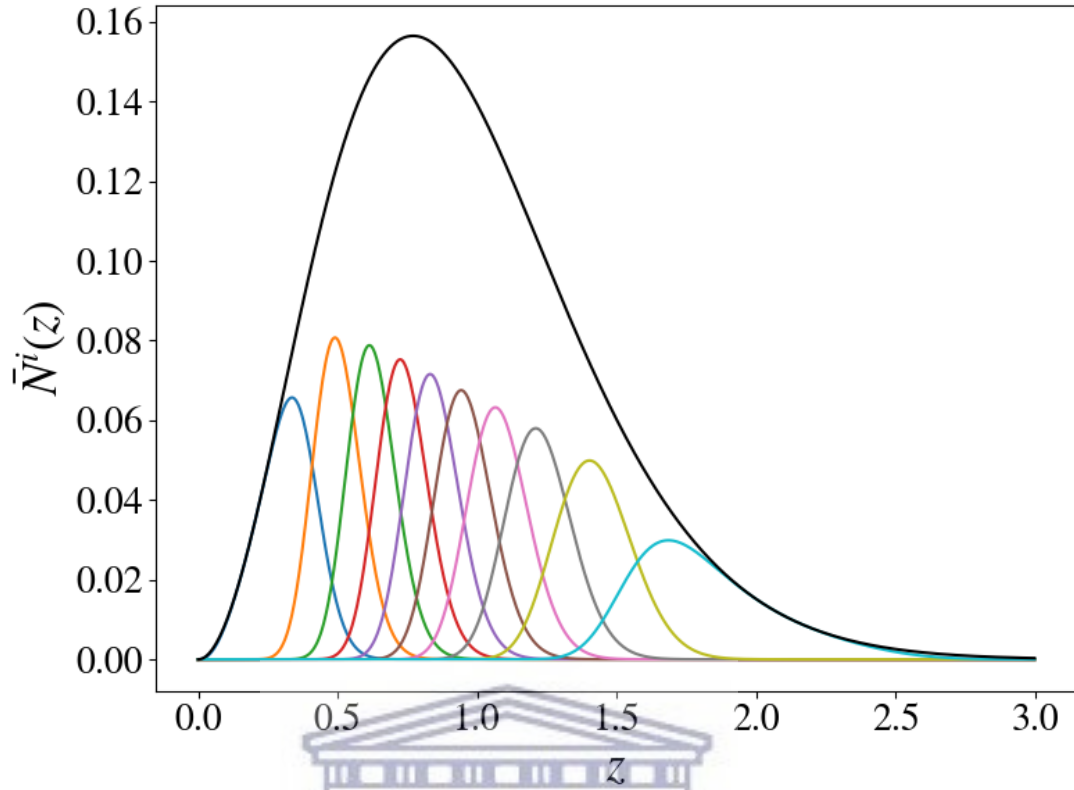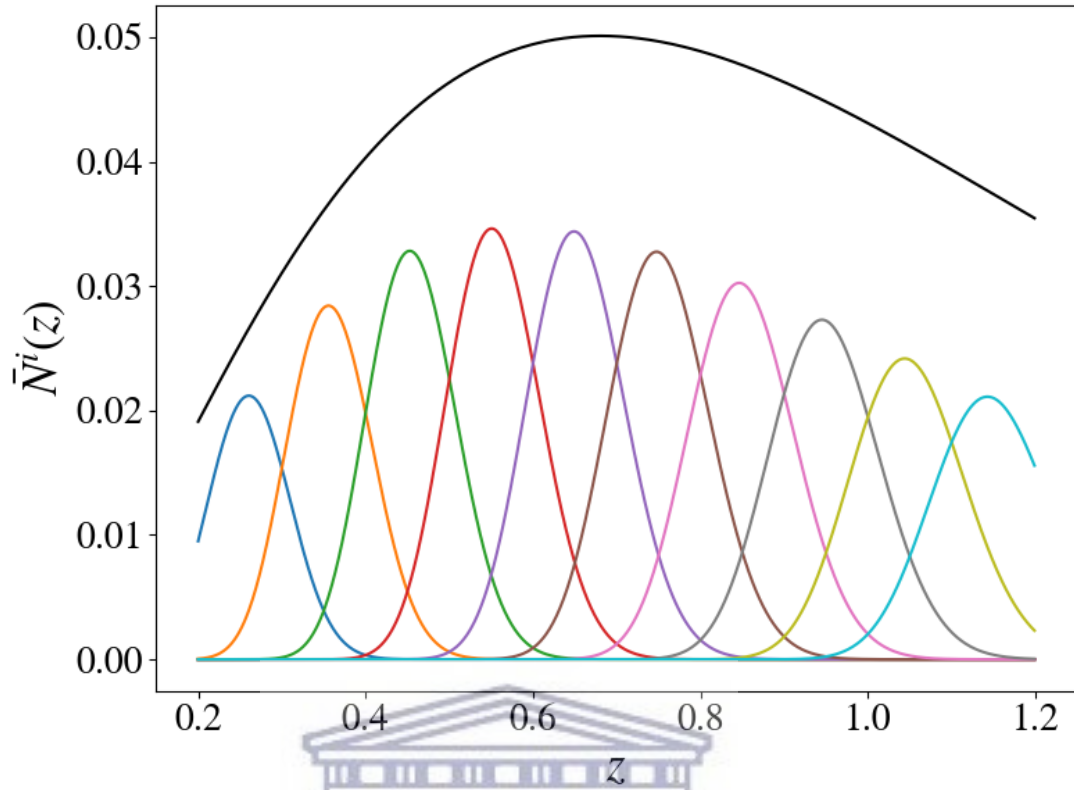
FIGURE 5.2: In black: The redshift distribution function for galaxies in a Euclid-like survey spanning the redshift range $0 < z < 3$. In colours: The redshift distribution for each of the 10 bins containing equal numbers of sources, accounting for the Gaussian spread due to uncertainties in the measured photometric redshift: $\sigma_z = 0.05(1 + z)$.

redshift distribution of sources for a Euclid-like photometric survey follows (5.16) with $\alpha = 2$, $\beta = 1.5$, and $z_0 = 0.636$.

Measurements are taken in the redshift range from $z = 0$ to $z = 2.5$ [80], which we divide into 10 bins, each containing equal numbers of galaxies [80]. The uncertainty in the photometric redshift estimate is assumed to be $\sigma_z = 0.05(1 + z)$ with respect to the true redshift value, and the linear galaxy bias is taken to evolve with redshift according to a fiducial model given by [80]

$$b_g(z) = \sqrt{1 + z} \ . \tag{5.21}$$

A large-scale multipole cut of $\ell_{\min} = 10$ is assumed for this survey.

FIGURE 5.3: In black: The redshift distribution function for galaxies in an LSST-like survey spanning the redshift range $0.2 < z < 1.2$. In colours: The redshift distribution for each of the 10 bins of width 0.1 in redshift, accounting for the Gaussian spread due to uncertainties in the measured photometric redshift: $\sigma_z = 0.03(1 + z)$.

5.2.4.2 LSST-like survey

The other survey we consider is a photometric survey with specifications similar to the one planned by the LSST Dark Energy Science Collaboration for the ground-based Large Synoptic Survey Telescope. We assume an observation over a patch of the sky with $f_{\rm sky}$ equivalent $\Omega_{\rm sky} = 13\ 800$ deg^2, detecting an average of $\bar{n}_{\rm g} = 48$ sources per arcmin^2 distributed in redshift following (5.16) with $\alpha = 2$, $\beta = 0.9$, and $z_0 = 0.28$ [81]. We divide the observed redshift range into 10 tomographic bins with widths of 0.1 in photo-z between $z = 0.2$ and $z = 1.2$. We assume a photometric redshift uncertainty of $\sigma_z = 0.03(1 + z)$ with respect to the true redshift z, and a fiducial model for the linear bias given by [81]

$$b_g(z) = 0.95/D(z) \,, \tag{5.22}$$

where $D(z)$ is the matter growth factor (see Section 1.5.2.3). We assume a slightly larger scale multipole cut of $\ell_{\rm min} = 20$ than for Euclid, because of the comparatively smaller

Parameter	CMB-S4 (T,E,ϕ)	SKA1-MID	Euclid-like	LSST-like
Noise	σ_T, σ_E, σ_ϕ	$\frac{4\pi f_{\mathrm{sky}} T^2_{\mathrm{sys}}(\nu_{\mathrm{i}})}{2N_{\mathrm{dish}} t_{\mathrm{tot}} \Delta\nu}$	$\frac{1}{\bar{n}^i}$	$\frac{1}{\bar{n}^i}$
Redshift Distribution	-	$\bar{T}_{\mathrm{HI}}(z)$ (5.10)	$z^2 \exp\left[-\left(\frac{z}{0.636}\right)^{1.5}\right]$	$z^2 \exp\left[-\left(\frac{z}{0.28}\right)^{0.9}\right]$
Beam θ^i_{FWHM}	3 arcmin	$\frac{c}{\nu^i D_{dish}}$	-	-
σ_z	-	-	$0.05(1+z)$	$0.03(1+z)$
$b(z)$	-	$b_{\mathrm{HI}}(z)$ (5.9)	$b_g(z) = \sqrt{1+z}$	$b_g(z) = 0.95/D(z)$
Redshift range	-	$0.35 - 3.05$	$0 - 2.5$	$0.2 - 1.2$
Number of Bins	-	27	10	10
f_{sky}	0.40	0.48	0.36	0.33
ℓ_{max}	3000,5000,3000	500	$\lfloor 0.3\chi - 1/2 \rfloor$	$\lfloor 0.3\chi - 1/2 \rfloor$
ℓ_{min}	30	5	10	20

TABLE 5.1: Technical specifications for different surveys.

sky area.

5.3 The multi-tracer approach

We describe in this section further details of the Fisher methodology used to determine constraints, specifically the procedure to be followed when multiple tracers are involved, and the full set of parameters used in the analysis.

5.3.1 Multiple tracers

A crucial component of this work is the cross-correlation of multiple tracers of the underlying dark matter distribution. In order to obtain constraints within this paradigm, we must be able to combine different data sets within the Fisher analysis. As before, according to (5.1), the Fisher Matrix is calculated at each multipole ℓ from the angular power spectra. From Chapter 2 and Chapter 3, these all share a similar general form given by (see (3.25))

$$C_\ell^{\mathrm{XY}}(z_i, z_j) = 4\pi \int \mathrm{d}\ln k \, \mathcal{P}_\zeta(k) \Delta_\ell^{\mathrm{X,W}}(k, z_i) \Delta_\ell^{\mathrm{Y,W}}(k, z_j) \,, \tag{5.23}$$

where the redshift dependence is suppressed, X, Y = T, E, ϕ for the CMB, and X, Y = g, HI for the galaxy number counts or HI IM brightness temperature perturbations,

respectively. Here, $\mathcal{P}_\zeta$ is the dimensionless primordial power spectrum and the kernels $\Delta_\ell^{W,X}$ are described in the previous chapters (see (2.57) and (3.142)) where both $\Delta_\ell^{g,W}$ and $\Delta_\ell^{\mathrm{HI,W}}$ include the window function and observational corrections from [45, 82]. As stated, the effective window function for the galaxy counts is the Gaussian probability distribution of photometric redshift. For the HI intensity mapping, the window function used is a smoothed top-hat window function of the form

$$W(z) = A \left(1 + \tanh \left(\frac{z_{i+1} - z}{s} \right) \right) \left(1 + \tanh \left(\frac{z - z_i}{s} \right) \right) \tag{5.24}$$

for the ith bin $[z_i, z_{i+1}]$, where A is a normalization constant and s is a parameter controlling the smoothness and is set to 0.01. The details of the CMB temperature and polarization window functions can be found in [90].

For multiple tracers the full covariance matrix takes the form:

$$C_\ell = \begin{pmatrix} C_\ell^{\mathrm{TT}} & C_\ell^{\mathrm{TE}} & C_\ell^{\mathrm{T}\phi} & C_\ell^{\mathrm{THI_1}} & ... & C_\ell^{\mathrm{Tg_1}} & ... \\ C_\ell^{\mathrm{ET}} & C_\ell^{\mathrm{EE}} & C_\ell^{\mathrm{E}\phi} & C_\ell^{\mathrm{EHI_1}} & ... & C_\ell^{\mathrm{Eg_1}} & ... \\ C_\ell^{\phi\mathrm{T}} & C_\ell^{\phi\mathrm{E}} & C_\ell^{\phi\phi} & C_\ell^{\phi\mathrm{HI_1}} & ... & C_\ell^{\phi g_1} & ... \\ . & & & . & & . & \\ . & & & . & & . & \\ C_\ell^{\mathrm{HI_1 T}} & C_\ell^{\mathrm{HI_1 E}} & C_\ell^{\mathrm{HI_1}\phi} & C_\ell^{\mathrm{HI_1 HI_1}} & ... & C_\ell^{\mathrm{HI_1 g_1}} & ... \\ & & & & & . & \\ . & & . & & . & & \\ C_\ell^{g_1 \mathrm{T}} & C_\ell^{g_1 \mathrm{E}} & C_\ell^{g_1 \phi} & C_\ell^{g_1 \mathrm{HI_1}} & ... & C_\ell^{g_1 g_1} & ... \end{pmatrix}, \tag{5.25}$$

constructed from the auto- and cross-correlation components of the observed angular power spectra (including noise), and where the superscript g_i and H_i denote the components of the galaxy number count and HI IM power spectra in the ith bin.

In the case of multipoles above or below the cut thresholds, this matrix becomes truncated to include only the spectra which are relevant at those multipoles. The different tracers also have different sky fractions, and so the expression in (5.1) generalizes to have a matrix coefficient $f_{sky,ij}$. This $f_{sky,ij}$ is defined so that CMB-CMB auto- and cross-correlation spectra are multiplied by the corresponding $f_{sky,CMB}$, and analogously for HI-HI and g-g spectra. In the case of *cross-survey* correlations C_ℓ^{XY} (e.g. HI-CMB), then the coefficient is determined by $f_{sky,XY} = \min[f_{sky,X}, f_{sky,Y}]$.

Parameter	Fiducial Value
ω_b	0.022383
ω_c	0.12011
H_0	67.32
τ	0.0543
$\ln\left(10^{10} A_s\right)$	3.0448
n_s	0.96605
$B_{g,i}, B_{\mathrm{HI,i}}$	1.0

TABLE 5.2: Fiducial parameter values [29]

5.3.2 Parameter vector

The parameter vector $\boldsymbol{\theta}$ contains the 6 standard ΛCDM cosmological parameters: $\boldsymbol{\theta} = \left\{\omega_b, \omega_c, H_0, \tau, \ln\left(10^{10} A_s\right), n_s\right\}$, as well as nuisance parameters $B_{g,i}$ and $B_{\mathrm{HI,i}}$ that multiply the bias in the ith bin: $b_g(z) \to B_{g,i} b_g(z)$ and $\bar{T}_{\mathrm{HI}}(z) b_{\mathrm{HI}}(z) \to B_{\mathrm{HI,i}} \bar{T}_{\mathrm{HI}}(z) b_{\mathrm{HI}}(z)$, in the respective cases of galaxy number counts and HI IM brightness temperature perturbations for $z \in [z_i, z_{i+1}]$. This allows for the free redshift evolution of the linear bias of each survey. Finally, $\boldsymbol{\theta}$ also contains the parameters associated with the primordial non-Gaussianity: $f_{\mathrm{NL}}, n_{\mathrm{NL}}$ which are defined in a previous section of this chapter (see Section 4.2).

To obtain the final constraints on the primordial non-Gaussianity parameters, we marginalise over the cosmological and nuisance parameters. The assumed fiducial values of the cosmological parameters and nuisance parameters are displayed in Table 5.2, following *Planck* 2018 [29]. The analysis is split into two parts: the first assumes a scale independent f_{NL} which has fiducial value 0, and the second includes the scale-dependence from the running n_{NL} using fiducial values $f_{\mathrm{NL}} = -0.9$ and $n_{\mathrm{NL}} = 0$.

5.4 Results

In this section we report the findings of the analysis, and the constraints in the cases of a scale-independent PNG parameter f_{NL} and for one including the running n_{NL}. First we present a summary of the results of this work, and then a comparison with the results currently in the literature. This section is based on the recently-published work [115].
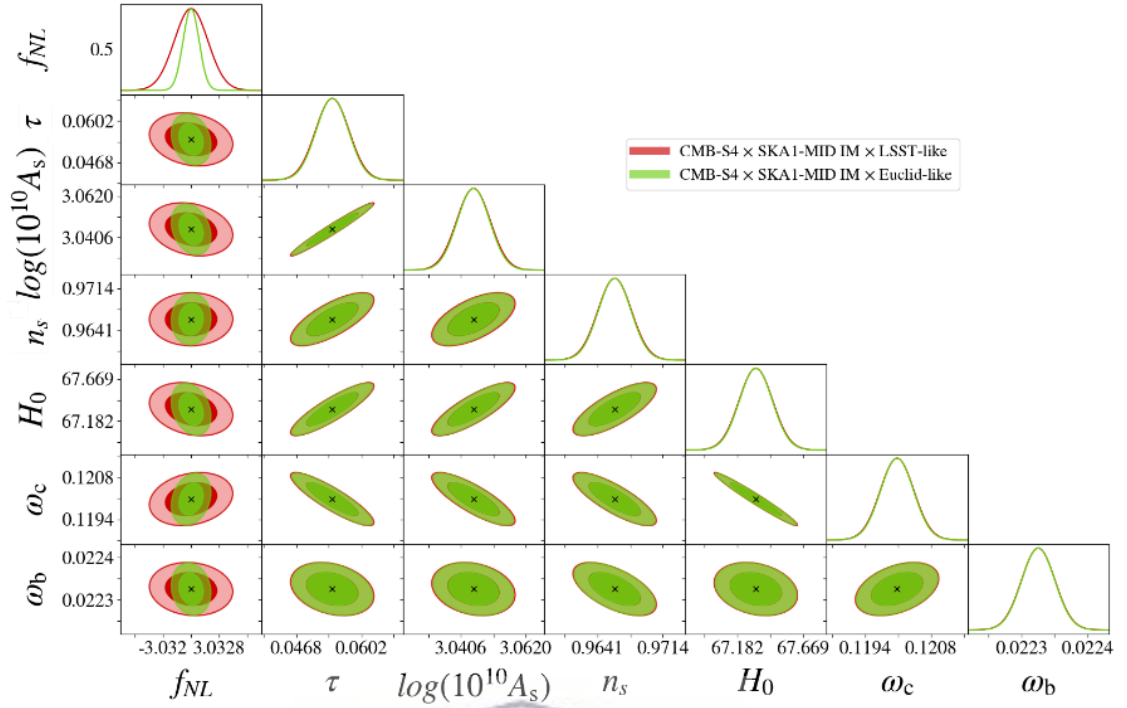
FIGURE 5.4: Triangle plot showing uncertainties on $f_{\rm NL}$ and the cosmological parameters for the case of multiple tracers. In red: CMB-S4 × SKA1-MID IM × LSST-like with respective $\ell_{min} = [30, 5, 20]$ and in green: CMB-S4 × SKA1-MID × Euclid-like with respective $\ell_{\min} = [30, 5, 10]$.

5.4.1 $f_{\rm NL}$ model of PNG

The uncertainties for this model from single surveys, with the assumed minimum monopole, are:

$$\sigma\left(f_{\rm NL}\right) \simeq \begin{cases} 2.1 & {\rm SKA1}\ (\ell_{\min} = 5)\,, \\ 2.3 & {\rm Euclid\text{-}like}\ (\ell_{\min} = 10)\,, \\ 16.2 & {\rm LSST\text{-}like}\ (\ell_{\min} = 20)\,. \end{cases} \qquad (5.26)$$

Once CMB lensing from CMB-S4 with $\ell_{\min} = 30$ is included with each of the other surveys, taking the smaller of the sky areas as the overlap area, the errors decrease to:

$$\sigma\left(f_{\rm NL}\right) \simeq \begin{cases} 1.6 & {\rm SKA1} \times {\rm CMB\text{-}S4}\,, \\ 1.8 & {\rm Euclid\text{-}like} \times {\rm CMB\text{-}S4}\,, \\ 10.5 & {\rm LSST\text{-}like} \times {\rm CMB\text{-}S4}\,. \end{cases} \qquad (5.27)$$

For the combination between only intensity mapping and number counts, the uncertainties obtained using the same ℓ_{min} values as above, taking the smaller sky area as the

overlap area, are:

$$\sigma\left(f_{\mathrm{NL}}\right) \simeq \begin{cases} 0.96 & \text{SKA1} \times \text{Euclid-like}\,, \\ 1.6 & \text{SKA1} \times \text{LSST-like}\,. \end{cases} \tag{5.28}$$

Once all three tracers are included, the tightest constraints obtained are:

$$\sigma\left(f_{\mathrm{NL}}\right) \simeq \begin{cases} 0.90 & \text{SKA1} \times \text{Euclid-like} \times \text{CMB-S4}\,, \\ 1.4 & \text{SKA1} \times \text{LSST-like} \times \text{CMB-S4}\,. \end{cases} \tag{5.29}$$

Recall that these results are marginalised over the uncertainties in the standard cosmological parameters. A full triangle plot of the uncertainties on the cosmological parameters and f_{NL} is shown in Fig. 5.4 for the cases including 3 tracers.

In addition to the different feasible minimum multipoles of the different experimental configurations described in Section 5.2, we consider the uncertainties in f_{NL} by changing the $\ell_{\min}$ for all of the experiments. These results are presented in figure 5.5.

In particular, if we consider the optimistic case where the minimum multipoles extend to 2 for all three tracers, this yields the following constraints for the multi-tracer cases:

$$\sigma\left(f_{\mathrm{NL}}\right) \simeq \begin{cases} 0.47 & \text{SKA1} \times \text{Euclid-like} \times \text{CMB-S4}\,, \\ 1.0 & \text{SKA1} \times \text{LSST-like} \times \text{CMB-S4}\,. \end{cases} \tag{5.30}$$

5.4.2 f_{NL}, n_{NL} model of PNG

We now consider the constraints for the two-parameter model (4.3) with a running of f_{NL}, using the same specifications as in (5.26)–(5.29). In figure 5.6, we show the marginalized uncertainties on the 2-dimensional f_{NL}-n_{NL} parameter space.

$$\sigma\left(n_{\mathrm{NL}}\right) \simeq \begin{cases} 2.7 & \text{SKA1} \left(\ell_{\min} = 5\right)\,, \\ 0.35 & \text{Euclid-like} \left(\ell_{\min} = 10\right)\,, \\ 0.37 & \text{LSST-like} \left(\ell_{\min} = 20\right)\,. \end{cases} \tag{5.31}$$
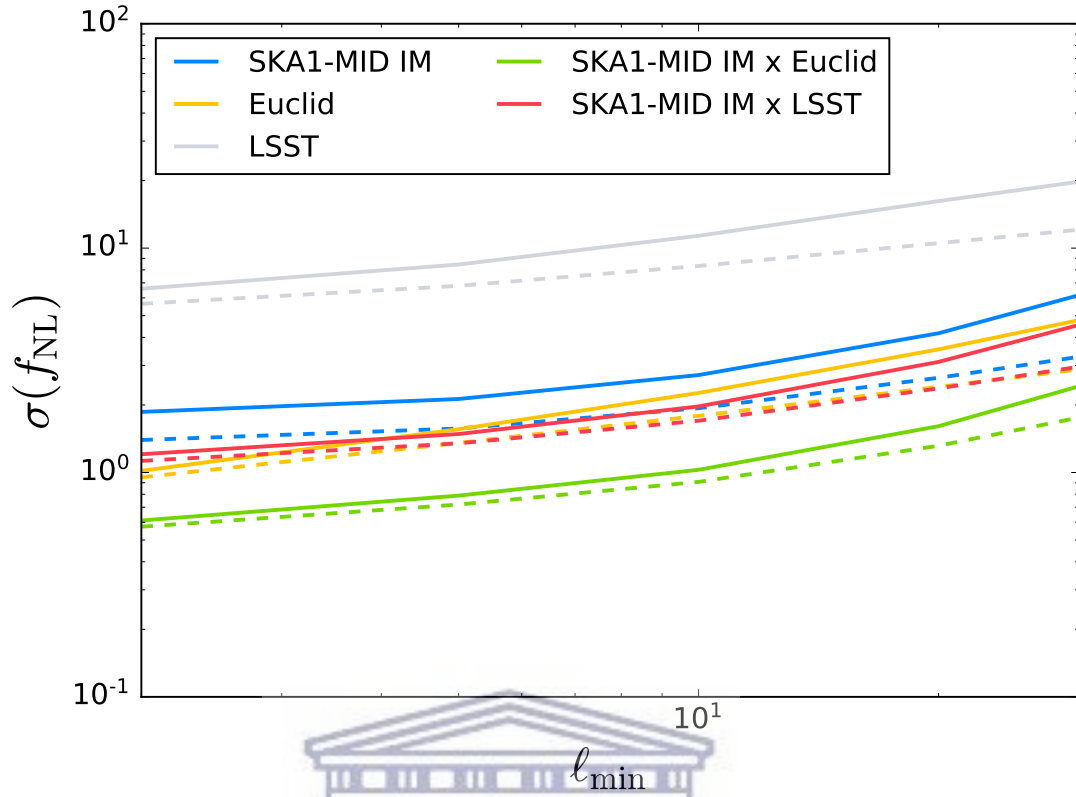
FIGURE 5.5: Marginalized uncertainties on f_{NL} as function of the minimum multipole ℓ_{min} of the LSS tracer. Solid curves correspond to LSS experiment without CMB: SKA1-MID IM (blue), Euclid-like (yellow), and LSST-like (grey), and the combinations SKA1 IM $\times$ Euclid-like (green) and LSST-like (red). Dashed lines correspond to the inclusion of CMB-S4 lensing ($\ell_{min} = 30$).

For the case of two tracers, where we have now included with the above surveys the CMB lensing from CMB-S4 with $\ell_{min} = 30$, the errors decrease to:

$$\sigma\left(n_{NL}\right) \simeq \begin{cases} 1.4 & \text{SKA1} \times \text{CMB-S4}\,, \\ 0.24 & \text{Euclid-like} \times \text{CMB-S4}\,, \\ 0.32 & \text{LSST-like} \times \text{CMB-S4}\,. \end{cases} \tag{5.32}$$

For the combination between intensity and number counts, the uncertainties obtained are:

$$\sigma\left(n_{NL}\right) \simeq \begin{cases} 0.13 & \text{SKA1} \times \text{Euclid-like}\,, \\ 0.24 & \text{SKA1} \times \text{LSST-like}\,. \end{cases} \tag{5.33}$$
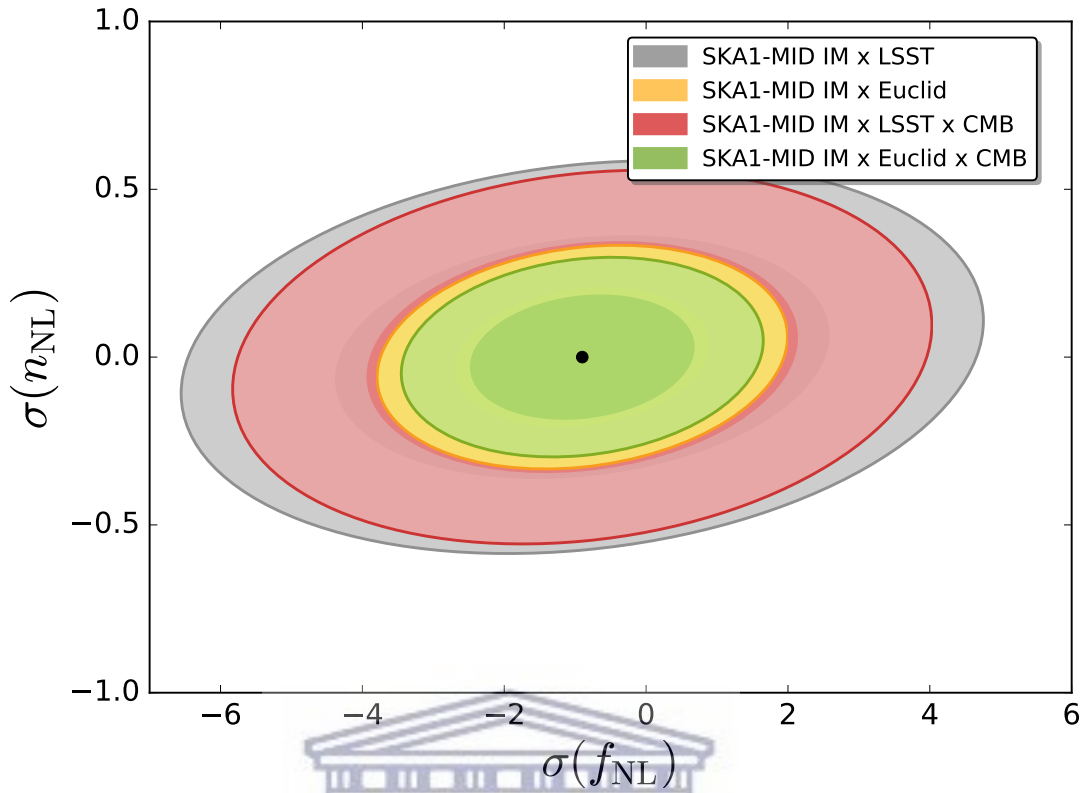
FIGURE 5.6: Marginalized 2-dimensional constraint plots for f_{NL} versus n_{NL} in the case of $\ell_{min} = 5$, 10, 30 for HI IM, galaxy number counts, and CMB respectively. The multi-tracer combinations are: SKA1 $\times$ Euclid-like (yellow), SKA1 $\times$ LSST-like (grey), CMB $\times$ SKA1 $\times$ Euclid-like (green), and CMB $\times$ SKA1 $\times$ LSST-like (red).

Once all three tracers are included, the tightest constraints obtained are:

$$\sigma\left(n_{NL}\right) \simeq \begin{cases} 0.12 & \text{SKA1} \times \text{Euclid-like} \times \text{CMB-S4}, \\ 0.22 & \text{SKA1} \times \text{LSST-like} \times \text{CMB-S4}. \end{cases} \tag{5.34}$$

The results from this model show that the uncertainties on f_{NL} degrade by $\sim 20\%$ on average, compared to the case without running, which indicates a weak degeneracy between the two parameters.

5.4.3 Comparison with other results on $\sigma(f_{NL})$

In this subsection we investigate the differences between our findings and uncertainties on f_{NL} derived in the literature. As stated before, in this work we consistently make use of the CMB convention to define f_{NL}. In the few cases where other works make use

of the alternate LSS convention, we quote here the relevant constraints modified to be consistent with the CMB convention (4.8) which we use.

In [54] and [55] the case of LSST-like and SKAI-MID IM is examined (without using CMB-S4), giving uncertainties down to ~ 0.31 for the multi-tracer case. They use a greater number of bins with smaller width for the SKAI-MID IM survey: 100 bins with equal co-moving width, while we use 27 such bins. In addition, 9 bins are used for LSST-like, with widths chosen to ensure equal source density, as opposed to our 10 fixed-width bins. They use a multipole range $2 \gtrsim \ell \gtrsim 500$ for both tracers and assume larger sky fractions: 0.5 for LSST-like and 0.75 for SKA1, with the overlap taken as 0.4, which also exceeds ours. Their LSST-like redshift distribution is normalized to a slightly more pessimistic 40 sources/arcmin^2, versus our 48 sources/arcmin^2 (according to [81]) which results in a slightly lower shot noise. In summary, their greater sky area and smaller $\ell_{\min}$ are the main reasons for their more optimistic constraints.

In [58] there is a multi-tracer analysis for Euclid-like and SKA1-MID IM surveys. Their results give $0.72 \leq \sigma\left(f_{\mathrm{NL}}\right) \leq 1.05$, depending on (a) the maximum multipole chosen ($\ell_{\max} = 60$ or $\ell_{\max} = 300$), and (b) the sky overlap (50% or 100%). Their multipole range for all tracers extends down to $\ell_{\min} = 2$. They also consider a LSST-like survey with a survey area equal to that of the entire SKA1-MID IM survey. They obtain the multi-tracer result $\sigma\left(f_{\mathrm{NL}}\right) \simeq 0.61$ for $\ell_{\max} = 300$, which is lower than ours. Considering that the effect of f_{NL} is captured only on larger scales, the difference in $\ell_{\max}$ should have a negligible effect on the final uncertainties. There are 20 bins for both surveys, chosen so that there are equal number counts of Euclid-like sources in each. The sky fraction in case (i) of 50% overlap (corresponding to an overlapping sky fraction 0.18) is smaller than our shared sky fraction of 0.36 for SKA1-MID IM and Euclid-like surveys. However, the SKA1 sky fraction used in the three cases is 0.72, which is larger than our 0.48 (according to [77]). In case (iii) the LSST-like sky fraction is also chosen as 0.72, larger than our sky fraction for LSST-like of ~ 0.33 (according to [81]). The bias fitting functions used are the same as ours, and the same kind of nuisance parameters are introduced. The main cause of the difference in results from ours is again the greater sky area and smaller $\ell_{\min}$ that they assumed.

In [96] the case of LSST-like clustering and CMB-S4 lensing in cross correlation is investigated. The uncertainties found are $\sigma\left(f_{\mathrm{NL}}\right) \simeq 0.4$ or $\sigma\left(f_{\mathrm{NL}}\right) \simeq 1.0$ for the cases

where the minimum multipole for both tracers is either 2 or 20, respectively. The galaxy redshift distribution is split into 6 bins, extending over a larger redshift range ($0 < z < 7$) than ours and assuming a redshift distribution normalized to 50 sources/arcmin^2 over the part of the redshift range that is the same as ours. The sky fractions used to obtain these results are 0.5 for CMB and LSST, assuming 100% overlap. Their bias for LSST is calculated according to the fiducial model $b(z) = 1 + z$ as opposed to the one we use: $b(z) = 0.95/D(z)$. Once again, the greater sky area and smaller $\ell_{\min}$ that they assumed produce more optimistic constraints than ours. The larger redshift range that they considered is not as important.

Note that the fact that our results for LSST-like are weaker than the uncertainties for Euclid-like and also weaker than the uncertainties in the literature is mainly due to the sky fraction assumed according to [81] and not for the smaller redshift range considered.

In light of the differences in assumptions made in the literature compared to this work, it is not unexpected that our constraints are not consistently tighter than those from previous investigations. However, it must be stressed that our constraints use conservative estimates and the most up-to-date specifications for the surveys involved.
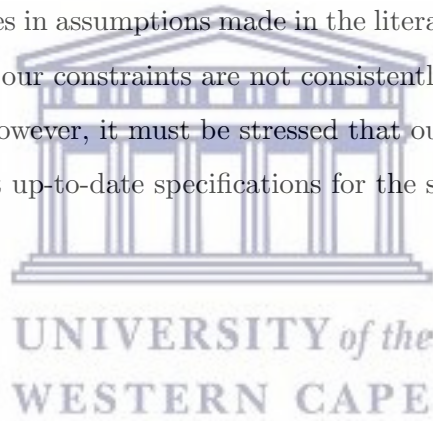
Chapter 6

Conclusion and future work

6.1 Summary of main results and derivations

In Chapter 2 we introduce the two-point correlation function and angular power spectrum. We then rederive expressions for the angular harmonic coefficients, as well as a series of useful relations between the two-point correlation function, angular power spectrum and 3D power spectrum. Following this, we relate the density perturbation to the primordial curvature perturbation by defining various transfer functions and describing their normalizations. This allows us to relate the C_ℓ of the angular power spectrum to the primordial curvature power spectrum $\mathcal{P}_\zeta$, using angular transfer functions Δ_ℓ. Finally, we take into account the effect of an observational window function on the angular power spectrum.

In Chapter 3 we continue to include observational effects to make the expression for the angular power spectrum more realistic. We begin by carefully defining the measured fluctuations in galaxy number counts and redefining the angular power spectrum accordingly. Using these definitions, we derive expressions for the angular transfer functions of two components of the newly-defined angular power spectrum, namely those associated with the comoving density and redshift space distortions. We then examine the distortions to the luminosity distance, rederiving the photon transport equation and establishing the framework which allows us to describe the effect from making observations on the past light cone. Then we rederive the relationship between the measured

100

galaxy fluctuations at the observer and those at the source, as well as the resulting expressions for these observational effects which are used by `CAMB` to numerically calculate the observed angular power spectrum. In addition, we describe the particular angular power spectra associated with HI intensity mapping and CMB lensing observations.

In Chapter 4 we introduce the primordial non-Gaussianity parameter f_{NL} and the associated running index n_{NL} and we discuss the motivation for the choice of surveys to constrain them. In particular, using the formalism of the peak-background split, we describe the scale-dependent halo bias that arises in the angular power spectra of large-scale structure due to the presence of primordial non-Gaussianity.

In Chapter 5 we describe the details of the surveys used to calculate constraints and outline the associated methodology, namely the Fisher formalism, and how it can be used in the case of multiple tracers. Finally, we present the results from single- and multi-tracer approaches, and discuss the findings in the context of the existing results concerning $\sigma(f_{NL})$ in the literature.

6.2 Major findings and future work

We have investigated the measurement of the effect of local primordial non-Gaussianity on ultra large-scale perturbations and shown the effectiveness of the use of up to three tracers of the cosmic matter density field in this regard. In particular, our forecast predicts that the combination of an SKA1-MID HI intensity mapping survey, a photometric galaxy survey (Euclid- or LSST-like) and CMB lensing from CMB-S4, could reach uncertainties for primordial non-Gaussianity parameters of $\sigma(f_{NL}) \lesssim 0.9$ and $\sigma(n_{NL}) \lesssim 0.2$ in the conservative case. We also note the particular importance that the inclusion of CMB lensing information has in further improving the constraints on f_{NL}, through the cross-correlation with intensity or number counts. Although the constraints forecast here are not conclusively better than similar results in the existing literature, in the context of the assumptions made, the results presented here are more robust and realistic.

Because the effect of the PNG parameters is most prominent on the very large scales, the constraints depend strongly on the ℓ_{min} and f_{sky} considered in the analysis. We assumed the following minimum multipoles and sky areas for each experiment, according to the latest specifications for each survey:

- $\ell_{\min} = 5,\ \Omega = 20\,000\,\mathrm{deg}^2$ – SKA1 [77]

- $\ell_{\min} = 10,\ \Omega = 15\,000\,\mathrm{deg}^2$ – Euclid-like [80]

- $\ell_{\min} = 20,\ \Omega = 13\,800\,\mathrm{deg}^2$ – LSST-like [81]

- $\ell_{\min} = 30,\ \Omega = 16\,500\,\mathrm{deg}^2$ – CMB-S4 [65]

The uncertainties obtained for local type PNG in the single-tracer cases are $\sigma(f_{\mathrm{NL}}) \simeq 2.1$ for SKA1-MID IM with $\ell_{\min} = 5$, $\sigma(f_{\mathrm{NL}}) \simeq 2.3$ for Euclid-like with $\ell_{\min} = 10$, and $\sigma(f_{\mathrm{NL}}) \simeq 16.2$ for LSST-like with $\ell_{\min} = 20$. The constraints on the running index of f_{NL} in the extended local PNG model, were found to be $\sigma(n_{\mathrm{NL}}) \simeq 2.7,\ 0.35,\ 0.37$ from the respective surveys.

From the combination of two different large-scale structure surveys via the multi-tracer approach, we forecast $\sigma(f_{\mathrm{NL}}) \simeq 0.96\ (1.6)$ for SKA1-MID IM with Euclid-like (LSST-like) and $\sigma(n_{\mathrm{NL}}) \simeq 0.13\ (0.24)$.

When we include CMB lensing information (with $\ell_{\min} = 30$) from a possible CMB-S4 ground-based experiment with a single LSS survey via the multi-tracer approach, we found that the single-tracer errors decrease to $\sigma(f_{\mathrm{NL}}) \simeq 1.6,\ 1.8,\ 10.5$ for SKA1-HI IM, Euclid-like, and LSST-like, respectively.

The tightest uncertainties, from the combination of all three tracers in a multi-tracer analysis, are predicted to be

$$\sigma(f_{\mathrm{NL}}) \simeq 0.90 \text{ and } \sigma(n_{\mathrm{NL}}) \simeq 0.12 \text{ , for SKA1} \times \text{Euclid-like} \times \text{CMB-S4.} \quad (6.1)$$

Replacing Euclid-like with LSST-like, degrades these to $\sigma(f_{\mathrm{NL}}) \simeq 1.4$ and $\sigma(n_{\mathrm{NL}}) \simeq 0.22$.

Since constraints calculated here use the most up-to-date specifications for the surveys involved and more conservative estimates of the minimum multipoles than in the existing literature, it is not unexpected that our constraints are comparatively weaker. We also studied the effect of the chosen minimum multipole on the PNG uncertainties, as shown in Fig. 5.5. In the cases of multiple tracers, the sky overlap area was assumed to be smallest of the sky fractions of the tracers used. In the case of smaller overlaps, the uncertainties will only be mildly negatively affected.

In addition to CMB-S4, we also considered using simulated *Planck*-like data as representative of current CMB measurements. Although a forecast of the corresponding constraints lead to uncertainties on the cosmological parameters compatible with the latest results in [27–29], the improvement in constraints by adding *Planck* to the single-tracer cases was very small. In addition, we tested the possibility of completing the missing first multipoles $2 \leq \ell_{\min} < 30$ in the CMB spectra, but found no further improvement, indicating that the improvements *Planck* made to the single-tracer cases were mainly due to parameter degeneracy with the standard cosmological parameters, rather than the imprint of f_{NL} on the cross-correlation between intensity/number counts and CMB lensing.

In future analyses it may be interesting to consider constraints on different models of primordial non-Gaussianity. For instance, extending the definition of f_{NL} given in (4.2), it is possible to define a higher order g_{NL} parameter such that

$$- \Phi_p = \varphi_G + f_{\mathrm{NL}} \left(\varphi_G^2 - \langle \varphi_G^2 \rangle \right) + g_{\mathrm{NL}} \left(\varphi_G^3 - 3 \langle \varphi_G^2 \rangle \varphi_G \right) \ . \tag{6.2}$$

Another possibility is to include the bispectrum in the analysis and perform a combined forecast using both the bispectrum and power spectrum of the tracers [123–126]. This approach has recently been shown to be effective in constraining the PNG using upcoming radio continuum and optical surveys by up to a factor of ~ 5 better than forecasts from the power spectrum alone [125].

In addition to the three used here, there are many other tracers that have been identified as good candidates to obtain competitive constraints on f_{NL}. Examples include:

- galaxy clustering [116–118],

- cosmic infrared background [119],

- cosmic voids [120]

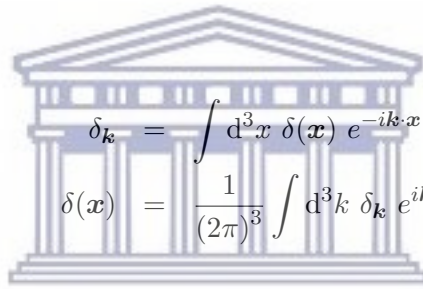- different IM lines, such as Hα, CO and [CII] [121, 122].

In future analyses these could be included to attain tighter constraints on primordial non-Gaussianity parameters.

Appendix A

Special Functions

This appendix contains definitions of special function relations used in the derivations.

Fourier Convention

$$\delta_{\boldsymbol{k}} = \int \mathrm{d}^3x \ \delta(\boldsymbol{x}) \ e^{-i\boldsymbol{k}\cdot\boldsymbol{x}} \tag{A.1}$$

$$\delta(\boldsymbol{x}) = \frac{1}{(2\pi)^3} \int \mathrm{d}^3k \ \delta_{\boldsymbol{k}} \ e^{i\boldsymbol{k}\cdot\boldsymbol{x}} \tag{A.2}$$

Legendre polynomials orthogonality

$$\int_{-1}^{1} \mathrm{d}(\hat{\boldsymbol{k}}\cdot\boldsymbol{n}) \ \mathcal{L}_\ell(\hat{\boldsymbol{k}}\cdot n)\mathcal{L}_{\ell'}(\hat{\boldsymbol{k}}\cdot n) = \frac{2}{2\ell+1}\delta_{\ell\ell'} \tag{A.3}$$

Spherical Harmonic expansion of Legendre Polynomials

$$\mathcal{L}_\ell(\hat{\boldsymbol{k}}\cdot\boldsymbol{n}) = \frac{4\pi}{2\ell+1} \sum_{m=-\ell}^{\ell} Y_{\ell m}(\boldsymbol{n})Y_{\ell m}^*(\hat{\boldsymbol{k}}) \tag{A.4}$$

Spherical harmonics orthonormality

$$\int \mathrm{d}\Omega_{\boldsymbol{n}} \ Y_{\ell m}(\boldsymbol{n})Y_{\ell' m'}^*(\boldsymbol{n}) = \delta_{\ell\ell'}\delta_{mm'} \tag{A.5}$$

Plane wave expansion of the exponential function

$$e^{i\boldsymbol{k}\cdot\boldsymbol{r}} = \sum_{\ell=0}^{\infty}(2\ell+1)i^\ell \mathcal{L}_\ell(\hat{\boldsymbol{k}}\cdot\hat{\boldsymbol{r}})j_\ell(kr) \ , \tag{A.6}$$

where $\mathcal{L}_\ell$ are the Legendre polynomials, and j_ℓ the spherical Bessel functions.

104

Appendix B

Volume perturbation calculation

This appendix, based on the work of [18], provides details of the calculation used to obtain the terms of the volume perturbation in Chapter 3.

First, we expand the right-hand side of (3.124), using (3.121), (3.123) and (3.127) to obtain

$$
dV = a^3(1 - 2\Phi)\chi^2 \sin\theta_S \left[(1 - \Phi)\frac{d\chi}{dz} - v_n \frac{d\eta}{dz} \right] \left[1 + \frac{\partial\delta\theta}{\partial\theta} + \frac{\partial\delta\phi}{\partial\phi} \right] dz d\theta_O d\phi_O , \quad \text{(B.1)}
$$

which, to first order, gives [18, 62]

$$
dV = a^3(1 - 2\Phi) \left[\frac{d\chi}{dz}\chi^2 \sin\theta_S \left(1 + \frac{\partial\delta\theta}{\partial\theta} + \frac{\partial\delta\phi}{\partial\phi} \right) - \left(\Phi\frac{d\bar\chi}{d\bar z} + v_n \frac{d\eta}{dz} \right) \bar\chi^2 \sin\theta_O \right] dz d\theta_O d\phi_O ,
$$
$$\text{(B.2)}$$

where v_n is the radial component of the velocity, $d\chi/dz$ is the measurement of the change in the comoving distance with redshift along the *perturbed* photon geodesic and we reserve overbars for background quantities.

Hence

$$
\begin{aligned}
\frac{d\chi}{dz} &= \frac{d\bar\chi}{d\bar z} + \frac{d\delta\chi}{d\bar z} - \frac{d\delta z}{d\bar z}\frac{\bar\chi}{\bar z} \\
&= \frac{a}{\mathcal{H}} + \frac{d\eta}{d\bar z}\left(\frac{d\delta\chi}{d\lambda} - \frac{d\delta z}{d\lambda}\frac{a}{\mathcal{H}} \right) \\
&= \frac{a}{\mathcal{H}}\left(1 - \frac{d\delta\chi}{d\lambda} + \frac{d\delta z}{d\lambda}\frac{a}{\mathcal{H}} \right) ,
\end{aligned}
\qquad \text{(B.3)}
$$

where $d\lambda$ is equivalent to $d\eta$ for derivatives along the photon geodesic and the derivatives $d\bar{\chi}/d\bar{z} = -d\eta/d\bar{z} = a/\mathcal{H}$, valid at first order, have been used.

Thus, keeping the calculation at first order, we can multiply out the expression for $\mathcal{V}$ (see (3.128)), using (B.2) to obtain

$$
\begin{aligned}
\mathcal{V} &= \frac{a^4}{\mathcal{H}} \left[\chi^2 \sin\theta_S \left(1 + \frac{\partial\delta\theta}{\partial\theta} + \frac{\partial\delta\phi}{\partial\phi} \right) + \bar{\chi}^2 \sin\theta_O \left(\frac{a}{\mathcal{H}} \frac{d\delta z}{d\lambda} - \frac{d\delta\chi}{d\lambda} \right) \right. \\
&\quad \left. - \frac{\mathcal{H}}{a} \left(\Phi \frac{d\bar{\chi}}{d\bar{z}} + v_{\boldsymbol{n}} \frac{d\eta}{dz} \right) \bar{\chi}^2 \sin\theta_O - 2\Phi\bar{\chi}^2 \sin\theta_O \right] \\
&= \frac{a^4}{\mathcal{H}} \bar{\chi}^2 \sin\theta_O \left[\frac{\bar{\chi}^2 + 2\bar{\chi}\delta\chi}{\bar{\chi}^2} \frac{\sin\theta_O + \cos\theta_O\delta\theta}{sin\theta_O} \left(1 + \frac{\partial\delta\theta}{\partial\theta} + \frac{\partial\delta\phi}{\partial\phi} \right) \right. \\
&\quad \left. + \left(\frac{a}{\mathcal{H}} \frac{d\delta z}{d\lambda} - \frac{d\delta\chi}{d\lambda} \right) - \Phi + v_{\boldsymbol{n}} - 2\Phi \right] \\
&= \frac{a^4}{\mathcal{H}} \bar{\chi}^2 \sin\theta_O \left[1 + 2\frac{\delta\chi}{\bar{\chi}} + \left(\cot\theta_O + \frac{\partial}{\partial\theta} \right)\delta\theta + \frac{\partial\delta\phi}{\partial\phi} \right. \\
&\quad \left. + \frac{a}{\mathcal{H}} \frac{d\delta z}{d\lambda} - \frac{d\delta\chi}{d\lambda} - 3\Phi + \boldsymbol{v}\cdot\boldsymbol{n} \right] ,
\end{aligned}
\tag{B.4}
$$

which (by (3.129)) gives [18, 62]

$$
\begin{aligned}
\frac{\delta V(\boldsymbol{n}, z)}{\bar{V}(z)} &= -3\Phi + \left(\cot\theta_O + \frac{\partial}{\partial\theta_O} \right)\delta\theta + \frac{\partial\delta\phi}{\partial\phi} + \boldsymbol{v}\cdot\boldsymbol{n} + 2\frac{\delta\chi}{\bar{\chi}} - \frac{\partial\delta\chi}{\partial\lambda} \\
&\quad + \frac{1}{\mathcal{H}(1+\bar{z})} \frac{\partial\delta z}{\partial\lambda} - \left(-4 + \frac{2}{\bar{\chi}\mathcal{H}} + \frac{\mathcal{H}'}{\mathcal{H}^2} \right) \frac{\delta z}{(1+\bar{z})} .
\end{aligned}
\tag{B.5}
$$

The $\delta\theta$, $\delta\phi$ and $\delta\chi$ can now be calculated by solving the geodesic equation for a perturbed Friedmann universe. The deviation vector defined earlier (see (3.49)) is useful here, because in spherical coordinates its components determine $\delta\theta$, $\delta\phi$ and $\delta\chi$. In order to relate the space-time coordinates and the affine parameter, we make use of

$$
\frac{dx^\mu}{d\eta} = \frac{dx^\mu}{d\lambda} \frac{d\lambda}{d\eta} = \frac{k^\mu}{k^0} ,
\tag{B.6}
$$

where we have used the wave vector k^μ tangent to the geodesic from (3.46). In the case of the conformal time component, this leads to

$$
x^0 = \int_{\eta_S}^{\eta_O} d\eta = \eta_O - \eta_S .
\tag{B.7}
$$

For the spatial components, writing k^μ using a first-order perturbation, we obtain

$$
\frac{dx^i}{d\eta} = \frac{\bar{k}^i + \delta k^i}{\bar{k}^0 + \delta k^0} = -n^i + n^i \delta k^0 + \delta k^i .
\tag{B.8}
$$

Integrating, we obtain

$$x^i = \int_{\eta_S}^{\eta_O} d\eta(-n^i + \delta k^i + n^i \delta k^0) \,. \tag{B.9}$$

At first order $d\eta = d\lambda$, and thus

$$x^i = -n^i(\eta_O - \eta_S) + \int_{\lambda_S}^{\lambda_O} d\lambda(\delta k^i + n^i \delta k^0) \,. \tag{B.10}$$

We subtract the background from (B.10) to obtain

$$x^i - \bar{x}^i = \delta x_O^i - \delta x_S^i = \int_{\lambda_S}^{\lambda_O} d\lambda(\delta k^i + n^i \delta k^0) \,, \tag{B.11}$$

where we have $\delta x_O^i = 0$. Thus, at first order and taking $\delta x_S^i \equiv \delta x^i$, we can write

$$\delta x^i = \int_{\lambda_O}^{\lambda_S} d\tilde{\lambda} \left(\delta k^i + n^i \delta k^0 \right) \,, \tag{B.12}$$

where the background components of $\bar{k}^\mu$ are described in Section 3.3.5.

We may then use the components (3.110) and (3.111) of the geodesic equation, with the corresponding affine parameter bounds $\lambda_O = 0$ and $\lambda_S = \lambda$, to show that

$$\delta k^0 = -2\Phi + 2\int_0^\lambda d\tilde{\lambda}\Phi' \,, \tag{B.13}$$

and

$$\delta k^i = -2n^i\Phi - 2\int_0^\lambda d\tilde{\lambda}\partial^i\Phi \,. \tag{B.14}$$

We may simplify the latter further using $\partial^i = n^i(n^j\partial_j) + \nabla_\perp^i$ and $\frac{\partial}{\partial\lambda} = \frac{\partial}{\partial\eta} - n^j\partial_j$ (compare (3.140)). Thus we have:

$$\delta k^i = -2n^i\Phi - 2\int_0^\lambda d\tilde{\lambda} \left[n^i \left(\frac{\partial}{\partial\eta} - \frac{\partial}{\partial\lambda} \right) \Phi + \nabla_\perp^i\Phi \right] \,, \tag{B.15}$$

and so we obtain

$$\delta k^i = -2n^i\int_0^\lambda d\tilde{\lambda}\Phi' - 2\int_0^\lambda d\tilde{\lambda}\,\tilde{\nabla}_\perp^i\Phi \,. \tag{B.16}$$

By substituting (B.16) in (B.12) we obtain

$$\delta x^i = -2n^i\int_0^\lambda d\tilde{\lambda}\Phi - 2\int_0^\lambda d\tilde{\lambda}'\int_0^{\tilde{\lambda}'} d\tilde{\lambda}\tilde{\nabla}_\perp^i\Phi \,, \tag{B.17}$$

where we can reverse the order of integration in the second term (as described in general

in [1]) while preserving the area covered in the $\tilde{\lambda}$-$\tilde{\lambda}'$ plane, to make the integral over $\tilde{\lambda}$ trivial, finally obtaining

$$\delta x^i = -2n^i \int_0^\lambda \mathrm{d}\tilde{\lambda}\,\Phi - 2\int_0^\lambda \mathrm{d}\tilde{\lambda}\left(\lambda - \tilde{\lambda}\right)\tilde{\nabla}_\perp^{\;i}\Phi\,. \tag{B.18}$$

We can also separate (B.18) into parallel and perpendicular components as

$$\delta x^i = \delta x_\parallel^{\;i} + \delta x_\perp^{\;i}\,, \tag{B.19}$$

where

$$\delta x_\parallel^{\;i} = -2n^i\int_0^\lambda \mathrm{d}\tilde{\lambda}\,\Phi,\qquad \delta x_\perp^{\;i} = -2\int_0^\lambda \mathrm{d}\tilde{\lambda}\left(\lambda - \tilde{\lambda}\right)\tilde{\nabla}_\perp^{\;i}\Phi\,. \tag{B.20}$$

We can now obtain $\delta\theta$, $\delta\phi$ and $\delta\chi$ by projecting $\delta x_\perp^{\;i}$ and $\delta x_\parallel^{\;i}$ onto each of the unit vectors $e_{\theta i}$, $e_{\phi i}$ and $e_{\chi i}$, respectively. These unit vectors have the following properties [18]:

$$n^i e_{\theta i} = 0\,,\qquad n^i e_{\phi i} = 0\,,\qquad n^i e_{\chi i} = 1\,, \tag{B.21}$$

and

$$e_{\theta i}\tilde{\nabla}_\perp^{\;i} = \frac{1}{\tilde{\chi}}\tilde{\partial}_{\theta_\mathrm{O}}\,,\qquad e_{\phi i}\tilde{\nabla}_\perp^{\;i} = \frac{1}{\tilde{\chi}\sin\theta_\mathrm{O}}\tilde{\partial}_{\phi_\mathrm{O}}\,. \tag{B.22}$$

Therefore, to first order we have:

$$\delta\chi = \delta x_\parallel^{\;i} e_{\chi i} = -2\int_0^\lambda \mathrm{d}\tilde{\lambda}\,\Phi\,,$$

$$\delta\theta = \frac{1}{\bar{\chi}}\delta x_\perp^{\;i} e_{\theta i} = -2\int_0^\lambda \mathrm{d}\tilde{\lambda}\,\frac{\chi - \tilde{\chi}}{\bar{\chi}\tilde{\chi}}\,\tilde{\partial}_{\theta_\mathrm{O}}\Phi\,,$$

$$\delta\phi = \frac{1}{\bar{\chi}\sin\theta_\mathrm{O}}\delta x_\perp^{\;i} e_{\phi i} = -\frac{2}{\sin^2\theta_\mathrm{O}}\int_0^\lambda \mathrm{d}\tilde{\lambda}\,\frac{\chi - \tilde{\chi}}{\bar{\chi}\tilde{\chi}}\,\tilde{\partial}_{\phi_\mathrm{O}}\Phi\,. \tag{B.23}$$

The redshift contribution $\partial\delta z/\partial\lambda$ can be obtained by taking the derivative of (3.115) with respect to the affine parameter λ to give:

$$\frac{a}{\mathcal{H}}\frac{\partial\delta z}{\partial\lambda} = \Phi - \boldsymbol{v}\cdot\boldsymbol{n} - 2\int_0^\lambda \mathrm{d}\hat{\lambda}\,\Phi'(\hat{\lambda}) - \frac{1}{\mathcal{H}}\left(\frac{\partial\Phi}{\partial\lambda} - \frac{\partial\boldsymbol{v}\cdot\boldsymbol{n}}{\partial\lambda} - 2\Phi'\right) \tag{B.24}$$

Then, by substituting this result and (B.23) into (B.5), we can show that the volume fluctuation becomes (3.131), which agrees with [18, 45, 62] (once the difference in convention are included). The sign of the eventual lensing term from this calculation disagrees, but the correct sign is adopted from (3.131) on.

Bibliography

[1] S. Dodelson, *Modern Cosmology*. Academic Press, Amsterdam, 2003.

[2] F. R. G. Ellis, R. Maartens, and A. H. M. MacCallum, *Relativistic cosmology*. Cambridge University Press, Cambridge, 2012.

[3] A. K. Singal, *Horizon, homogeneity and flatness problems ? do their resolutions really depend upon inflation?*, in *Proceedings, National Conference on Current Issues in Cosmology, Astrophysics and High Energy Physics (CICAHEP): Dibrugarh, India, November 2-5, 2015*, (Dibrugarh, India), pp. 94–99, Dibrugarh Univ., Dibrugarh Univ., 2016. arXiv:1603.01539.

[4] S. S. Bayin, *Is the Universe Flat?*, arXiv:1309.5815.

[5] J.-P. Uzan, *The big-bang theory: construction, evolution and status*, 2016. arXiv:1606.06112.

[6] S. Chongchitnan, *Reheating in an inflation model parametrized by the Hubble radius*, arXiv:1709.03482.

[7] J. Martin, C. Ringeval, R. Trotta, and V. Vennin, *The Best Inflationary Models After Planck*, JCAP **1403** (2014) 039, [arXiv:1312.3529].

[8] W. J. Handley, S. D. Brechet, A. N. Lasenby, and M. P. Hobson, *Kinetic Initial Conditions for Inflation*, Phys. Rev. **D89** (2014), no. 6 063505, [arXiv:1401.2253].

[9] J. W. Fowler et al., *CMB observations with a compact heterogeneous 150-GHz interferometer in Chile*, Astrophys. J. Suppl. **156** (2005) 1, [astro-ph/0403137].

[10] J. Borrill, *The challenge of data analysis for future CMB observations*, AIP Conf. Proc. **476** (1999), no. 1 277–282, [astro-ph/9903204].

[11] **WMAP** Collaboration, C. L. Bennett et al., *Nine-Year Wilkinson Microwave Anisotropy Probe (WMAP) Observations: Final Maps and Results*, *Astrophys. J. Suppl.* **208** (2013) 20, [arXiv:1212.5225].

[12] **Planck** Collaboration, P. A. R. Ade et al., *Planck 2015 results. XIII. Cosmological parameters*, *Astron. Astrophys.* **594** (2016) A13, [arXiv:1502.01589].

[13] J. Miralda-Escude, *The dark age of the universe*, *Science* **300** (2003) 1904–1909, [astro-ph/0307396].

[14] Lucian Dorneanu, *Nuclear chemistry of the big bang*, 2007. [Online; accessed February 28, 2018].

[15] V. Springel, C. S. Frenk, and S. D. M. White, *The large-scale structure of the Universe*, *Nature* **440** (2006) 1137, [astro-ph/0604561].

[16] D. H. Lyth and A. Riotto, *Particle physics models of inflation and the cosmological density perturbation*, *Phys. Rept.* **314** (1999) 1–146, [hep-ph/9807278].

[17] N. Yoshida, *Structure Formation in the Early Universe*, arXiv:0906.4372.

[18] C. Bonvin and R. Durrer, *What galaxy surveys really measure*, *Phys. Rev.* **D84** (2011) 063505, [arXiv:1105.5280].

[19] V. Tansella, G. Jelic-Cizmek, C. Bonvin, and R. Durrer, *COFFE: a code for the full-sky relativistic galaxy correlation function*, arXiv:1806.11090.

[20] P. Schneider, *Weak gravitational lensing*, in *Proceedings, 33rd Advanced Saas Fee Course on Gravitational Lensing: Strong, Weak, and Micro: Les Diablerets, Switzerland, April 7-12, 2003*, pp. 269–451, 2006. astro-ph/0509252.

[21] S. M. Carroll, *Lecture notes on general relativity*, gr-qc/9712019.

[22] K. Liao, Z. Li, G.-J. Wang, and X.-L. Fan, *Test of the FLRW metric and curvature with strong lens time delays*, *Astrophys. J.* **839** (2017), no. 2 70, [arXiv:1704.04329].

[23] P. Peter, J.-P. Uzan, *Primordial Cosmology*. Oxford University Press, Oxford, 2009.

[24] **Supernova Search Team** Collaboration, A. G. Riess et al., *Observational evidence from supernovae for an accelerating universe and a cosmological constant*, *Astron. J.* **116** (1998) 1009–1038, [astro-ph/9805201].

[25] N. G. Busca et al., *Baryon Acoustic Oscillations in the Ly-α forest of BOSS quasars*, *Astron. Astrophys.* **552** (2013) A96, [arXiv:1211.2616].

[26] **DES** Collaboration, T. Abbott et al., *The dark energy survey*, astro-ph/0510346.

[27] Planck Collaboration, N. Aghanim et al. *Planck 2018 results. VIII. Gravitational lensing*, *arXiv e-prints*, (2018), [arXiv:1807.06210]

[28] Planck Collaboration, Y. Akrami et al. *Planck 2018 results. I. Overview and the cosmological legacy of Planck*, *arXiv e-prints*, (2018), [arXiv:1807.06205]

[29] **Planck** Collaboration, N. Aghanim et al., *Planck 2018 results. VI. Cosmological parameters*, arXiv:1807.06209.

[30] D. W. Hogg, *Distance measures in cosmology*, astro-ph/9905116.

[31] C. Clarkson, O. Umeh, R. Maartens, and R. Durrer, *What is the distance to the CMB?*, *JCAP* **1411** (2014), no. 11 036, [arXiv:1405.7860].

[32] D. Bertacca, *Observed galaxy number counts on the light cone up to second order: III. Magnification bias*, *Class. Quant. Grav.* **32** (2015), no. 19 195011, [arXiv:1409.2024].

[33] L. Sberna and P. Pani, *Nonsingular solutions and instabilities in Einstein-scalar-Gauss-Bonnet cosmology*, *Phys. Rev.* **D96** (2017), no. 12 124022, [arXiv:1708.06371].

[34] L. Amendola and S. Tsujikawa, *Dark energy: theory and observations.* Cambridge University Press, Cambridge, 2010.

[35] R. Durrer, *Cosmological perturbation theory*, *Lect. Notes Phys.* **653** (2004) 31–70, [astro-ph/0402129]. [,31(2004)].

[36] L. Perivolaropoulos, *Consistency of LCDM with Geometric and Dynamical Probes*, *J. Phys. Conf. Ser.* **222** (2010) 012024, [arXiv:1002.3030].

[37] M. J. Hudson and S. J. Turnbull, *The growth rate of cosmic structure from peculiar velocities at low and high redshifts*, Astrophys. J. **751** (2013) L30, [`arXiv:1203.4814`].

[38] E. V. Linder and R. N. Cahn, *Parameterized Beyond-Einstein Growth*, Astropart. Phys. **28** (2007) 481–488, [`astro-ph/0701317`].

[39] A. Hall & C. Bonvin *Measuring cosmic velocities with 21 cm intensity mapping and galaxy redshift survey cross-correlation dipoles*, Phys. Rev. D, **95** (2017), 043530, [`arXiv:1609.09252`]

[40] P. Reimberg, F. Bernardeau, & C. Pitrou *Redshift-space distortions with wide angular separations*, JCAP, **2016** (2016), 048, [`arXiv:1506.06596`]

[41] L. Samushia et al., *The clustering of galaxies in the SDSS-III Baryon Oscillation Spectroscopic Survey: measuring growth rate and geometry with anisotropic clustering*, Mon. Not. Roy. Astron. Soc. **439** (2014), no. 4 3504–3519, [`arXiv:1312.4899`].

[42] D. Duniya, D. Bertacca, and R. Maartens, *Clustering of quintessence on horizon scales and its imprint on HI intensity mapping*, JCAP **1310** (2013) 015, [`arXiv:1305.4509`].

[43] D. G. A. Duniya, D. Bertacca, and R. Maartens, *Probing the imprint of interacting dark energy on very large scales*, Phys. Rev. **D91** (2015) 063530, [`arXiv:1502.06424`].

[44] K. A. Malik, *Cosmological perturbations in an inflationary universe*. PhD thesis, Portsmouth U., 2001. `astro-ph/0101563`.

[45] A. Challinor and A. Lewis, *The linear power spectrum of observed source number counts*, Phys. Rev. **D84** (2011) 043516, [`arXiv:1105.5292`].

[46] K. A. Malik and D. R. Matravers, *A Concise Introduction to Perturbation Theory in Cosmology*, Class. Quant. Grav. **25** (2008) 193001, [`arXiv:0804.3276`].

[47] N. Kaiser, *Clustering in real space and in redshift space*, Mon. Not. Roy. Astron. Soc. **227** (1987), 1–21, [`astro-ph/9307001`].

[48] A. Challinor and A. Lewis, *Weak gravitational lensing of the CMB*, *Phys. Rev.* **429** (2006) no. 1, 1–65, [`astro-ph/0601594`].

[49] C. Bonvin, R. Durrer, and M. A. Gasparini, *Fluctuations of the luminosity distance*, *Phys. Rev.* **D73** (2006) 023523, [`astro-ph/0511183`]. [Erratum: Phys. Rev.D85,029901(2012)].

[50] P. Schneider, J. Ehlers, & E. E. Falco, *Gravitational Lenses.* Springer, Berlin, 1992.

[51] R. A. Fisher, *The Logic of Inductive Inference*, *Journal of the Royal Statistical Society*, **98** (1935)

[52] L. Verde, *Statistical Methods in Cosmology*, *Lecture Notes in Physics, Berlin Springer Verlag*, **800** (2010), 147, [`arXiv:0911.3105`]

[53] M. Tegmark, A. N. Taylor & A. F. Heavens, *Karhunen-Love Eigenvalue Problems in Cosmology: How Should We Tackle Large Data Sets?*, *Astrophys. J.*, **480** (1997), 22, [`astro-ph/9603021`]

[54] D. Alonso, P. Bull, P. G. Ferreira, R. Maartens, & M. G. Santos, *Ultra-large-scale Cosmology in Next-generation Experiments with Single Tracers*, *Astrophys. J.*, **814** (2015), 145, [`arXiv:1505.07596`]

[55] D. Alonso, & P. G. Ferreira, *Constraining ultralarge-scale cosmology with multiple tracers in optical and radio surveys*, *Phys. Rev. D*, **92** (2015), 063525, [`arXiv:1507.03550`]

[56] A. Witzemann, D. Alonso, J. Fonseca, & M. G. Santos, *Simulated multitracer analyses with H I intensity mapping*, *Mon. Not. Roy. Astron. Soc.*, **485** (2019), 5519, []

[57] S. Cunnington, L. Wolz, A. Pourtsidou & D. Bacon, *Impact of Foregrounds on HI Intensity Mapping Cross-Correlations with Optical Surveys*, *Mon. Not. Roy. Astron. Soc.*, (2019), 1847, []

[58] J. Fonseca, S. Camera, M. G. Santos, & R. Maartens, *Hunting Down Horizon-scale Effects with Multi-wavelength Surveys*, *Astrophys. J.*, **812** (2015), L22, [`arXiv:1507.04605`]

[59] A. Hall, C. Bonvin, & A. Challinor, *Testing general relativity with 21-cm intensity mapping*, *Phys. Rev. D*, **87** (2013), 064026, [`arXiv:1212.0728`]

[60] R. Maartens, C. Clarkson, & S. Chen, *The kinematic dipole in galaxy redshift surveys*, *JCAP*, **2018** (2018), 013, [`arXiv:1709.04165`]

[61] M. Bruni, R. Crittenden, K. Koyama, R. Maartens, C. Pitrou, & D. Wands, *Disentangling non-Gaussianity, bias, and general relativistic effects in the galaxy distribution*, *Phys. Rev. D*, **85** (2012), 041301, []

[62] C. Bonvin, *Isolating relativistic effects in large-scale structure*, *Class. Quant. Grav.* **31** (2014), no. 23 234002, [`arXiv:1409.2224`].

[63] D. Jeong, F. Schmidt, and C. M. Hirata, *Large-scale clustering of galaxies in general relativity*, *Phys. Rev.* **D85** (2012) 023504, [`arXiv:1107.5427`].

[64] J. Yoo, A. L. Fitzpatrick, & M. Zaldarriaga, *New perspective on galaxy clustering as a cosmological probe: General relativistic effects*, *Phys. Rev. D* **80** (2009) 083514, [`arXiv:0907.0707`].

[65] K. N. Abazajian et al., *CMB-S4 Science Book, First Edition*, *arXiv e-prints*, (2016), [`arXiv:1610.02743`]

[66] L. Knox, *Determination of inflationary observables by cosmic microwave background anisotropy experiments*, *Phys. Rev. D*, **52** (1995), 4307, [`arXiv:astro-ph/9504054`]

[67] W. Hu,& T. Okamoto, *Mass Reconstruction with Cosmic Microwave Background Polarization*, *Astrophys. J.*, **574** (2002), 566, [`astro-ph/0111606`]

[68] C. M. Hirata, & U. Seljak, *Reconstruction of lensing from the cosmic microwave background polarization*, *Phys. Rev. D*, **68** (2003), 083002, [`astro-ph/0306354`]

[69] K. M. Smith, D. Hanson, M. LoVerde, C. M.Hirata & O. Zahn, *Delensing CMB polarization with external datasets*, *Journal of Cosmology and Astro-Particle Physics*, **2012** (2012), 014, [`arXiv:1010.0048`]

[70] R. A. Battye, R. D. Davies & J. Weller, *Neutral hydrogen surveys for high-redshift galaxy clusters and protoclusters*, *Mon. Not. Roy. Astron. Soc.*, **355** (2004), 1339, [`astro-ph/0401340`]

[71] J. S. B. Wyithe & A. Loeb, *Fluctuations in 21-cm emission after reionization*, *Mon. Not. Roy. Astron. Soc.*, **383** (2008), 606, [`arXiv:0708.3392`]

[72] T.-C. Chang, U.-L. Pen, J. B. Peterson & P. McDonald, *Baryon Acoustic Oscillation Intensity Mapping of Dark Energy*, *Phys. Rev. Let.*, **100** (2008), 091303, [`arXiv:0709.3672`]

[73] P. Bull, P. G. Ferreira, P. Patel & M. G. Santos, *Late-time Cosmology with 21 cm Intensity Mapping Experiments*, *Astrophys. J.*, **803** (2015), 21, [`arXiv:1405.1452`]

[74] M. G. Santos, P. Bull, D. Alonso, S. Camera, P. G. Ferreira, G. Bernardi, R. Maartens, M. Viel, F. Villaescusa-Navarro, F. B. Abdalla, M. Jarvis, R. B. Metcalf, A. Pourtsidou, L. & Wolz, *Cosmology from a SKA HI intensity mapping survey*, *Advancing Astrophysics with the Square Kilometre Array (AASKA14)*, (2015), 19, [`arXiv:1501.03989`]

[75] E. D. Kovetz, M. P. Viero, A. Lidz, L. Newburgh, M. Rahman, E. Switzer, M. Kamionkowski, J. Aguirre, M. Alvarez, J. Bock, J. R. Bond, G. Bower, C. M. Bradford, P. C. Breysse, P. Bull, T.-C. Chang, Y.-T. Cheng, D. Chung, K. Cleary, A. Corray, A. Crites, R. Croft, O. Dor, M. Eastwood, A. Ferrara, J. Fonseca, D. Jacobs, G. K. Keating, G. Lagache, G. Lakhlani, A. Liu, K. Moodley, N. Murray, A. Pnin, G. Popping, A. Pullen, D. Reichers, S. Saito, B. Saliwanchik, M. Santos, R. Somerville, G. Stacey, G. Stein, E. Villaescusa-Navarro, E. Visbal, A. Weltman, L. Wolz, & M. Zemcov, *Line-Intensity Mapping: 2017 Status Report*, *arXiv e-prints*, (2017), [`arXiv:1709.09066`]

[76] **MeerKLASS** Collaboration, M. G. Santos et al., *MeerKLASS: MeerKAT Large Area Synoptic Survey*, 2017. `arXiv:1709.06099`.

[77] Square Kilometre Array Cosmology Science Working Group, D. J. Bacon et al., *Cosmology with Phase 1 of the Square Kilometre Array; Red Book 2018: Technical specifications and performance forecasts*, *arXiv e-prints*, (2018), [`arXiv:1811.02743`]

[78] Z. Ma, W. Hu, & D. Huterer, *Effects of Photometric Redshift Uncertainties on Weak-Lensing Tomography*, *Astrophys. J.*, **636** (2006), 21, [`astro-ph/0506614`]

[79] R. Laureijs et al., *Euclid Definition Study Report*, arXiv e-prints, (2011), [`arXiv:1110.3193`]

[80] L. Amendola et al., *Cosmology and fundamental physics with the Euclid satellite*, *Living Reviews in Relativity*, **21** (2018), 2, [`arXiv:1606.00180`]

[81] The LSST Dark Energy Science Collaboration, R. Mandelbaum et al., *The LSST Dark Energy Science Collaboration (DESC) Science Requirements Document*, *arXiv e-prints*, (2018), [`arXiv:1809.01669`]

[82] M. Ballardini, & R. Maartens, *Measuring the ISW effect with next-generation radio surveys*, *Mon. Not. Roy. Astron. Soc.*, **485** (2019), 1339, []

[83] N. Dalal, O. Dor, D. Huterer, & A. Shirokov, *Imprints of primordial non-Gaussianities on large-scale structure: Scale-dependent bias and abundance of virialized objects*, *Phys. Rev. D*, **77** (2008), 123514, [`arXiv:0710.4560`]

[84] N. Bartolo, E. Komatsu, S. Matarrese, and A. Riotto, *Non-Gaussianity from inflation: Theory and observations*, *Phys. Rept.* **402** (2004) 103–266, [`astro-ph/0406398`].

[85] X. Chen, *Primordial Non-Gaussianities from Inflation Models*, *Adv. Astron.* **2010** (2010) 638979, [`arXiv:1002.1416`].

[86] J. M. Maldacena, *Non-Gaussian features of primordial fluctuations in single field inflationary models*, *JHEP* **05** (2003) 013, [`astro-ph/0210603`].

[87] V. Acquaviva, N. Bartolo, S. Matarrese, and A. Riotto, *Second order cosmological perturbations from inflation*, *Nucl. Phys.* **B667** (2003) 119–148, [`astro-ph/0209156`].

[88] C. T. Byrnes, & K.-Y. Choi, *Review of Local Non-Gaussianity from Multifield Inflation*, *Advances in Astronomy*, **2010** (2010), 724525, [`arXiv:1002.3110`]

[89] P. Creminelli, & M. Zaldarriaga, *A single-field consistency relation for the three-point function*, *Journal of Cosmology and Astro-Particle Physics*, **2004** (2004), 006, [`astro-ph/0407059`]

[90] W. Hu, & M. White, *CMB anisotropies: Total angular momentum method*, *Phys. Rev. D*, **56** (1997), 596, [`astro-ph/9702170`]

[91] Planck Collaboration, Y. Akrami et al., *Planck 2018 results. IX. Constraints on primordial non-Gaussianity*, *arXiv e-prints*, (2019), arXiv:1905.05697, [arXiv:1905.05697]

[92] D. S. Salopek, & J. R. Bond, *Nonlinear evolution of long-wavelength metric fluctuations in inflationary models*, *Phys. Rev. D*, **42** (1990), 3936

[93] A. Gangui, F. Lucchin, S. Matarrese, and S. Mollerach, *The Three point correlation function of the cosmic microwave background in inflationary models*, *Astrophys. J.* **430** (1994) 447–457, [astro-ph/9312033].

[94] A. Lewis, A. Challinor, & A. Lasenby, *Efficient Computation of Cosmic Microwave Background Anisotropies in Closed Friedmann-Robertson-Walker Models*, *Astrophys. J.*, **538** (2000), 473, [astro-ph/9911177]

[95] C. Howlett, A. Lewis, A. Hall, & A. Challinor, *CMB power spectrum parameter degeneracies in the era of precision cosmology*, *Journal of Cosmology and Astro-Particle Physics*, **2012** (2012), 027, [arXiv:1201.3654]

[96] M. Schmittfull, & U. Seljak, *Parameter constraints from cross-correlation of CMB lensing with galaxy clustering*, *Phys. Rev. D*, **97** (2018), 123540, [arXiv:1710.09465]

[97] E. Giusarma, S. Vagnozzi, S. Ho, S. Ferraro, K. Freese, R. Kamen-Rubio & K.-B. Luk, *Scale-dependent galaxy bias, CMB lensing-galaxy cross-correlation, and neutrino masses*, *Phys. Rev. D*, **98** (2018), 123526, [arXiv:1802.08694]

[98] N. Dalal, O. Dor, D. Huterer, & A. Shirokov, *Imprints of primordial non-Gaussianities on large-scale structure: Scale-dependent bias and abundance of virialized objects*, *Phys. Rev. D*, **77** (2008), 123514, [arXiv:0710.4560]

[99] S. Matarrese, & L. Verde, *The Effect of Primordial Non-Gaussianity on Halo Bias*, *Astrophys. J.*, **677** (2008), L77, [0801.4826]

[100] V. Desjacques, U. Seljak, & I. T. Iliev, *Scale-dependent bias induced by local non-Gaussianity: a comparison to N-body simulations*, *Mon. Not. Roy. Astron. Soc.*, **396** (2009), 85, [arXiv:0811.2748]

[101] A. Slosar, C. Hirata, U. Seljak, S. Ho, & N. Padmanabhan, *Constraints on local primordial non-Gaussianity from large scale structure*, *Journal of Cosmology and Astro-Particle Physics*, **2008** (2008), 031, [arXiv:0805.3580]

[102] S. Camera, M. G. Santos, P. G. Ferreira, & L. Ferramacho, *Cosmology on Ultralarge Scales with Intensity Mapping of the Neutral Hydrogen 21 cm Emission: Limits on Primordial Non-Gaussianity*, *Phys. Rev. Lett.*, **111** (2013), 171302, [arXiv:1305.6928]

[103] D. Alonso, P. Bull, P. G. Ferreira, R. Maartens, and M. Santos, *Ultra large-scale cosmology in next-generation experiments with single tracers*, *Astrophys. J.* **814** (2015), no. 2 145, [arXiv:1505.07596].

[104] E. Castorina, N. Hand, U. Seljak, F. Beutler, C.-H. Chuang, C. Zhao, H. Gil-Marn, W. J. Percival, A. J. Ross, P D. Choi, K. Dawson, A. de la Macorra, G. Rossi, R. Ruggeri, D. Schneider & G.-B. Zhao, *Redshift-weighted constraints on primordial non-Gaussianity from the clustering of the eBOSS DR14 quasars in Fourier space*, *arXiv e-prints*, (2019), [1904.08859]

[105] X. Chen, *Running non-Gaussianities in Dirac-Born-Infeld inflation*, *Phys. Rev. D*, **72** (2005), 123518, [astro-ph/0507053]

[106] E. Sefusatti, M. Liguori, A. P. S. Yadav, M. G. Jackson & E. Pajer, *Constraining running non-gaussianity*, *Journal of Cosmology and Astro-Particle Physics*, **2009** (2009), 022, [arXiv:0906.0232]

[107] A. Raccanelli, O. Dor & N. Dalal, *Optimization of spectroscopic surveys for testing non-Gaussianity*, *Journal of Cosmology and Astro-Particle Physics*, **2015** (2015), 034, [arXiv:1409.1927]

[108] A. Becker & D. Huterer, *First Constraints on the Running of Non-Gaussianity*, *Phys. Rev. Lett.*, **109** (2012), 121302, [arXiv:1207.5788]

[109] F. Oppizzi, M. Liguori, A. Renzi, F. Arroja & N. Bartolo, *CMB constraints on running non-Gaussianity*, *Journal of Cosmology and Astro-Particle Physics*, **2018** (2018), 045, [arXiv:1711.08286]

[110] H. J. Mo & S. D. M. White, *An analytic model for the spatial clustering of dark matter haloes*, Mon. Not. Roy. Astron. Soc., **282** (1996), 347, [astro-ph/9512127]

[111] R. K. Sheth & G. Tormen, *Large-scale bias and the peak background split, Mon. Not. Roy. Astron. Soc.*, **308** (1999), 119, [astro-ph/9901122]

[112] F. Schmidt and M. Kamionkowski, *Halo Clustering with Non-Local Non-Gaussianity*, Phys. Rev. **D82** (2010) 103002, [arXiv:1008.0638].

[113] V. Desjacques, D. Jeong, and F. Schmidt, *Large-Scale Galaxy Bias*, arXiv:1611.09787.

[114] T. H.-C. Lu, K. Ananda, C. Clarkson, and R. Maartens, *The cosmological background of vector modes*, JCAP **0902** (2009) 023, [arXiv:0812.1349].

[115] M. Ballardini, W. L. Matthewson & R. Maartens, *Constraining primordial non-Gaussianity using two galaxy surveys and CMB lensing, Mon. Not. Roy. Astron. Soc.*, (accepted 13 August 2019), [arXiv:1906.04730]

[116] A. Pillepich, C. Porciani & T. H. Reiprich, *The X-ray cluster survey with eRosita: forecasts for cosmology, cluster physics and primordial non-Gaussianity, Mon. Not. Roy. Astron. Soc.*, **422** (2012), 44, [arXiv:1111.6587]

[117] A. Mana, T. Giannantonio, J. Weller, B. Hoyle, G. Htsi & B. Sartoris, *Combining clustering and abundances of galaxy clusters to test cosmology and primordial non-Gaussianity, Mon. Not. Roy. Astron. Soc.*, **434** (2013), 684, [arXiv:1303.0287]

[118] B. Sartoris, A. Biviano, C. Fedeli, J. G. Bartlett, S. Borgani, M. Costanzi, C. Giocoli, L. Moscardini, J. Weller, B. Ascaso, S. Bardelli, S. Maurogordato & P. .T. P. Viana, *Next generation cosmology: constraints from the Euclid galaxy cluster survey, Mon. Not. Roy. Astron. Soc.*, **459** (2016), 1764, [arXiv:1505.02165]

[119] M. Tucci, V. Desjacques & M. Kunz, *Cosmic infrared background anisotropies as a window into primordial non-Gaussianity, Mon. Not. Roy. Astron. Soc.*, **463** (2016), 2046, [arXiv:1606.02323]

[120] K. C. Chan,N. Hamaus & M. Biagetti, *Constraint of void bias on primordial non-Gaussianity*, *Phys. Rev. D*, **99** (2019), 121304, [`arXiv:1812.04024`]

[121] J. Fonseca, R. Maartens & M. G. Santos, *Synergies between intensity maps of hydrogen lines*, *Mon. Not. Roy. Astron. Soc.*, **479** (2018), 3490, [`arXiv:1803.07077`]

[122] A. Moradinezhad Dizgah & G. K. Keating, *Line Intensity Mapping with [C II] and CO(1-0) as Probes of Primordial Non-Gaussianity*, *Astrophys. J.*, **872** (2019), 126, [`arXiv:1810.02850`]

[123] J. R. Fergusson,H. F. Gruetjen, E. P.S. Shellard, & M. Liguori, *Combining power spectrum and bispectrum measurements to detect oscillatory features*, *Phys. Rev. D*, **91** (2015), 023502, [`arXiv:1410.5114`]

[124] J. R. Fergusson, H. F. Gruetjen, E. P. S. Shellard, & B. Wallisch, *Polyspectra searches for sharp oscillatory features in cosmic microwave sky data*, *Phys. Rev. D*, **91** (2015), 123506, [`arXiv:1412.6152`]

[125] D. Karagiannis, A. Lazanu, M. Liguori, A. Raccanelli, N. Bartolo, & L. Verde, *Constraining primordial non-Gaussianity with bispectrum and power spectrum from upcoming optical and radio surveys*, *Mon. Not. Roy. Astron. Soc.*, **478** (2018), 1341, [`arXiv:`]

[126] J. Hung, J. R. Fergusson, & E. P. S. Shellard, *Advancing the matter bispectrum estimation of large-scale structure: a comparison of dark matter codes*, *arXiv e-prints*, (2019), arXiv:1902.01830, [`arXiv:`]